

DESIGN STUDIES IN FLUID DYNAMICS:

I - DEVELOPMENT OF A LOW-SPEED WIND TUNNEL

II - HYDRODYNAMICS OF THE EXHAUST DUCT

OF A HYDROKINETIC TURBINE

by

Catherine Elizabeth Clark

Bachelor of Aerospace Engineering (Carleton University)

A thesis submitted to the Faculty of Graduate Studies and Research
in partial fulfillment of the requirements for the degree of

Masters of Applied Science

Ottawa-Carleton Institute for Mechanical and Aerospace Engineering

Department of Mechanical and Aerospace Engineering

Carleton University

Ottawa, Ontario

Canada

January 2010



Library and Archives
Canada

Published Heritage
Branch

395 Wellington Street
Ottawa ON K1A 0N4
Canada

Bibliothèque et
Archives Canada

Direction du
Patrimoine de l'édition

395, rue Wellington
Ottawa ON K1A 0N4
Canada

Your file *Votre référence*
ISBN: 978-0-494-68653-9
Our file *Notre référence*
ISBN: 978-0-494-68653-9

NOTICE:

The author has granted a non-exclusive license allowing Library and Archives Canada to reproduce, publish, archive, preserve, conserve, communicate to the public by telecommunication or on the Internet, loan, distribute and sell theses worldwide, for commercial or non-commercial purposes, in microform, paper, electronic and/or any other formats.

The author retains copyright ownership and moral rights in this thesis. Neither the thesis nor substantial extracts from it may be printed or otherwise reproduced without the author's permission.

In compliance with the Canadian Privacy Act some supporting forms may have been removed from this thesis.

While these forms may be included in the document page count, their removal does not represent any loss of content from the thesis.

AVIS:

L'auteur a accordé une licence non exclusive permettant à la Bibliothèque et Archives Canada de reproduire, publier, archiver, sauvegarder, conserver, transmettre au public par télécommunication ou par l'Internet, prêter, distribuer et vendre des thèses partout dans le monde, à des fins commerciales ou autres, sur support microforme, papier, électronique et/ou autres formats.

L'auteur conserve la propriété du droit d'auteur et des droits moraux qui protègent cette thèse. Ni la thèse ni des extraits substantiels de celle-ci ne doivent être imprimés ou autrement reproduits sans son autorisation.

Conformément à la loi canadienne sur la protection de la vie privée, quelques formulaires secondaires ont été enlevés de cette thèse.

Bien que ces formulaires aient inclus dans la pagination, il n'y aura aucun contenu manquant.

■ ■ ■
Canada

ABSTRACT

This thesis examines the optimization of two internal fluid flow paths: the design of a low-speed, open-circuit wind tunnel and the evaluation of the pressure-recovery performance through the exhaust duct of the Carleton Hydrokinetic Turbine. The wind tunnel is designed to provide highly uniform, low-turbulence test section flow at lower velocities than the existing Carleton wind tunnels provide, with the design constrained by the available laboratory space. The exhaust duct of the Carleton Hydrokinetic Turbine creates a high rate of static pressure recovery downstream of the turbine assembly, for the purpose of increasing the power output of the turbine. The present study evaluates the sensitivity of the hydrodynamic performance of the exhaust duct to a range of geometric parameters specific to this design. These studies provide excellent examples of the use of state-of-the-art computational design tools in fluid engineering, and demonstrate the reliability of such tools for two substantially different applications.

TABLE OF CONTENTS

Abstract	ii
Table of Contents	iii
List of Tables.....	vii
List of Figures	viii
Nomenclature	xiii
1 Introduction	1
2 Development of a Low-Speed Wind Tunnel.....	3
2.1 Introduction to Wind Tunnel Design.....	3
2.2 Review of Current Wind Tunnel Designs.....	3
2.3 Wind Tunnel Design Constraints	5
2.4 General Configuration of Wind Tunnel.....	6
2.5 Design of Wind Tunnel Inlet and Flow-Conditioning Screen	8
2.6 Description of Test Section.....	10
2.7 Sizing of Transition Duct and Fan Module	11
2.8 Design of Wind Tunnel Contraction	13
2.8.1 Contraction Contour defined using Morel's Equations.....	14
2.8.2 Contraction Contour defined using Mikhail/Rainbird's Equations	16
2.8.3 Evaluation of Contraction Geometries Using CFD.....	18
2.8.4 Construction of Contraction.....	31
2.9 Installation of Wind Tunnel Static Taps	33
2.9.1 Static Tap Placement	33
2.9.2 Static Tap Sizing	35

2.9.3	Static Tap Installation.....	35
2.10	Assembly of Wind Tunnel	36
2.11	Design of 3-Axis Traverse System	38
2.11.1	Traverse System Design Constraints.....	38
2.11.2	Detailed Design of Traverse System.....	38
2.11.3	Traverse System Deflection under Load	44
2.11.4	Range and Accuracy of Probe Placement.....	51
2.12	Summary of Wind Tunnel Design and Construction.....	52
2.13	Introduction to Wind Tunnel Commissioning.....	53
2.14	Instrumentation used in Wind Tunnel Commissioning	54
2.14.1	Description of Instrumentation	54
2.15	Wind Tunnel Static Tap Calibration	57
2.16	Wind Tunnel Test Configurations	58
2.17	Measured Wind Tunnel Boundary-Layer Profiles	61
2.18	Measured Wind Tunnel Boundary-Layer Shape Factors.....	63
2.19	Measured Flow Uniformity at Test Section Inlet	63
2.20	Measured Turbulence Intensity at Test Section Inlet	67
2.21	Summary of Wind Tunnel Commissioning.....	68
3	Hydrodynamics of the Exhaust Duct of a Hydrokinetic Turbine	70
3.1	Introduction to Hydrokinetic Turbines	70
3.2	Carleton Hydrokinetic Turbine	70
3.2.1	Internal Geometry of the Carleton Hydrokinetic Turbine Exhaust Duct	73
3.3	Review of Flows through Conical Diffusers	75

3.4	Turbulence Model Selection	76
3.5	Turbulence Model Validation	79
3.5.1	Experimental Parameters	79
3.5.2	Computational Domain.....	80
3.5.3	Boundary Conditions.....	82
3.5.4	Type of Spatial Grid	84
3.5.5	Discretization of Spatial Derivatives.....	84
3.5.6	Solution Algorithm and Convergence Study	86
3.5.7	Grid Convergence Study.....	87
3.5.8	Simulation Results for the Turbulence Model Validation Study	89
3.6	Evaluation of the Carleton Hydrokinetic Turbine Exhaust Duct	96
3.6.1	Computational Domain.....	96
3.6.2	Boundary Conditions.....	99
3.6.3	Grid Convergence Study.....	106
3.6.4	Exhaust Duct Flow Field and Pressure-Recovery Performance	108
3.6.5	Sensitivity of Exhaust Duct Pressure-Recovery Performance to Variations in Geometry	123
3.7	Flow Visualization through the Carleton Hydrokinetic Turbine Exhaust Duct in a Water Channel	128
3.7.1	Manufacturing of the Exhaust Duct Model	128
3.7.2	Evaluation of Exhaust Duct Performance Using Flow Visualization	132
3.8	Recommendations and Future Work	137
3.9	Summary of Pressure-Recovery Performance of Exhaust Duct	137

4	Conclusions	139
	References	142
Appendix A.	Wind Tunnel Three-View Drawings	145
Appendix B.	Wind Tunnel Fan Information.....	148
Appendix C.	Wind Tunnel Assembly Instructions	149
Appendix D.	Wind Tunnel Disassembly Instructions	150
Appendix E.	Traverse System Design Iterations	151
Appendix F.	Photographs of Installed Traverse System.....	152
Appendix G.	Operation of Traverse System.....	154
Appendix H.	Wind Tunnel Cost Report	162
Appendix I.	Wind Tunnel Boundary Layer Profiles.....	164
Appendix J.	Wind Tunnel Mean-Velocity Plots.....	166
Appendix K.	Hotwire Anemometer Data Reduction.....	170
Appendix L.	Stagnation Pressure Drop in Axial-Turbine	172
Appendix M.	Description of Water Channel Facility	174
Appendix N.	Flow Visualization in Water Channel.....	178

LIST OF TABLES

Table 2.1 Parameters for Contraction using Mikhail/Rainbird's Equations	18
Table 2.2 Contraction Grid Convergence Study Parameters and Results	24
Table 2.3 Predicted Flow Properties at Contraction Outlet	26
Table 2.4 Predicted Boundary-Layer Shape Factors in Contraction	30
Table 2.5 Drag Force on Probe Stem in Streamwise Direction	45
Table 2.6 Summary of Traverse System Motion Capabilities	52
Table 2.7 Pitot-Static Pressure Probe Properties	55
Table 2.8 Pitot-Total Pressure Probe Properties	56
Table 3.1 Geometric Parameters for Evaluation of Exhaust Duct Performance.....	108
Table A.1 Wind Tunnel Assembly Instructions.....	149
Table A.2 Wind Tunnel Disassembly Instructions	150
Table A.3 Traverse System Design Iterations.....	151
Table A.4 Wind Tunnel Contraction Costs.....	162
Table A.5 Wind Tunnel Traverse System Costs.....	163
Table A.6 Velocity Spatial Distribution for $\Delta 1 = \Delta 2$ with Flow-Conditioning Screen ..	166
Table A.8 Velocity Spatial Distribution for $\Delta 1 \neq \Delta 2$ with Flow-Conditioning Screen ..	167
Table A. 9 Velocity Spatial Distribution Repeatability.....	168
Table A.10 Effect of Flow-Conditioning Screen on Velocity Spatial Distribution	169

LIST OF FIGURES

Figure 2.1 Main Components of the Carleton Open-Circuit Suction Wind Tunnel	7
Figure 2.2 Rounded Wind Tunnel Inlet Segment	8
Figure 2.3 Wind Tunnel Inlet Assembly (Exploded View)	9
Figure 2.4 Test Section Components.....	10
Figure 2.5 Fan Module and Transition Duct Components	11
Figure 2.6 Parameters for Contraction Contour using Morel's Equations	14
Figure 2.7 Parameters for Contraction Contour using Mikhail/Rainbird's Equations	17
Figure 2.8 Boundary Conditions for Simulations of Flow through Contraction	21
Figure 2.9 Grid-Node Spacing and Inflation Layers at Contraction Inlet	23
Figure 2.10 Grid-Node Spacing and Inflation Layers at Contraction Outlet.....	23
Figure 2.11 Contraction Outlet Velocity Contour Plot: Morel's Equations, $L=2.13$ m	27
Figure 2.12 Contraction Outlet Velocity Contour Plot: Morel's Equations, $L=1.14$ m	27
Figure 2.13 Contraction Outlet Velocity Contour Plot: Mikhail's Equations, $L=1.14$ m ..	27
Figure 2.14 Pressure Gradient through Contraction.....	28
Figure 2.15 Streamwise Pressure Gradient along Length of Contraction	29
Figure 2.16 Contraction Support Structure.....	32
Figure 2.17 Contraction Wall Assembly	33
Figure 2.18 Location of Static Pressure Taps in Wind Tunnel.....	34
Figure 2.19 Installed Wind Tunnel Static Taps	36
Figure 2.20 Contraction Assembly Procedure	36
Figure 2.21 Photographs of Constructed Wind Tunnel.....	37
Figure 2.22 Solid Model of Traverse System	39

Figure 2.23 Solid Model of Traverse System Support Structure in 3175 ME.....	40
Figure 2.24 Solid Model of Traverse System and Streamwise Motion Components	41
Figure 2.25 Solid Model of Traverse System and Spanwise Motion Components	42
Figure 2.26 Solid Model of Traverse System and Vertical Motion Components.....	43
Figure 2.27 Solid Model of Traverse System and Probe Mounting Block.....	43
Figure 2.28 Streamwise Deflections in Traverse System under Load	45
Figure 2.29 Spanwise Deflections in Traverse System under Load.....	47
Figure 2.30 Location of Loads on Traverse System Support Structure	48
Figure 2.31 Vertical Deflections in Support Structure under Load	49
Figure 2.32 Vertical Deflections in Traverse System under Load.....	50
Figure 2.33 Location of Pitot-Static Pressure Probe (Top View)	54
Figure 2.34 Calibration of Contraction Wall Static Pressure Taps.....	58
Figure 2.35 Test Section Profile with Flat Ceiling.....	59
Figure 2.36 Test Section Profile with Contoured Ceiling	59
Figure 2.37 Contraction-to-Wall Spacing Measurement Locations.....	60
Figure 2.38 Boundary-Layer Profiles at Test Section Inlet	61
Figure 2.39 Velocity Uniformity at Test Section Inlet for Configuration 1	64
Figure 2.40 Velocity Uniformity at Test Section Inlet for Configuration 2	65
Figure 2.41 Velocity Uniformity at Test Section Inlet for Configuration 3	66
Figure 2.42 Variation in Turbulence Intensity with Wind Tunnel Velocity.....	68
Figure 3.1 Carleton Hydrokinetic Turbine Components	72
Figure 3.2 Schematic of Flow through Carleton Hydrokinetic Turbine.....	72
Figure 3.3 Orientation of Carleton Hydrokinetic Turbine Relative to Local Currents	73

Figure 3.4 Internal Geometry of Carleton Hydrokinetic Turbine Exhaust Duct	74
Figure 3.5 Experiment Setup for Turbulence Model Validation Study	80
Figure 3.6 Computational Domain for Turbulence Model Validation Study	81
Figure 3.7 Computational Grid for Turbulence Model Validation Study	88
Figure 3.8 Axial Velocity (U/U_{REF}) Results with SST Model	89
Figure 3.9 Near-Wall Axial Velocity (U/U_{REF}) Results with SST Model	90
Figure 3.10 Tangential Velocity (W/U_{REF}) Results with SST Model	90
Figure 3.11 Turbulence Kinetic Energy ($k/(U_{REF}^2)*100$) Results with SST Model	91
Figure 3.12 Axial Velocity (U/U_{REF}) Results with RNG k- ϵ Model	92
Figure 3.13 Near-Wall Axial Velocity (U/U_{REF}) Results with RNG k- ϵ Model	93
Figure 3.14 Tangential Velocity (W/U_{REF}) Results with RNG k- ϵ Model	93
Figure 3.15 Turbulence Kinetic Energy ($k/(U_{REF}^2)*100$) Results with RNG k- ϵ Model ..	94
Figure 3.16 Computational Domain for Exhaust Duct Flow Simulations	97
Figure 3.17 Geometric Parameters for Evaluation of Exhaust Duct Performance	98
Figure 3.18 Location of Domain for Side Intake Boundary Condition Simulations	102
Figure 3.19 Computational Domain for Side Intake Boundary Condition Simulations ..	103
Figure 3.20 Stagnation Pressure Profile for Side Intake Boundary Condition	105
Figure 3.21 Turbulence Kinetic Energy Profile for Side Intake Boundary Condition	105
Figure 3.22 Computational Grid for Evaluation of Exhaust Duct Performance	107
Figure 3.23 Effect of Inclination Angle (α) on Exhaust Duct Performance	109
Figure 3.24 Flow Field through Exhaust Duct at $\alpha = 60$ deg. (View 1)	111
Figure 3.25 Flow Field through Exhaust Duct at $\alpha = 60$ deg. (View 2)	111
Figure 3.26 Flow Field through Exhaust Duct at $\alpha = 60$ deg. (View 3)	112

Figure 3.27 Axial Flow through Exhaust Duct at $\alpha = 60$ deg.	113
Figure 3.28 Static Pressure Field through Exhaust Duct at $\alpha = 60$ deg.	114
Figure 3.29 Stagnation Pressure Field through Exhaust Duct at $\alpha = 60$ deg.	115
Figure 3.30 Side Intake Flow through Exhaust Duct for Multiple Inclination Angles ...	116
Figure 3.31 Flow Field through Exhaust Duct at $\alpha = 30$ deg. (Side View)	117
Figure 3.32 Flow Field through Exhaust Duct at $\alpha = 30$ deg. (Front View)	118
Figure 3.33 Flow Field through Exhaust Duct at $\alpha = 60$ deg. (Side View)	119
Figure 3.34 Flow Field through Exhaust Duct at $\alpha = 60$ deg. (Front View)	119
Figure 3.35 Flow Field through Exhaust Duct at $\alpha = 90$ deg. (Side View)	120
Figure 3.36 Flow Field through Exhaust Duct at $\alpha = 90$ deg. (Front View)	121
Figure 3.37 Effect of Side Intake Width on Exhaust Duct Performance.....	124
Figure 3.38 Effect of Axial Intake Diameter on Exhaust Duct Performance	126
Figure 3.39 Effect of Opening Angle on Exhaust Duct Performance	127
Figure 3.40 Scale Model of Carleton Hydrokinetic Turbine Exhaust Duct	129
Figure 3.41 Brass Spacers for Maintaining Side Intake Width of Scale Model	129
Figure 3.42 Honeycomb and Bulb-Shaped Generator Unit for Scale Model	130
Figure 3.43 Dye Ports for Flow Visualization in Scale Model	131
Figure 3.44 Flow Visualization in Exhaust Duct Model with $w = 0.3 D_{REF}$ (Side).....	133
Figure 3.45 Flow Visualization in Exhaust Duct Model with $w = 0.3 D_{REF}$ (Bottom) ...	134
Figure 3.46 Flow Visualization in Exhaust Duct Model with $w = 0.1 D_{REF}$	136
Figure A.1 Three-View Drawing of Wind Tunnel Test Section.....	145
Figure A.2 Three-View Drawing of Wind Tunnel Transition Duct and Fan Module	146
Figure A.3 Three-View Drawing of Wind Tunnel Contraction and Inlet	147

Figure A.4 Traverse System Installed in 3175 ME	152
Figure A.5 Traverse System and Streamwise Motion Components Installed in 3175 ME	152
Figure A.6 Traverse System and Spanwise Motion Components Installed in 3175 ME	153
Figure A.7 Traverse System and Vertical Motion Components Installed in 3175 ME ..	153
Figure A.8 Wiring Diagram for Traverse System	154
Figure A.9 Traverse System User Interface	155
Figure A.10 Boundary Layer Profiles with Flow-Conditioning Screen.....	164
Figure A.11 Boundary Layer Profiles without Flow-Conditioning Screen.....	165
Figure A.12 Specific Speeds for Various Hydraulic Turbines	172
Figure A.13 Schematic of Water Channel Facility	174
Figure A.14 Photographs of Water Channel Platform	176
Figure A.15 Visualization of Flow over a Cylinder	180

NOMENCLATURE

Acronyms

CFD	Computational Fluid Dynamics
DNS	Direct Numerical Simulation
LES	Large-Eddy Simulation
ME	Mackenzie Building
NRC	National Research Council
RANS	Reynolds-Averaged Navier-Stokes
RCZ	Recirculation Zone
RHRC	Rolling Hills Research Corporation
RMS	Root-Mean Square
RNG	Re-Normalization Group
SG	Specific Gravity
SST	Shear Stress Transport

English Symbols

c_p	Coefficient of pressure
D	Diameter [m]
D_{IN}	Diameter of axial intake of Carleton Hydrokinetic Turbine [m]
D_{REF}	Diameter of axial turbine in Carleton Hydrokinetic Turbine [m]
H	Boundary-layer shape factor
k	Turbulence kinetic energy [m^2/s^2]
L	Length [m]

\dot{m}	Mass flow rate [kg/s]
\dot{m}_{REF}	Reference mass flow rate [kg/s]
\dot{m}_T	Mass flow rate through turbine rotor [kg/s]
P	Static pressure [Pa]
P_{C1}	Static pressure measured at contraction wall tap 1 [Pa]
P_{C2}	Static pressure measured at contraction wall tap 2 [Pa]
P_o	Stagnation pressure [Pa]
$P_{o, REF}$	Reference stagnation pressure [Pa]
q_c	Dynamic pressure along centerline of wind tunnel test section [Pa]
r	Radial distance from centerline [m]
R	Radius [m]
u	Fluctuating component of velocity [m/s]
U	Axial velocity [m/s]
U_C	Centerline axial velocity [m/s]
U_{MAX}	Maximum axial velocity [m/s]
U_{REF}	Reference axial velocity [m/s]
w	Width of side intake of Carleton Hydrokinetic Turbine [m]
W	Tangential velocity [m/s]
x	Axial distance [m]
X_i	Inflection point [m]
y	Distance perpendicular to wall [m]
y^+	Dimensionless wall-normal distance
z	Height [z]

Greek Symbols

α	Inclination angle of Carleton Hydrokinetic Turbine relative to local currents [deg.]
β	Specified blend factor for advection scheme calculations in ANSYS CFX
δ^*	Displacement thickness [m]
$\Delta 1, \Delta 2$	Distances from wind tunnel inlet to laboratory walls on sides 1 and 2 [m]
ε	Dissipation rate of turbulence kinetic energy [m^2/s^3]
θ	Momentum thickness [m]
2θ	Opening angle of diffuser [deg.]
Φ	Variable for discretization of spatial derivatives in ANSYS CFX
ρ	Density [kg/m^3]
ν	Kinematic viscosity [m^2/s]
ω	Specific dissipation rate of turbulence kinetic energy [s^{-1}]

1 INTRODUCTION

The work presented in this thesis contains the design optimization of two internal fluid flows by manipulation of the solid boundaries containing the flows. Although the two projects deal with different real-world applications, they both combine the use of computational design tools with experimental methods to undertake each design in the most accurate and cost-effective manner possible. Both projects evaluate the abilities of two-equation turbulence models to predict flows that are influenced by pressure gradients and streamline curvature, with special focus on modeling the boundary layer and its influence on the core flow of the respective geometries. The experimental results are used to verify the accuracy of the computational results and provide additional information on the flow of interest. The body of this thesis is divided into two chapters that contain the design information, numerical and experimental studies, and conclusions of each project.

The first chapter of this thesis contains the development of an open-circuit, low-speed suction wind tunnel for the Department of Mechanical and Aerospace Engineering at Carleton University. The velocity range for this wind tunnel was selected to complement the existing wind tunnels in the department, which do not provide test section flow with the desired spatial uniformity and turbulence intensity at low Reynolds numbers. All of the wind tunnel components were built in a modular fashion to allow for efficient and reversible disassembly, transportation and reassembly of the wind tunnel in a different laboratory. The wind tunnel contraction, which accelerates the air from the laboratory into the test section, was designed using computational fluid dynamics (CFD) to provide flow with the desired spatial uniformity and turbulence intensity into the test

section. In order to provide a complete wind-tunnel facility, a 3-axis traverse system was designed to provide automated motion of a measurement probe through the volume of the test section. The constructed wind tunnel was commissioned by measuring the spatial uniformity, boundary-layer profile, and turbulence intensity of the flow entering the test section. The sensitivity of these properties to the addition of a flow-conditioning screen, the wall contours of the test section, and the position of the wind tunnel relative to the laboratory walls was measured to provide a complete description of the wind tunnel behaviour over a range of operating conditions.

The second chapter of this thesis evaluates the hydrodynamic performance of the exhaust duct of the Carleton Hydrokinetic Turbine. The Carleton Hydrokinetic Turbine is a free-stream (hydrokinetic) turbine design that extracts energy from river and tidal currents. The exhaust duct of the Carleton Hydrokinetic Turbine is a wide-angle conical diffuser, with a unique configuration that uses tangential flow from a side intake to control the boundary layer development along the exhaust duct walls. The relatively high static pressure recovery through the exhaust duct allows the Carleton Hydrokinetic Turbine to extract more mechanical energy from the turbine through flow than existing alternative designs. The sensitivity of the pressure-recovery performance of the exhaust duct to a range of geometric parameters and flow conditions was evaluated using CFD, and a turbulence model validation study was completed to ensure confidence in the CFD results. The accuracy of the predicted flow field through the exhaust duct was confirmed experimentally using flow visualization through a scaled-model of the exhaust duct in a water channel facility.

2 DEVELOPMENT OF A LOW-SPEED WIND TUNNEL

2.1 INTRODUCTION TO WIND TUNNEL DESIGN

A new wind tunnel facility was designed to provide a low-speed testing environment not offered by the current experimental facilities belonging to Carleton University's Department of Mechanical and Aerospace Engineering. The facility is to be used for experiments requiring low-turbulence, highly uniform and steady flow at low-Reynolds numbers, such as boundary-layer instability and transition experiments that require precisely-controlled free-stream flow conditions.

2.2 REVIEW OF CURRENT WIND TUNNEL DESIGNS

A wind tunnel is an essential tool for engineering design and research of fluid flows. Originally intended as a means to improve aircraft performance, wind tunnels are now used to design everything from road vehicles to parachutes. Although there have been significant advances in computing resources in recent years, wind tunnels are still necessary to verify the accuracy of CFD simulations and evaluate flows that are too complicated or time-consuming for accurate numerical studies. A select number of wind tunnel facilities are presented in this study to give the reader an idea of the capabilities of modern wind tunnels and the flow conditioning that is attainable. The spatial uniformity, turbulence levels and steadiness of the flow through a wind tunnel can have a significant effect on the measured data in the test section, and therefore it is important that these parameters be carefully controlled.

The National Research Council (NRC) in Canada has multiple wind tunnel facilities that provide a wide range of testing conditions, from test sections of 0.9 m x 0.9 m cross-sectional dimensions for university projects and instrument calibration to test sections of 9 m x 9 m cross-sectional dimensions for full-scale road vehicle testing. As an example of the NRC's testing capabilities, their 2m x 3m wind tunnel facility offers a maximum speed of 140 m/s with spatial non-uniformity of $\pm 0.7\%$ and turbulence intensities less than 0.14% (National Research Council, 2009).

The Delft University of Technology in the Netherlands has a number of wind tunnels facilities. Their closed-circuit, low-turbulence wind tunnel offers a maximum speed of 120 m/s with turbulence intensities less than 0.1%, and their vertical, open-circuit wind tunnel offers a maximum speed of 35 m/s with turbulence intensities less than 0.1% (Delft University of Technology, 2009). The University of Washington Aeronautical Laboratory operates an older low-speed wind tunnel for both academic and commercial testing purposes. Their wind tunnel started operation in 1939, and offers test section speeds up to 90 m/s with a turbulence intensity of 0.72%. (University of Washington, 2009)

The examples of wind tunnels described above are all incompressible flow wind tunnels that offer high spatial flow uniformity with low turbulence intensities. Older wind tunnel facilities offer turbulence intensities less than 1%, whereas more modern designs have the ability to reduce turbulence intensity in the test section to less than 0.1% through more refined shaping of wind tunnel flow path and the use of multiple flow-conditioning

devices, including screens and honeycombs. Based on the current state-of-the-art, it is reasonable to expect that a new wind tunnel facility should have spatial flow non-uniformity of less than $\pm 0.5\%$ and free-stream turbulence intensity of less than 0.1% in the test section.

2.3 WIND TUNNEL DESIGN CONSTRAINTS

The current location for the wind tunnel that is the subject of this thesis is 3175 Mackenzie Building (ME); a small laboratory that has a floor space of 5.5 m by 7 m. If space on campus becomes available, it may be desirable to move the wind tunnel to a different location. For this reason, it was required that the wind tunnel be designed in a modular fashion that allows for disassembly, transportation and assembly of the wind tunnel without damaging the structure. Based on the size of the doorway to 3175 ME, all of the wind tunnel components must fit through a 0.9 m by 2.4 m opening.

The velocity range for which this wind tunnel is designed to provide uniform, steady and low-turbulence flow is 1 m/s to 5 m/s, corresponding to Reynolds numbers per unit length of $63,775 \text{ m}^{-1}$ and $318,875 \text{ m}^{-1}$ respectively. These are relatively low Reynolds number compared to the other wind tunnel facilities in the department, and these other facilities do not provide the desired flow quality when operating in low Reynolds number conditions. The maximum test section velocity for which this wind tunnel is being designed is 10 m/s, and this velocity was used to calculate the fan power requirements. For test section velocities from 1 m/s to 5 m/s, the mean flow non-uniformity should be

less than $\pm 0.5\%$ of the spatially-averaged value and the free-stream turbulence intensity should be less than 0.1%.

This wind tunnel is required to accommodate the same test section used with the closed-circuit wind tunnel located in 3230 ME. This allows experiments to be designed for complementary use of the two wind tunnels, allowing for test Reynolds-number and free-stream turbulence ranges greater than those currently feasible with the closed-circuit wind tunnel alone.

2.4 GENERAL CONFIGURATION OF WIND TUNNEL

An open-circuit suction configuration was selected for the wind tunnel based on the desired flow quality in the test section. In an open-circuit suction configuration, the fan pulls the ambient laboratory air through the wind tunnel inlet, contraction, test section and diffuser, and discharges the air back into the surroundings. For an open-circuit wind tunnel with a blower configuration, the fan is installed upstream of the wind tunnel contraction. This arrangement does not provide the desired flow uniformity and turbulence levels without the use of extensive flow-conditioning devices at the wind tunnel inlet. For a closed-circuit wind tunnel, the requirement to move the flow around the wind tunnel circuit may introduce increased levels of flow turbulence and spatial non-uniformity. A closed-circuit configuration also requires a larger structure that includes flow turning vanes and flow-conditioning devices upstream of the test section.

The main components of the Carleton open-circuit suction wind tunnel, shown in Figure 2.1, are the rounded inlet, flow-conditioning screen, contraction, test section, transition duct and fan module. All of these components are supported by steel frames on rolling casters to facilitate movement over the limited floor space and make it easier for the operator to change test sections, install equipment and perform maintenance. Drawings with all the major dimensions of the main wind tunnel components are presented in Appendix A. In order to provide a complete ready-to-use wind tunnel facility, a 3-axis motorized traverse system was designed to allow accurate placement of a probe in the test section.

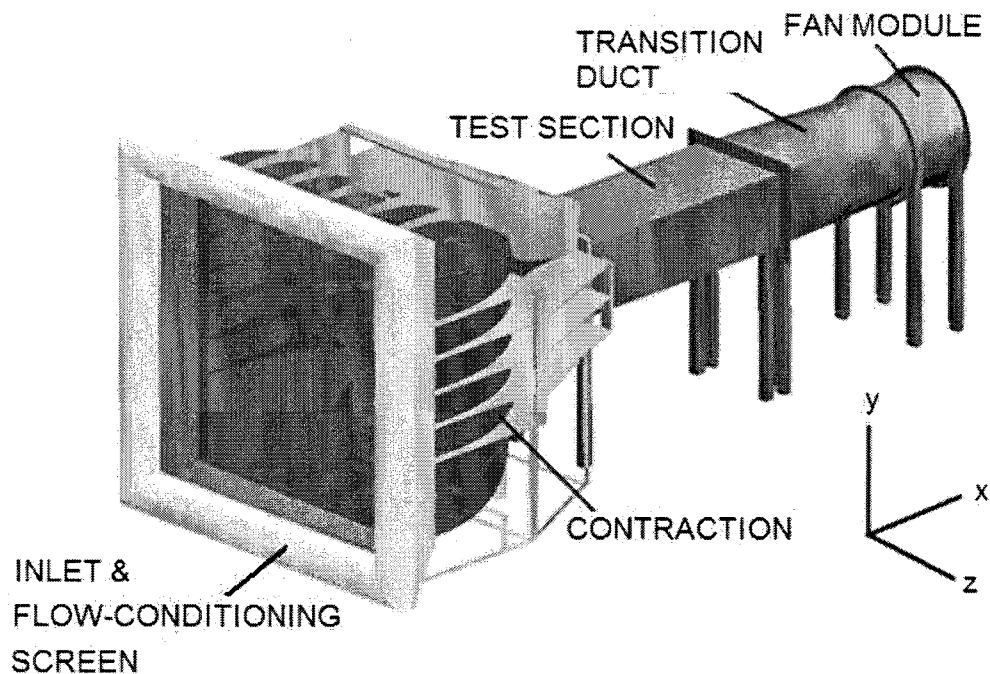


Figure 2.1 Main Components of the Carleton Open-Circuit Suction Wind Tunnel

2.5 DESIGN OF WIND TUNNEL INLET AND FLOW-CONDITIONING SCREEN

The rounded inlet at the entrance of the contraction was designed to smoothly guide the flow from the laboratory environment into the contraction without boundary-layer separation and with a spatially-uniform core flow. The inlet was formed using four tubes 0.3048 m (12 in.) in diameter, composed of 4.76 mm (3/16 in.) thick cardboard material. The tubes are known by the brand name Sonotube, and are used in the construction industry to create concrete forms. One of the four segments that form the rounded inlet is shown in Figure 2.2, with the addition of a flat panel to hold the semi-circular section in place. A thick wooden frame supports the rounded inlet segments and connects them to the contraction using dowel pins and straps. A short rectangular steel base supports the wooden frame from below; therefore the bottom inlet segment does not have a flat panel. The placement of the four inlet segments relative to the wind tunnel contraction is shown in Figure 2.3.

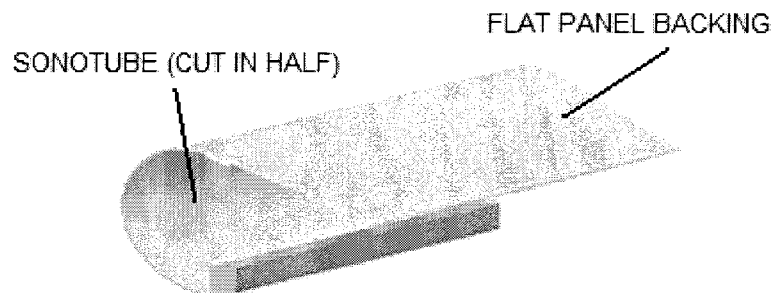


Figure 2.2 Rounded Wind Tunnel Inlet Segment

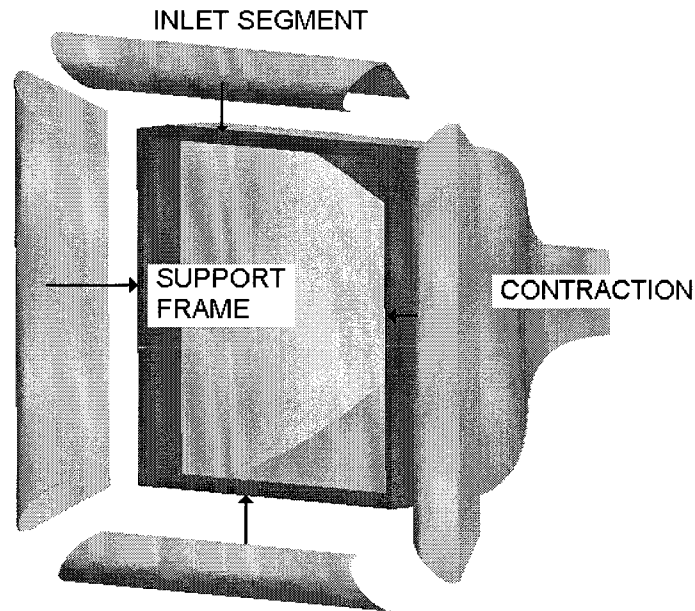


Figure 2.3 Wind Tunnel Inlet Assembly (Exploded View)

One of the main drawbacks of an open-circuit suction wind tunnel configuration is its sensitivity to large-scale, low-frequency unsteady air motion in the laboratory space, driven by the air discharging into the laboratory from the downstream end of the wind tunnel (Bradshaw & Mehta, 1979). For this reason, a flow-conditioning screen was added upstream of the contraction to dampen unsteady flow motions as the air is pulled into the wind tunnel. It is worth noting that the flow-conditioning screen is not a screen in the traditional sense; it is not an interwoven structure with square or rectangular openings. The screen is composed of two layers of porous fibreglass filter material, provided courtesy of Superior Fibres Ltd. (Naperville, IL, USA). The screen is supported by a thin wooden frame sandwiched between the rounded inlet and contraction sections, with holes to accommodate the dowel pin inserts on the mating surfaces of these sections. The effectiveness of the flow-conditioning screen at dampening the unsteady flow motions in the laboratory is evaluated during the commissioning of the wind tunnel facility.

2.6 DESCRIPTION OF TEST SECTION

The primary test section for the new wind tunnel being designed is one of several in use with the department's closed-circuit wind tunnel. A solid model of this test section on its rolling support structure is shown in Figure 2.4. The interior of the test section is 0.508 m (20 in.) high, 0.762 m (30 in.) wide and 1.829 m (72 in.) long. The side walls are made of clear plastic to allow the operator to see inside, the floor and ceiling are made of wood, and a metal frame at each end allows the test section to be clamped to the contraction and the transition duct. The original designers of the test section sized its external dimensions to allow it to fit through a single-panel doorway when turned on its side.

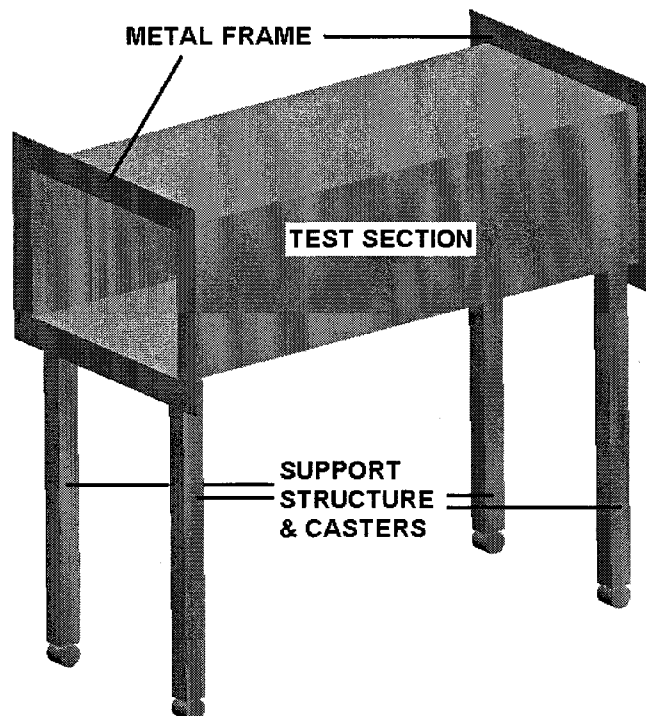


Figure 2.4 Test Section Components

2.7 SIZING OF TRANSITION DUCT AND FAN MODULE

The transition duct interfaces the 0.508 m (20 in.) by 0.762 m (30 in.) rectangular test section with the 0.775 m (30.5 in.) diameter cylindrical fan module. For a duct length of 1.219 m (48 in.), these dimensions correspond to a maximum diffuser opening angle (2θ) of 12.5 deg., and an opening angle (2θ) of 3.43 deg for a conical diffuser with the same length and area ratio. This geometry was selected conservatively to avoid transient flow separation along the walls that could cause unsteady flow upstream in the test section (Bradshaw & Mehta, 1979). The transition duct length was kept as short as possible to reduce the occupied floor space in the laboratory. The fan module is connected to the downstream end of the transition duct, as shown in Figure 2.5.

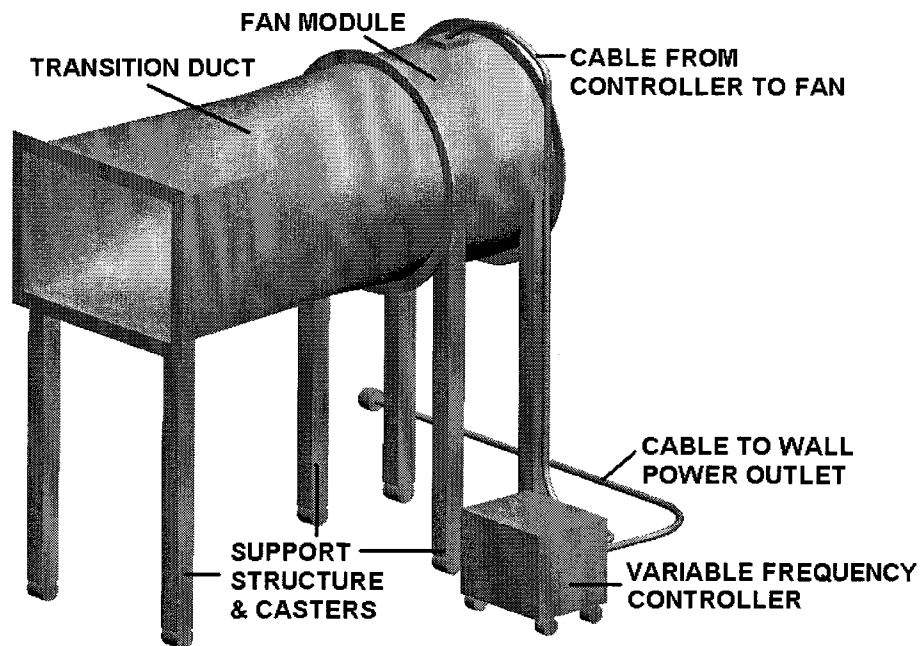


Figure 2.5 Fan Module and Transition Duct Components

The fan module includes a fan, an electric motor, a motor controller and a steel housing. The fan is designed to pull the air through the wind tunnel and discharge it back into the laboratory. The fan blade assembly is contained in a steel housing with a circular cross-section of 0.775 m (30.5 in.) diameter and 0.508 m (20 in.) length, and is located 0.1016 m (4 in.) downstream of the fan housing inlet. The downstream end of the fan housing is covered by a coarse steel grid for safety. The fan has six fixed-pitch blades, a tip diameter of 0.762 m (30 in.), a maximum speed of 183 rad/s (1750 rpm) and an efficiency of 70% at standard operating conditions. It is driven by an AC electric motor mounted on a low-profile support frame in the housing structure downstream of the fan. The motor draws up to 3.73 kW (5 Hp) at 183 rad/s (1750 rpm), and is designed for continuous operation at low rotational speeds. For the present wind tunnel, the motor is controlled by a Siemens MicroMaster Vector variable-frequency controller with 230 V, 3-phase power input. The design and manufacturing of both the transition duct and fan module was performed by Daltec Industries.

Based on preliminary estimates of pressure losses through the inlet, contraction, test section, transition duct and discharge segments of the wind tunnel circuit, the total pressure loss at a flow rate of 3.9 m³/s (for a maximum test section velocity of 10 m/s) was estimated to be 86 Pa. The fan installed in the wind tunnel was designed to supply a flow rate of 4.7 m³/s with a pressure loss of 436 Pa. The fan was oversized to account for pressure losses due to any flow-conditioning devices and model aerodynamic drag in the test section. There is no disadvantage to having an over-powered fan, since the Siemens Micromaster variable-frequency controller can vary the fan speed from 0 to 183 rad/s

(1750 rpm) and according to the fan performance charts provided by the supplier, the fan is capable of delivering the required pressure rise at the design flow rate of the wind tunnel. The fan design point is labelled in the performance charts presented in Appendix B.

2.8 DESIGN OF WIND TUNNEL CONTRACTION

The purpose of a wind tunnel contraction is to accelerate the air from the laboratory to a desired velocity in the test section. The flow exiting the contraction should be steady, have high spatial uniformity and low turbulence intensity. The boundary layer should remain attached to the walls throughout the contraction, as transient separation can lead to flow unsteadiness in the test section (Bell & Mehta, 1989).

The contraction dimensions were determined based on the amount of floor space in the laboratory given the size of the test section, transition duct and fan module, as well as the desire for a high contraction area ratio (ratio of inlet area to outlet area). A high area ratio is desirable because it reduces pressure losses across flow-conditioning devices at the contraction inlet and reduces the turbulence intensity of the flow entering the test section (Bradshaw & Mehta, 1979). In general, contraction area ratios between 6 and 10 are adequate for low-speed wind tunnels with test section velocities less than 40 m/s (Bell & Mehta, 1989). For the present wind tunnel, setting the contraction width and height to 2.13 m (84 in.) provides a contraction area ratio of 11.76 and allows for the use of standard construction materials that come in 2.44 m (96 in.) lengths.

2.8.1 Contraction Contour defined using Morel's Equations

In 1975, T. Morel published a paper defining the wall contour of an axisymmetric contraction designed to provide attached flow over its entire length. He defined the wall shape using two matched cubic equations that were constrained to have zero slope values at the contraction inlet and outlet. The equations and variables used to define the contraction wall shape are shown in Figure 2.6. (Morel, 1975)

$$\frac{D - D_2}{D_1 - D_2} = 1 - \frac{(x/L)^3}{(X_i/L)^2} \text{ for } 0 \leq x/L < X_i/L \quad (2.1)$$

$$\frac{D - D_2}{D_1 - D_2} = \frac{(1 - x/L)^3}{(1 - X_i/L)^2} \text{ for } X_i/L \leq x/L < 1 \quad (2.2)$$

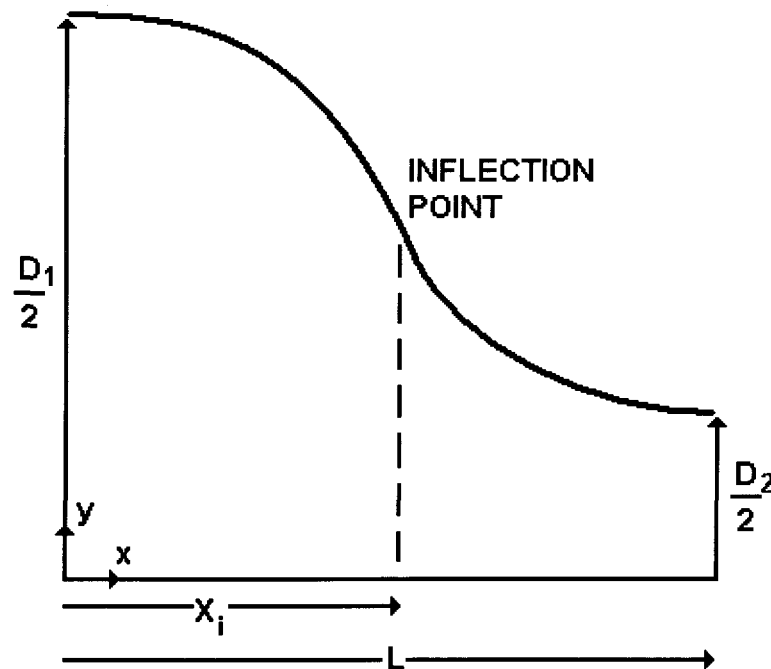


Figure 2.6 Parameters for Contraction Contour using Morel's Equations

For the present work, the equations developed by Morel were modified to apply to a contraction with a rectangular cross-section. The axisymmetric diameters (D) in Morel's equations were replaced with the width and height of the contraction to obtain two different equations defining the vertical and horizontal walls. The inflection point (X_i) was placed at $x = 0.55 L$ based on data provided by Morel (Morel, 1975).

By changing Morel's equations to apply to a contraction with a rectangular cross-section and a changing aspect ratio, the flow will behave differently than for an axisymmetric contraction of the same length and area ratio. For rectangular cross-sections the flow near the walls will migrate laterally, increasing the risk of boundary-layer separation in the corners (Bradshaw & Mehta, 1979). Therefore, the development of the boundary layer near the corners of the contraction should be monitored carefully. For the current contraction design, the cross-section aspect ratio changes from 1 (square) at the inlet to 1.5 at the outlet. A changing aspect ratio means that the pressure gradient is different along the vertical and horizontal walls, but this difference in pressure does not increase the risk of flow separation in the corners of the contraction (Su, 1991).

Morel's equations provide a conservative and well-established method for designing wind tunnel contractions. The experiments performed by Tulapurkara and Bhalla (1988) found that contractions designed using Morel's equations with contraction area ratios varying from 3.464 to 12 provided attached flow with a spatial non-uniformity of $\pm 1\%$ at the contraction outlet. Using the results of Tulapurkara and Bhalla in combination with CFD, Morel's equations were used to successfully design a wind tunnel

contraction at the Technical Institute of Aeronautics in Brazil (Mattos, 2003). A study in 2001 by Chen et al. (2001) on the flow through square-to-square wind tunnel contractions using both experiments and numerical simulations also concluded that contractions designed using Morel's equations provide attached boundary-layer flow along the walls and high spatial uniformity in the test section.

In the present study, the flow through two contractions with wall contours defined using Morel's equations are examined. The first contraction has a length of 2.13 m (84 in.), which is the maximum size that can fit into the available floor space in 3175 ME. The second contraction has a length of 1.14 m (45 in.), and is evaluated to see if uniform flow can be obtained with a shorter contraction length.

2.8.2 Contraction Contour defined using Mikhail/Rainbird's Equations

A second method for defining contraction walls examined in this study was published in 1979 by M. Mikhail and W.J. Rainbird. Their work suggests an optimized wall curvature that reduces the length of the contraction while trying to minimize the risk of flow separation along the walls (Mikhail & Rainbird, 1979). A shorter contraction that maintains high spatial uniformity is desired for this wind tunnel in order to reduce the occupied floor space in 3175 ME. The wall contours of the contraction designed by Mikhail and Rainbird are defined by the second derivative of the wall radius with respect to the axial distance. The equations and variables used to define the wall shape are shown in Figure 2.7.

$$R'' = -A_1(1 + B_1L_1)(\sin(\pi L_1))^{N_1} \text{ for } 0 \leq L_1 \leq 1 \quad (2.3)$$

$$R'' = -A_2(1 + B_2L_2)(\sin(\pi L_2))^{N_1} \text{ for } 0 \leq L_2 \leq 1 \quad (2.4)$$

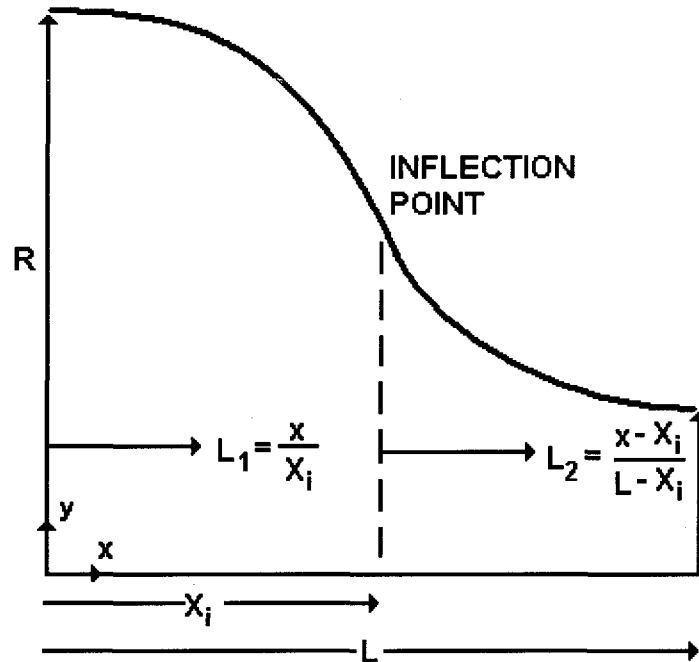


Figure 2.7 Parameters for Contraction Contour using Mikhail/Rainbird's Equations

As with the contraction defined by Morel's equations, these equations were modified to apply to a rectangular contraction with a changing aspect ratio, keeping in mind the consequences of such a modification mentioned in Section 2.8.1. The parameters used to calculate the contraction wall shape using Mikhail and Rainbird's equations are shown in Table 2.1, and were selected to obtain a contraction length of 1.14 m (45 in.).

Table 2.1 Parameters for Contraction using Mikhail/Rainbird's Equations

$0 < L_1 < 1$		$0 < L_2 < 1$	
A ₁ (vertical walls)	1.48	A ₂ (vertical walls)	11.54
A ₁ (horizontal walls)	1.246	A ₂ (horizontal walls)	9.68
B ₁	1.5	B ₂	0
N ₁	0.01	N ₂	3

The CFD predictions of the flow through the contraction defined using Mikhail and Rainbird's equations are compared to the predictions of the flow through a contraction designed using Morel's equations to determine if either design can provide the desired flow quality for a contraction length of 1.14 m (45 in.).

2.8.3 Evaluation of Contraction Geometries Using CFD

2.8.3.1 Reynolds Averaging and Turbulence Modeling in CFD

Computational fluid dynamics is a branch of mathematics that numerically solves for the properties of a fluid flow using the Navier-Stokes equations. Options for solving the equations include direct numerical simulations (DNS) and large-eddy simulations (LES), but both of these methods are expensive in terms of computational power and provide more detail about the turbulence structures of the flow through the contraction than is necessary for the purposes of the present design study. Reynolds-Averaged Navier-Stokes (RANS) equations can be used instead of DNS and LES solutions to calculate the effects of turbulence on the mean flow field using statistical correlations of the turbulence fluctuations, and are more feasible in terms of computational expense.

2.8.3.2 Turbulence Model Selection

One of the most popular turbulence models is the k - ϵ model, which solves for the turbulence kinetic energy (k) and turbulence dissipation rate (ϵ) using partial differential transport equations. It is popular because it is robust and reasonably accurate for flows with zero or small pressure gradients. The model's biggest limitation is that it over-predicts skin friction and is poor at predicting flow separation in adverse pressure gradients (Bardina, Coakley, & Huang, 1997).

The k - ω turbulence model solves for the turbulence kinetic energy and the specific dissipation rate (ω) using partial differential transport equations. It is suggested to be more accurate than the k - ϵ turbulence model at predicting near-wall flows in both adverse and favourable streamwise pressure gradients, but is highly sensitive to free-stream turbulence conditions. (Bardina, Coakley, & Huang, 1997)

The shear stress transport (SST) turbulence model developed by Menter (1994) is one of the more accurate models for predicting the location of boundary-layer separation due to pressure gradients (Nikjoo & Mongia, 1999). This turbulence model combines the k - ω equations in the inner region of the boundary layer with the k - ϵ equations in the wake region of the boundary layer and in the free-stream flow (Nikjoo & Mongia, 1999). Using the k - ϵ equations in the free-stream avoids the problems with free-stream turbulence sensitivity observed with the k - ω turbulence model.

Based on the published data about these two-equation turbulence models, the SST turbulence model was selected to simulate the flow through the wind tunnel contractions in the present study. In the ANSYS CFX commercial CFD software, the boundary layer with the SST turbulence model is treated using a hybrid method that automatically switches from a low-Reynolds-number formulation to wall functions, based on the grid-node spacing provided by the user. For a strict low-Reynolds-number implementation of the turbulence model, the location of the first grid-node off the wall must satisfy the condition of $y^+ < 2$ and there must be at least 15 grid-nodes in the boundary layer (ANSYS, 2009), where y^+ is the wall-normal distance normalized using the kinematic viscosity and the friction velocity. A low-Reynolds-number implementation is desired since wall functions are not accurate in regions with high pressure gradients or in separated flows (Patel, 1984).

The use of a turbulence model to simulate the flow through the wind tunnel contraction assumes that the boundary layer is turbulent over the entire length of the contraction. This implies that the boundary layer flow exiting the flow-conditioning screen is turbulent and there is no laminar flow near the upstream end of the contraction. The effect of this assumption on the predicted flow through the contraction is evaluated by comparing the boundary-layer profiles calculated using the SST turbulence model to boundary-layer profiles calculated imposing laminar flow conditions throughout the contraction.

2.8.3.3 Computational Domain and Boundary Conditions

The computational domain for the simulations of the flow through the contraction was restricted to the contraction volume, with the computational domain starting downstream of the flow-conditioning screen and ending upstream of the test section inlet, as shown in Figure 2.8.

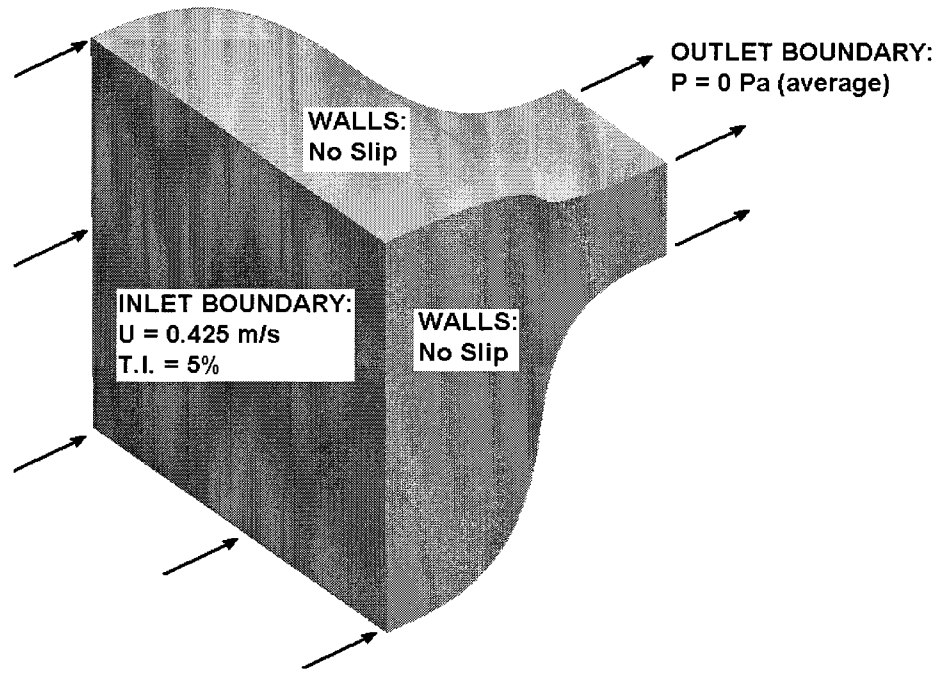


Figure 2.8 Boundary Conditions for Simulations of Flow through Contraction

The contraction geometries were created using ProEngineer, the volumes meshed using ANSYS ICEM and the flows simulated using ANSYS CFX, all of which are commercial software packages.

The velocity at the inlet boundary was calculated based on the desired test section velocity and a contraction area ratio of 11.76, neglecting the boundary-layer development

along the walls. For the grid-convergence study, the velocity at the inlet boundary was set to 0.425 m/s, which corresponds to a test section velocity of 5 m/s. Once a grid-independent solution was obtained, simulations with an inlet boundary velocity corresponding to the slowest test section velocity of 1 m/s were completed. The flow through the contraction for the maximum test section velocity of 10 m/s was not simulated, as the lowest spatial uniformity and highest turbulence levels are expected towards the lower end of the wind tunnel velocity range. A turbulence intensity of 5% was applied arbitrarily at the inlet boundary since the properties of the flow entering the contraction are unknown. Simulations with turbulence intensities ranging from 1% to 10% indicate that the solution calculated using the SST turbulence model is insensitive to the inlet turbulence conditions. A no-slip condition was applied to the contraction walls and the average pressure at the outlet boundary was set to 0 Pa, since for incompressible flows the governing equations only contain terms for the spatial gradients of pressure.

2.8.3.4 Grid Convergence Study

The independence of the CFD results from the selected computational grid was evaluated for the 2.13 m (84 in.) long contraction defined using Morel's equations. The locations of the grid-nodes and inflation layers are shown at the contraction inlet in Figure 2.9 and at the contraction outlet in Figure 2.10. Grid-nodes refer to the vertices of the tetrahedral elements used to define the computational grid throughout the volume of the contraction. Prism elements with triangular cross-sections are stacked closely together near the walls in order to capture the boundary-layer development, and are referred to as inflation layers in ANSYS CFX. The inflation layers are defined by the height of the first

grid-node off the wall, the rate of expansion of the grid-node height and the total number of layers.

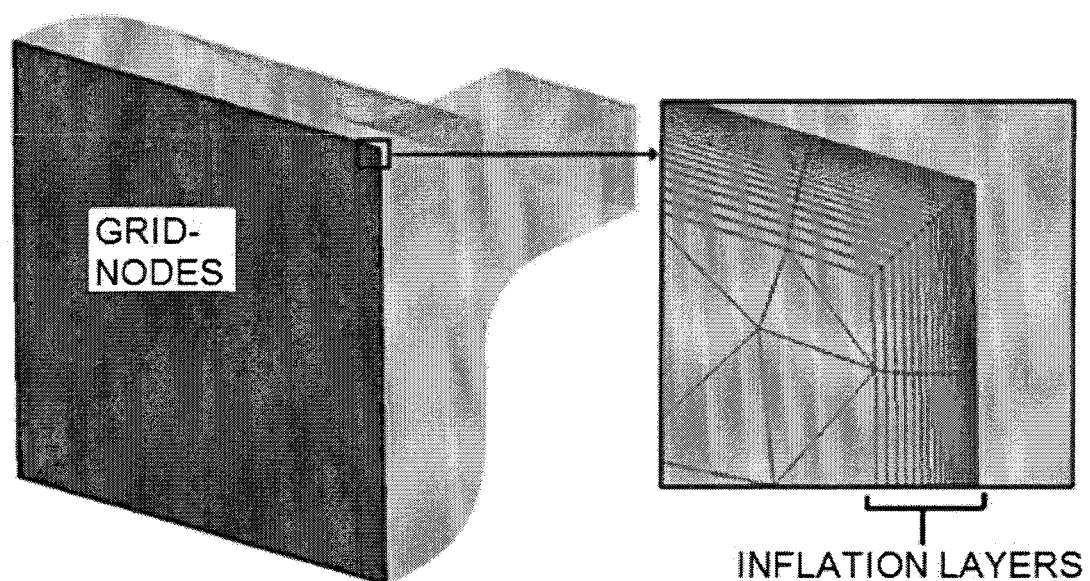


Figure 2.9 Grid-Node Spacing and Inflation Layers at Contraction Inlet

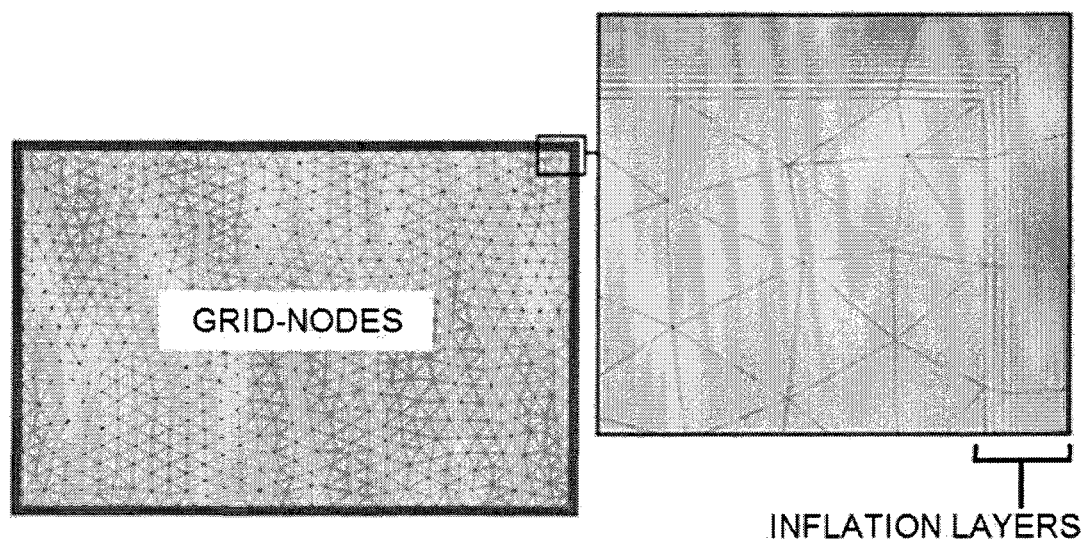


Figure 2.10 Grid-Node Spacing and Inflation Layers at Contraction Outlet

The parameters used to define the grid for each simulation in the grid convergence study are shown in Table 2.2. The centerline velocity (U_C) and maximum velocity (U_{MAX}) at the outlet of the contraction were selected to evaluate the convergence of the solution. If the boundary layer changes significantly and/or separates due to changes in grid-node spacing, there should be noticeable changes in U_C and U_{MAX} at the contraction outlet. The selected criterion for a grid-converged solution is that when the grid-node spacing is halved or the height of the first grid-node off the wall is halved, U_C and U_{MAX} at the contraction outlet should change by less than 1%.

Table 2.2 Contraction Grid Convergence Study Parameters and Results

Simulation	1	2	3	4
Grid-node spacing (mm)	50	25	25	12.5
Total number of inflation layers	10	20	25	20
Expansion factor of inflation layers	1.1	1.1	1.1	1.1
Height of first grid-node off wall (mm)	1.3	0.25	0.13	0.25
Total number of elements	3.1×10^5	1.8×10^6	2.1×10^6	2.2×10^6
U_C (m/s) at outlet plane	4.987	4.992	4.968	5.001
U_{MAX} (m/s) at outlet plane	5.163	5.175	5.126	5.161

The resolution of the first simulation was found to be insufficient to adequately define the boundary layer, so the near-wall grid-node spacing was refined for the second simulation. The second simulation resulted in a well-defined flow, with 21 grid-nodes in the boundary layer at the contraction outlet. The boundary layer was defined as ending when the streamwise velocity is 99% of the centerline velocity. To determine if the results of the second simulation were grid-independent, the height of the first grid-node perpendicular to the wall was halved for the third simulation and the grid-node spacing

was halved for the fourth simulation. The results of the third simulation show a 0.48% increase in centerline velocity and 0.94% decrease in maximum velocity at the contraction outlet. The results of the fourth simulation show a 0.17% increase in centerline velocity and 0.26% decrease in maximum velocity at the contraction outlet. These results indicate that the grid used in the second simulation meets the selected criteria for a grid-independent solution. These grid parameters were also used to discretize the volume of the two shorter contractions designed using Morel's equations and Mikhail and Rainbird's equations.

2.8.3.5 Solution Convergence Study

The solution root-mean-square (RMS) convergence criteria for the continuity, momentum and turbulence partial-differential equations were set to 1×10^{-5} . This value is the root-mean square of the residuals of each transport equation for all the control volumes defined by the elements of the computational domain. The ANSYS CFX solver stops the solution when the RMS residual value for every transport equation within the domain has reached the RMS convergence criteria specified by the user. The effect of the selected convergence criteria on the predicted flow through the contraction was determined by changing the convergence criteria to 1×10^{-6} and examining the resulting U_C and U_{MAX} at the contraction outlet. The simulation results indicate that lowering the RMS convergence criteria by an order of magnitude results in negligible changes in these flow properties at the contraction outlet.

2.8.3.6 Evaluation of Flow through Contraction Designs

The flow properties predicted by the CFD simulations at the contraction outlet for the three different contraction designs are presented in Table 2.3. The flows through both 1.14 m (45 in.) long contractions have higher core-flow non-uniformity and turbulence intensity than the flow through the 2.13 m (84 in.) contraction defined using Morel's equations. The simulation results also indicate that the contraction defined using Mikhail and Rainbird's equations has worse flow quality than the contraction of the same length defined using Morel's equations. Therefore, the walls were defined using Morel's equations and, despite the desire to maximize available floor space in the laboratory, the contraction length was set to 2.13 m (84 in.). Contour plots of the velocity at the outlet of each contraction design are shown in Figures 2.11 to 2.13, with the results normalized by U_C .

Table 2.3 Predicted Flow Properties at Contraction Outlet

Defining Equations	Morel	Morel	Mikhail/Rainbird
Contraction Length (L)	2.13 m	1.14 m	1.14 m
U_{MAX}/U_C	1.04	1.15	1.22
Turbulence Intensity	0.03%	0.2%	0.23%

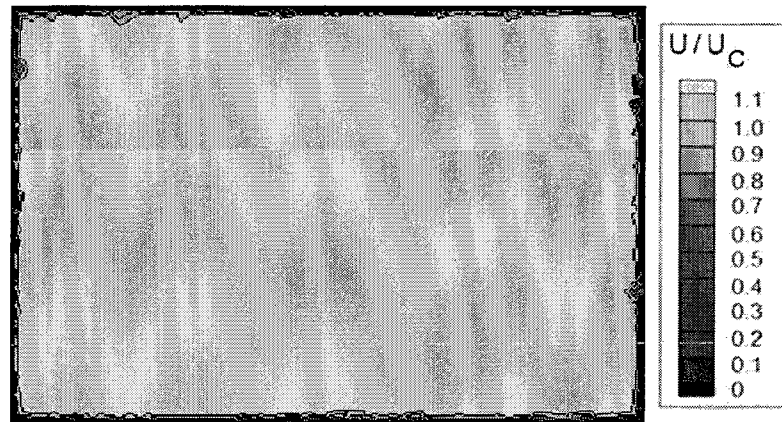


Figure 2.11 Contraction Outlet Velocity Contour Plot: Morel's Equations, $L=2.13$ m

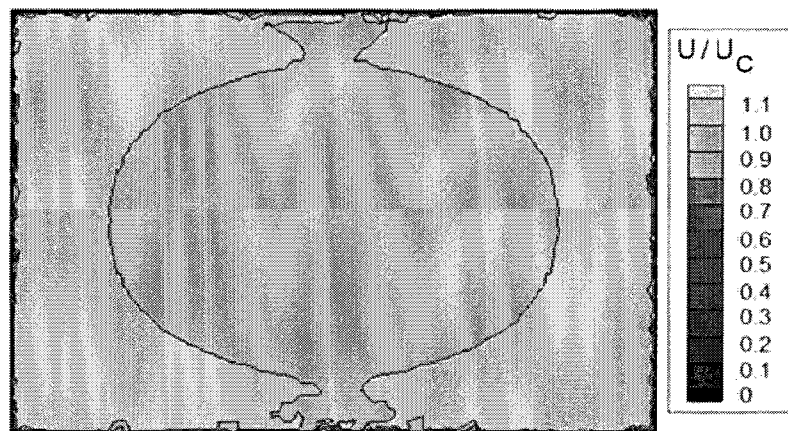


Figure 2.12 Contraction Outlet Velocity Contour Plot: Morel's Equations, $L=1.14$ m



Figure 2.13 Contraction Outlet Velocity Contour Plot: Mikhail's Equations, $L=1.14$ m

The simulations of the flow through the 2.13 m (84 in.) long contraction defined using Morel's equations were repeated for conditions corresponding to a test section velocity of 1 m/s. The simulation results predict a U_{MAX}/U_C of 1.03 and a turbulence intensity of 0.03% at the contraction outlet.

2.8.3.7 Detailed Flow through Selected Contraction Design

The magnitude of the streamwise pressure gradient along the walls of the 2.13 m (84 in.) long contraction defined by Morel's equations is shown in Figure 2.14, for flow conditions corresponding to a test section velocity of 5 m/s.

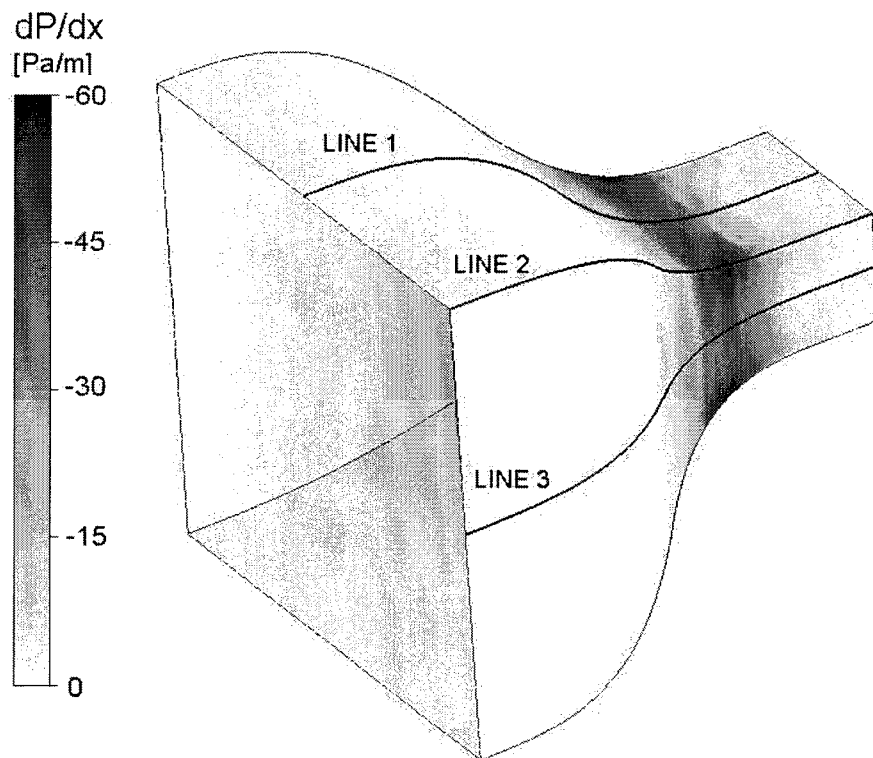


Figure 2.14 Pressure Gradient through Contraction

The change in pressure gradient with streamwise distance along lines 1, 2 and 3 is shown in Figure 2.15. The pressure gradient through the contraction is favourable ($dP/dx < 0$) for $0 < x/L < 0.95$, indicating that the boundary layer is unlikely to separate. There is a small adverse pressure gradient ($dP/dx > 0$) through the contraction for $0.95 < x/L < 1$, indicating the risk of boundary-layer separation increases close to the outlet of the contraction.

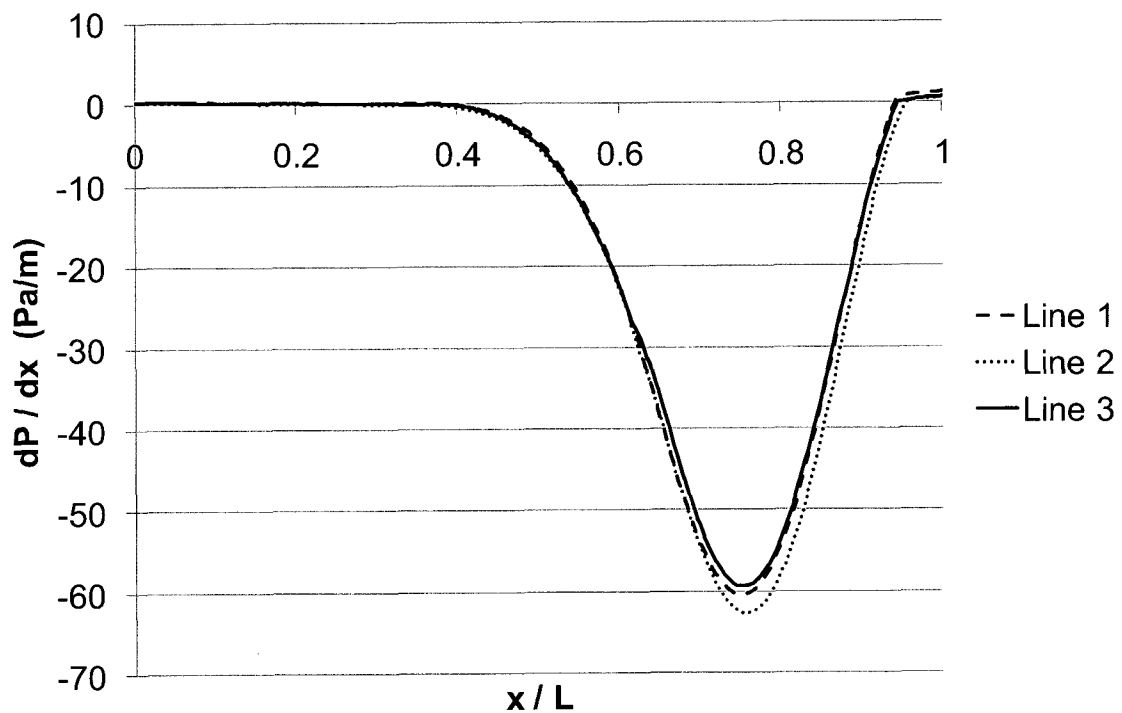


Figure 2.15 Streamwise Pressure Gradient along Length of Contraction

The boundary-layer shape factor (H , Equation 2.5), is used to evaluate how close the boundary layer is to a separated state. The shape factor is defined as the ratio of the boundary-layer displacement thickness (δ^* , Equation 2.6) and the boundary-layer momentum thickness (θ , Equation 2.7).

$$\text{Shape Factor} \quad H = \frac{\delta^*}{\theta} \quad (2.5)$$

$$\text{Displacement Thickness} \quad \delta^* = \int_0^{\infty} \left(1 - \frac{u}{u_{\infty}}\right) dy \quad (2.6)$$

$$\text{Momentum Thickness} \quad \theta = \int_0^{\infty} \frac{u}{u_{\infty}} \left(1 - \frac{u}{u_{\infty}}\right) dy \quad (2.7)$$

The boundary-layer shape factor was calculated along lines 1, 2 and 3 at $x/L = 0.05$ (contraction inlet), $x/L = 0.7$ (region of favourable pressure gradient), and $x/L = 1$ (contraction outlet). The shape factors at these locations are shown in Table 2.4 for simulations using the SST turbulence model and simulations with laminar flow conditions. As mentioned in Section 2.8.3.2, the use of a turbulence model implies that the boundary layer is turbulent along the entire length of the contraction. In reality, the boundary layer is likely laminar at the upstream end of the contraction, and transitions to a turbulent state along the contraction walls downstream. The shape factor under zero streamwise pressure gradient and over a flat surface is expected to be around 2.6 for a laminar boundary layer and 1.4 for a turbulent boundary layer (Gersten & Schlichting, 2004). As the flow approaches separation, the shape factor will increase to 3.7 for a laminar boundary layer and to 2.4 for a turbulent boundary layer (Saleh, 2002).

Table 2.4 Predicted Boundary-Layer Shape Factors in Contraction

Flow Conditions	Turbulent			Laminar		
	1	2	3	1	2	3
Shape Factor ($x/L = 0.05$)	1.53	1.56	1.59	1.74	2.89	1.81
Shape Factor ($x/L = 0.7$)	1.60	1.86	1.54	1.73	2.31	1.74
Shape Factor ($x/L = 1.0$)	1.51	1.82	1.51	2.43	3.16	2.44

The simulations with turbulent and laminar flow conditions both predict that the boundary layer remains attached to the walls along the length of the contraction, with the shape factors indicating that the flow in the corners is closer to separation than the flow along the center of the walls. It is important to note that the shape factor calculation applies only to two-dimensional boundary layers, and that the boundary layers in the corners of the contraction are three-dimensional. Therefore, the calculated shape factors in the corners of the contraction are an approximation of the actual condition of the boundary layer at that location. Simulations with flow conditions corresponding to a test section velocity of 1 m/s also indicate that the boundary layer remains attached along the length of the contraction for both turbulent and laminar flow conditions. Based on the Reynolds number, for lower test section velocities it is possible that the boundary layer remains laminar over the length of the contraction. Since the simulations indicate that the boundary layer remains attached over the entire range of wind tunnel velocities, regardless of whether the flow is turbulent or laminar, the risk of flow separation is considered minimal. The shape factor of the boundary layer at the contraction outlet is measured experimentally during the commissioning of the wind tunnel.

2.8.4 Construction of Contraction

A contraction support structure was designed to support the contraction walls and align the contraction outlet with the test section inlet. The support structure shown in Figure 2.16 was built using steel angles and flats, and is supported by four swivelling casters. The two vertical sections were bolted to the horizontal section, and must be removed to fit the assembly through the doorway.

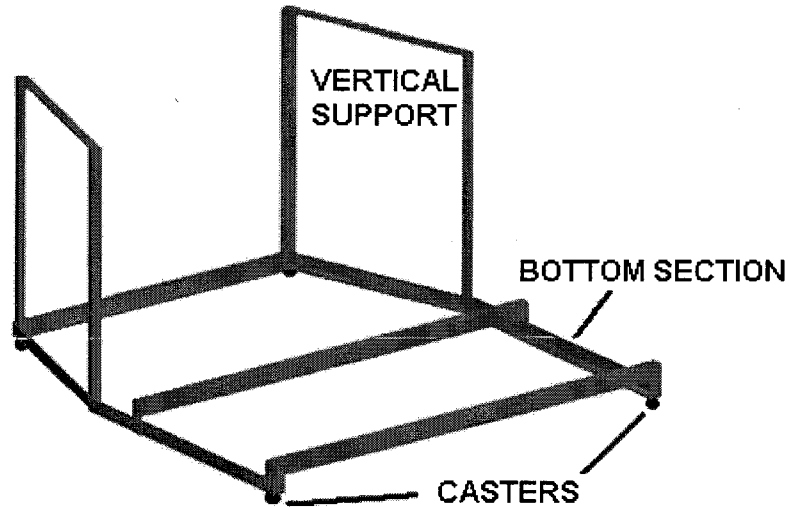


Figure 2.16 Contraction Support Structure

The contraction walls were constructed in a manner that prevents laboratory air from seeping into the low-pressure wind tunnel flow. Each wall assembly was built using plywood ribs overlaid with 3.175 mm (1/8 in.) thick flexible acrylic sheets. The plywood ribs and acrylic sheets were cut to shape using a programmable router in order to produce the desired wall shape and ensure the absence of gaps along the wall edges. Due to the size of the assembly, two acrylic sheets were required to cover each wall, with a seam running streamwise up the center of the wall. Each acrylic sheet is secured to the plywood ribs using small screws with pre-drilled pilot holes to prevent cracking and counter-sinks to prevent the screws from protruding into the flow. The contraction assembly is shown in Figure 2.17.

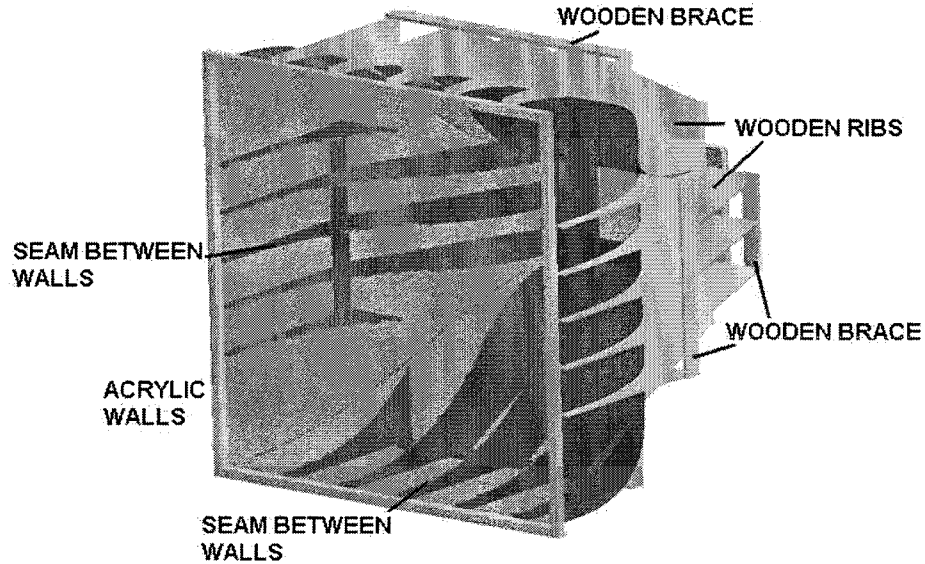


Figure 2.17 Contraction Wall Assembly

2.9 INSTALLATION OF WIND TUNNEL STATIC TAPS

2.9.1 Static Tap Placement

Two static pressure taps were installed in the vertical contraction wall closest to the laboratory entrance to measure the change in static pressure between the contraction inlet and the contraction outlet. With the proper calibration, the difference in pressure between the two static pressure taps ($P_{C1} - P_{C2}$) allows the wind tunnel operator to establish the centerline velocity in the test section without using intrusive pressure probes. The preliminary location of the taps was determined by examining the location of static pressure taps in similar wind tunnels and the geometry of the contraction. The first static pressure tap (P_{C1}) was placed 0.2 m downstream of the contraction inlet where the wall curvature is minimal and the tap is sufficiently downstream to allow the flow to settle after the flow-conditioning screen. The second static pressure tap (P_{C2}) was placed 0.2 m upstream of the contraction outlet where the wall curvature is minimal and the tap is

sufficiently upstream to allow for installation of the turbulence-generating grids for certain future tests.

The CFD results from the contraction design study were used to evaluate the effect of the Reynolds number in the wind tunnel on the pressure coefficient measured by the static pressure taps at these locations. Over the intended velocity range of the wind tunnel, the simulations predict that the pressure coefficient measured at the chosen static pressure tap locations changes by less than 1%. This was considered an acceptable variation in static pressure, so the static pressure taps were placed 0.2 m downstream of the contraction inlet and 0.2 m upstream of the contraction outlet, as shown in Figure 2.18.

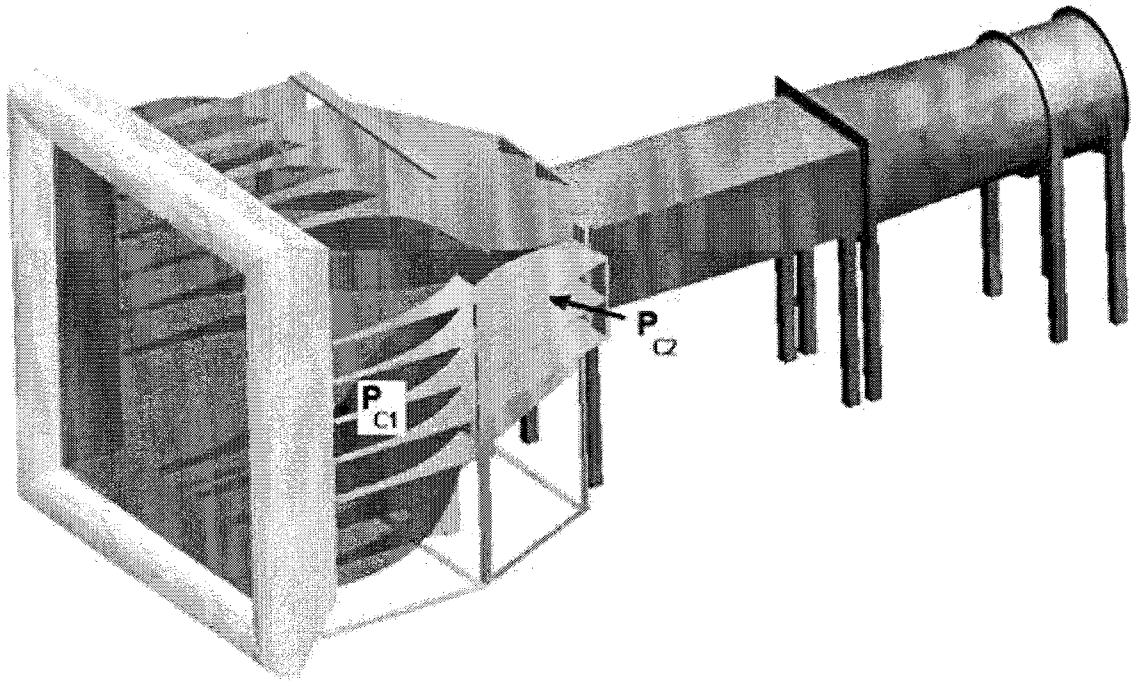


Figure 2.18 Location of Static Pressure Taps in Wind Tunnel

2.9.2 Static Tap Sizing

The static pressure taps were made from cylindrical brass tubing with an inner diameter of 1.58 mm (1/16 in.), an outer diameter of 2.39 mm (3/32 in.) and length of 51 mm (2 in.). The length-to-diameter ratio of the static pressure taps is 32. Static pressure taps with length-to-diameter ratios greater than 4 are known as deep static holes (Chue, 1975). For a deep, square-edged static hole in subsonic flow with a diameter of 1.58 mm (1/16 in.), the measured static pressure is greater than the true wall static pressure by 0.9% of the free-stream dynamic pressure (Chue, 1975). The effect of this error on the pressure measurements pertaining to the commissioning of the wind tunnel are discussed in the relevant sections.

2.9.3 Static Tap Installation

It is critical that the installed static pressure taps are aligned precisely with the contraction wall and have clean edges, as burrs or dirt can cause large errors in the static pressure readings. The static pressure taps are held securely in place with small blocks of wood glued to the wooden ribs and to the contraction wall. For future wind tunnel installations, the static tap support should not be attached to both the wooden ribs and the contraction wall, as there is some flexibility in the structure that could break the tap when the wind tunnel contraction is disassembled for transportation. Photographs of the static pressure taps installed in the wind tunnel are shown in Figure 2.19.

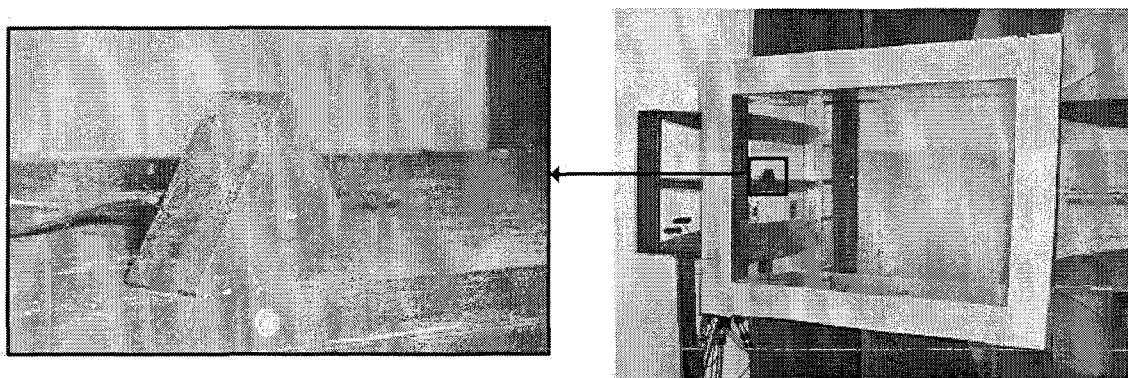


Figure 2.19 Installed Wind Tunnel Static Taps

2.10 ASSEMBLY OF WIND TUNNEL

Due to the size of the laboratory, the pieces for the support structure, contraction walls and inlet have to be brought in and set in place one at a time. The assembly sequence for the contraction is shown in Figure 2.20, and detailed instructions are provided in Appendix C. The instructions for removing the wind tunnel from the laboratory are provided in Appendix D.

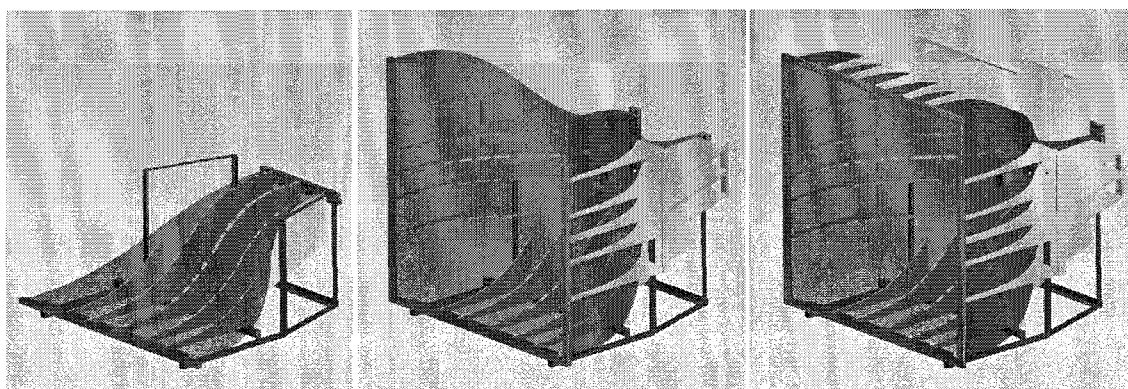


Figure 2.20 Contraction Assembly Procedure

Hardened steel dowel pins located at each corner of the contraction inlet and outlet connect the four wall assemblies together. Steel sleeves for the dowel pins were embedded in the wood to prevent the pins from ripping out and to ensure proper alignment. To prevent air in the laboratory from entering the low-pressure test section, closed-cell foam strips were added between the contraction outlet and test section inlet. The same foam was added between the test section and the transition duct to prevent air leakage between those two sections. A final addition to the wind tunnel was the placement of a net over the entrance to the transition duct as a safety measure to prevent any loose objects in the test section from hitting the fan. Photographs of the constructed wind tunnel are shown in Figure 2.21.

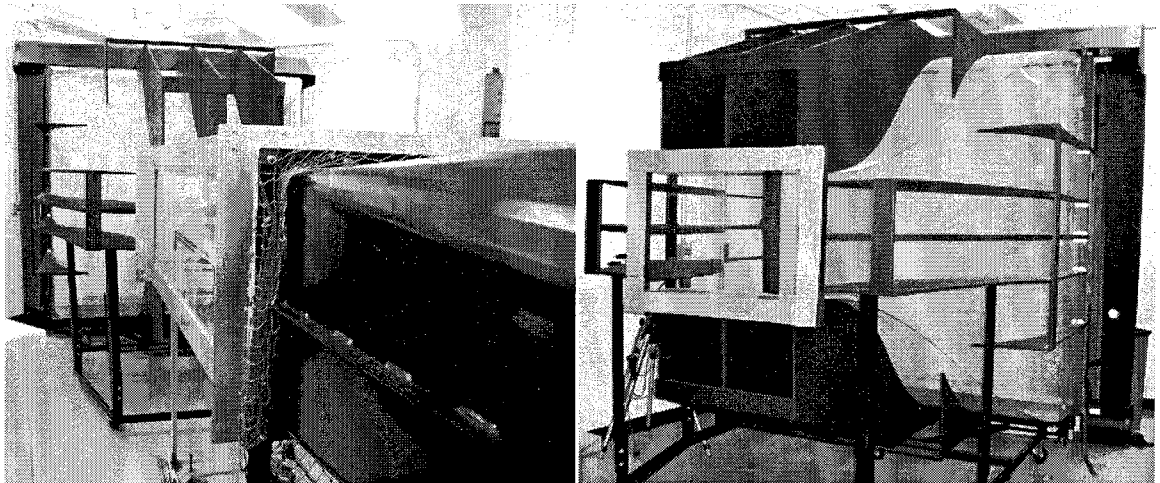


Figure 2.21 Photographs of Constructed Wind Tunnel

2.11 DESIGN OF 3-AXIS TRAVERSE SYSTEM

2.11.1 Traverse System Design Constraints

In order to provide a complete ready-to-use wind tunnel facility, a 3-axis traverse system was designed and installed in 3175 ME. The traverse system must move any measurement probe with a 6.35 mm (0.25 in.) diameter stem through the volume of the wind tunnel test section. The uncertainty in the location of the probe tip due to deformation of the traverse system structure must be less than 0.1 mm under normal operating loads. The traverse system may also be mounted over the water channel test section in 2268 ME; therefore the construction materials must not corrode in a humid environment. Although the traverse system can be mounted on any side of the wind tunnel test section, to be compatible with the water channel facility it must access the test section from above.

The traverse system must provide open access to the test section to allow the operator to easily place models and equipment. The system should be as light as possible to allow for the easy transfer of the traverse system between different facilities and the support structure should be simple to reproduce and mount over any test section. The preliminary design iterations for the traverse system are included in Appendix E.

2.11.2 Detailed Design of Traverse System

The traverse system can be separated into the support structure, streamwise motion components, spanwise motion components and vertical motion components. The design was developed in detail using ProEngineer software to create the solid model

shown in Figure 2.22. Aluminum was selected to build the majority of the components since it does not corrode extensively in a humid environment, is sufficiently strong for the present purpose, and has a low density compared to other corrosion-resistant metals such as stainless steel. Photographs of the traverse system installed in 3175 ME can be found in Appendix F. The wiring diagram for the traverse system motors and details about the user interface developed in Matlab are in Appendix G.

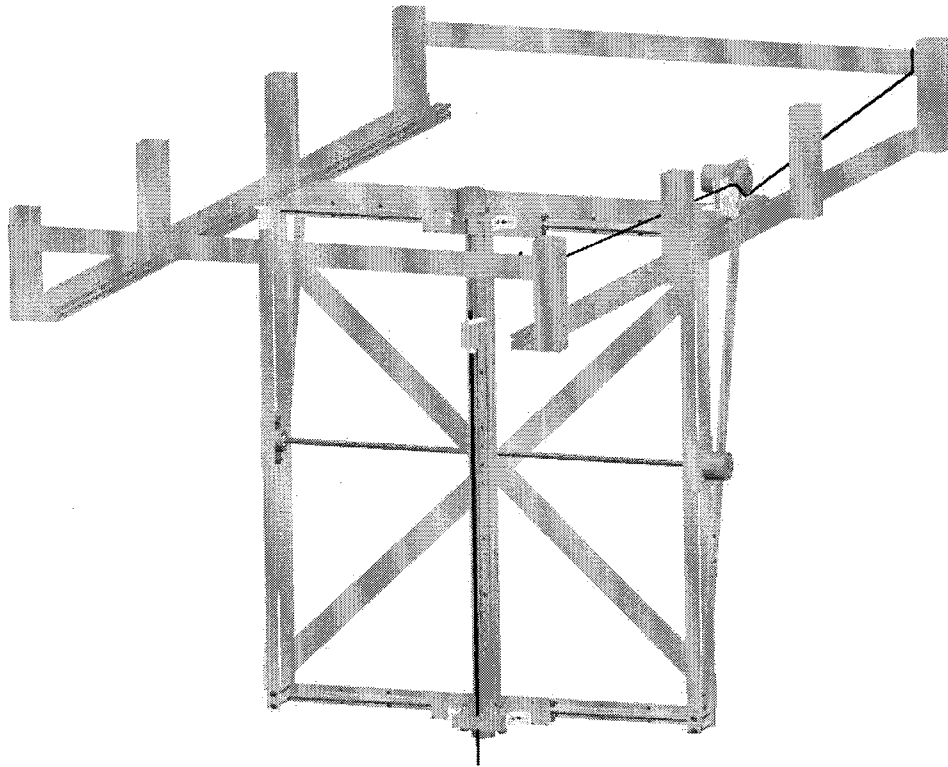


Figure 2.22 Solid Model of Traverse System

2.11.2.1 Traverse System Support Structure Design and Installation

The support structure for the traverse system mounts to the ceiling over the test section. Since the main structure is welded together, the weakest point in the assembly where deflections are most likely to occur is at the attachment to the ceiling. To

strengthen this area, $\frac{1}{4}$ inch thick aluminum angles with a single hole to mount a bolt into an anchor in the ceiling were used as brackets. For the support structure over the wind tunnel facility, the vertical legs were made to fit around the existing lights and ventilation shafts shown in Figure 2.23.

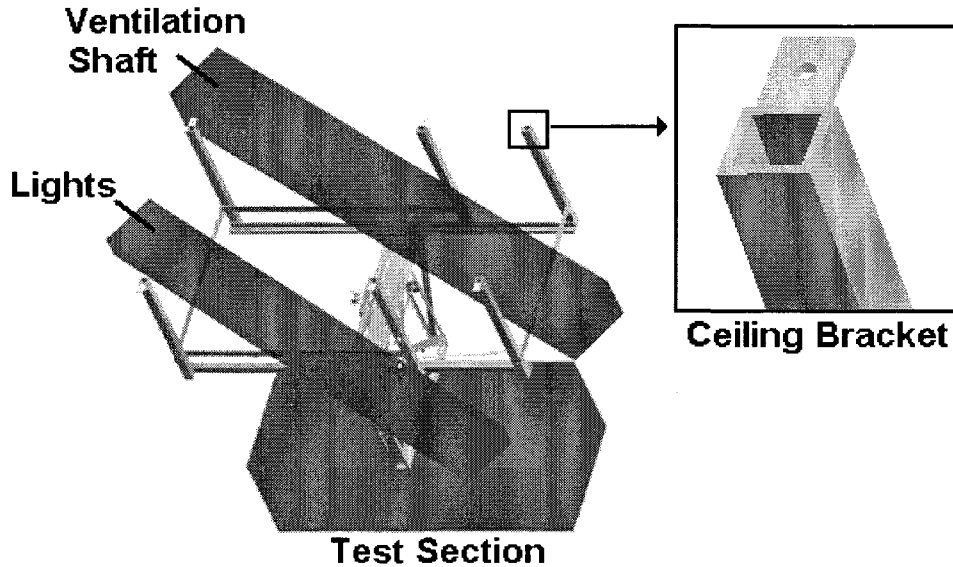


Figure 2.23 Solid Model of Traverse System Support Structure in 3175 ME

2.11.2.2 Traverse System Streamwise Motion Components

The motion of the traverse system in the streamwise (x) direction is generated using rails, guide blocks, a sprocket on a motor, and a chain, as shown in Figure 2.24. Two aluminum rails are mounted on each side of the support structure in the streamwise direction and guide blocks attached to the traverse system allow for smooth movement along the rails. A step motor and sprocket pull the traverse system along a chain mounted on one side of the support structure. For a motor full-step angle of 0.36 deg. and a

sprocket diameter of 55 mm, the motion resolution in the streamwise direction is 0.173 mm.

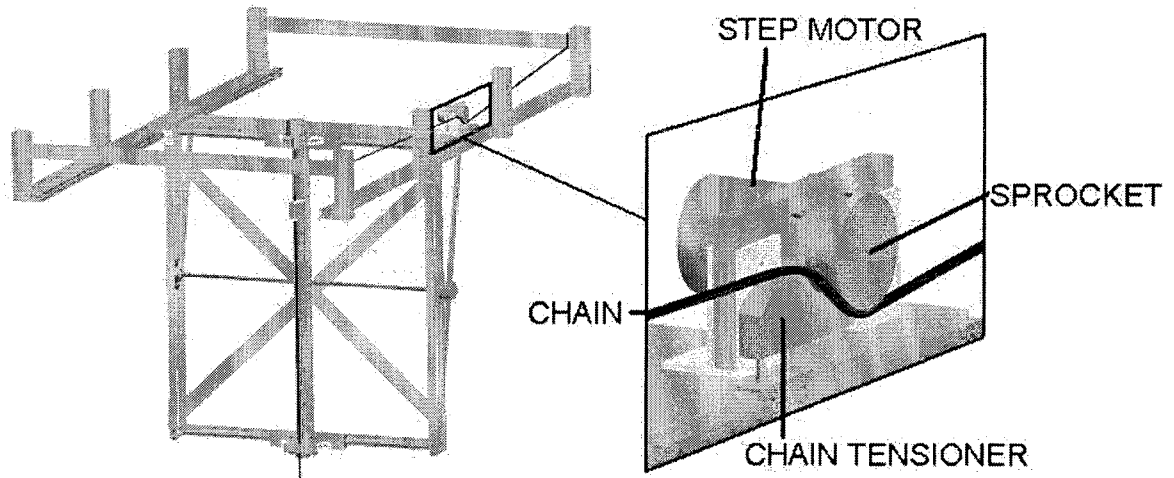


Figure 2.24 Solid Model of Traverse System and Streamwise Motion Components

2.11.2.3 Traverse System Spanwise Motion Components

The motion of the probe in the spanwise (z) direction is generated using a step motor, a threaded rod and a fixed nut, as shown in Figure 2.25. The threaded rod is held to the motor using a zero-backlash coupling at one end and is held by a flanged bearing at the other end. The middle of the rod is threaded through a precision flanged nut that mounts on the channel holding the traverse system components that move the probe in the vertical direction. Turning the threaded rod slides the flanged nut and channel horizontally along shafts at the top and bottom of the traverse system, creating motion in the spanwise direction. For a motor full-step angle of 1.8 deg. and a rod with 10 threads per 25 mm, the motion resolution in the spanwise direction is 0.0125 mm.

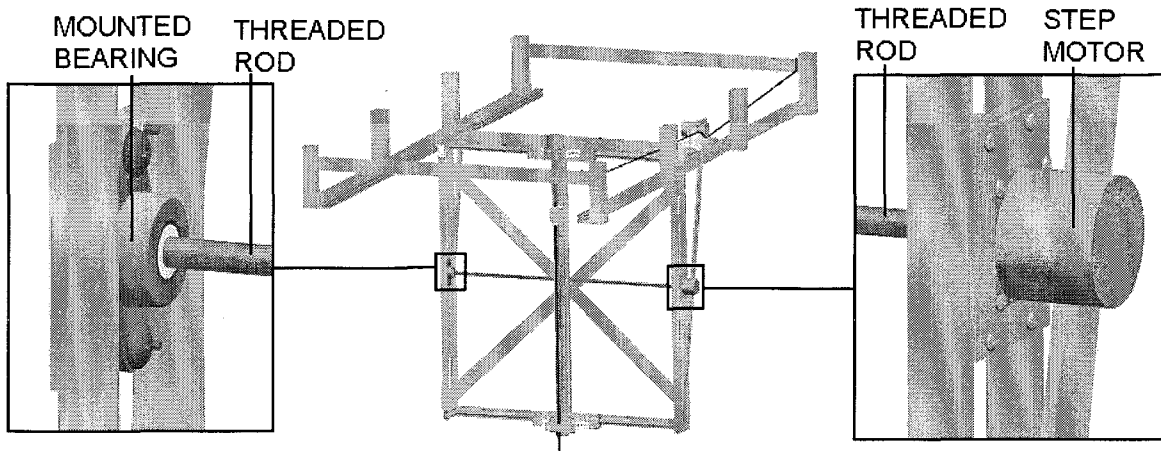


Figure 2.25 Solid Model of Traverse System and Spanwise Motion Components

2.11.2.4 Traverse System Vertical Motion Components

The motion of the probe in the vertical (y) direction is generated using a step motor, a threaded rod and a fixed nut, as shown in Figure 2.26. The middle of the rod threads through a precision flanged nut that mounts on a block holding the probe. Turning the threaded rod slides the block along a vertical rail, moving the probe in the vertical direction. For a motor full-step angle of 1.8 deg. and a rod with 10 threads per 25 mm, the motion resolution in the vertical direction is 0.0125 mm.

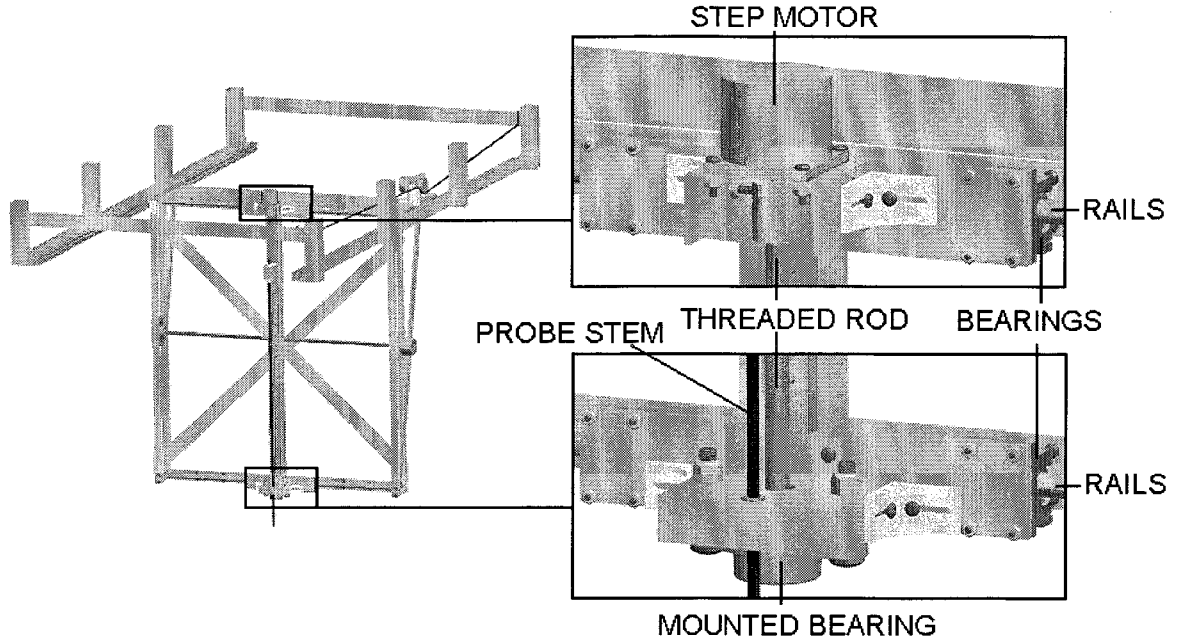


Figure 2.26 Solid Model of Traverse System and Vertical Motion Components

The probe mounting block holds a 6.35 mm (0.25 in.) probe stem using set screws to maintain the orientation and shaft collars to hold the vertical position, as shown in Figure 2.27. The block is interfaced with the vertical threaded rod using a flanged, zero-backlash precision nut.

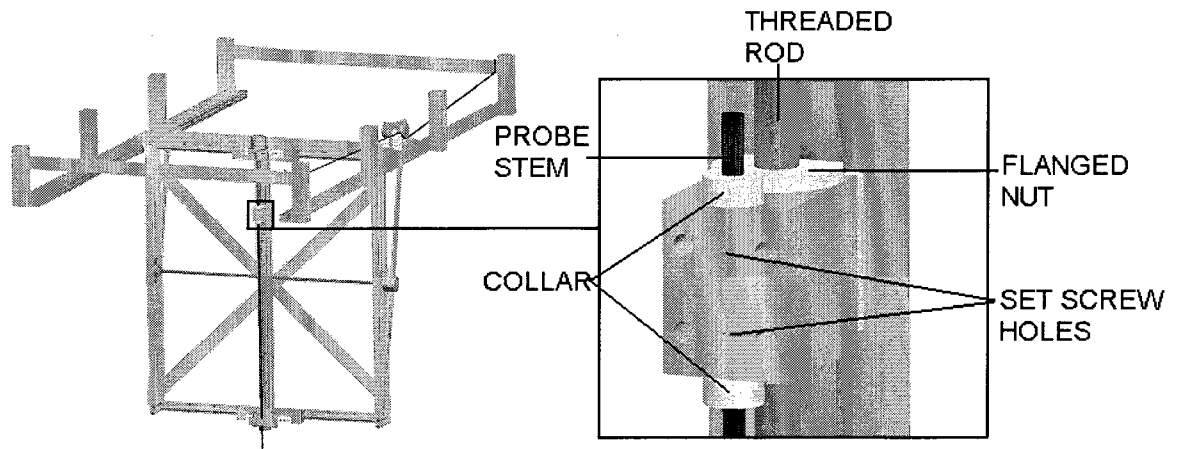


Figure 2.27 Solid Model of Traverse System and Probe Mounting Block

2.11.3 Traverse System Deflection under Load

The traverse system was evaluated using ProE Mechanical software to estimate the deflections in the traverse system structure under load. The computed deflections were used to optimize the traverse system design prior to its construction. Once constructed, the traverse system was subjected to maximum loads of 22.24 N (5 lb.), 44.48 N (10 lb.), and 66.72 N (15 lb.) in the spanwise, vertical and streamwise directions. The resulting deflections were measured to determine the positioning accuracy of the constructed traverse system for typical wind tunnel operating conditions. The deflection of the support structure was only measured in the vertical direction, since the main load on the support structure is the weight of the traverse system.

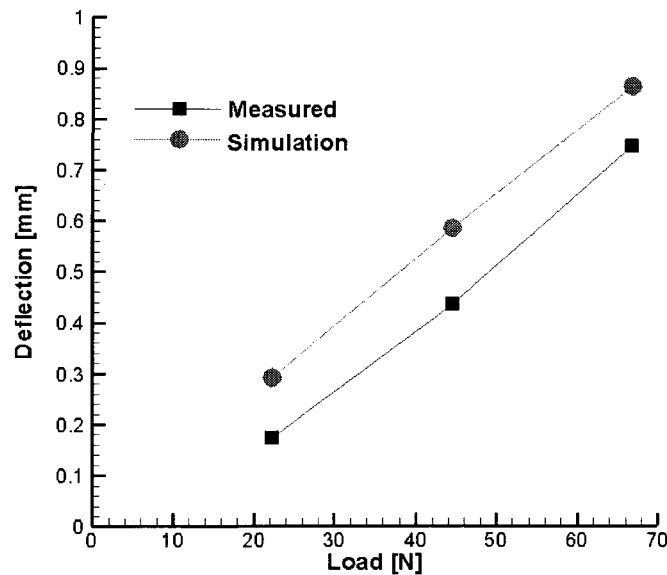
2.11.3.1 Traverse System Deflection in Streamwise Direction

During operation of the wind tunnel, the drag force on the probe stem in the streamwise direction was estimated assuming the probe stem is a 6.35 mm (0.25 in.) diameter cylinder in cross-flow and extends halfway into a given test section. The drag was calculated for the maximum test section velocities in three different experimental facilities where the traverse system is likely to be used. The coefficient of drag was selected based on the Reynolds number of the flow over the probe stem (Kundu & Cohen, 2004). The expected drag force on a probe stem of the given dimensions installed in the three different experimental facilities is shown in Table 2.5. The results show that the highest drag force on the probe stem is 2.43 N and occurs in the high-speed wind tunnel.

Table 2.5 Drag Force on Probe Stem in Streamwise Direction

Facility	U_{MAX}	Fluid	Probe Stem Length	Re_D	C_D	Drag
Low-speed wind tunnel	10 m/s	Air	0.25 m	5050	1	0.097 N
High-speed wind tunnel	50 m/s	Air	0.25 m	20250	1.2	2.43 N
Water channel	0.3 m/s	Water	0.40 m	1480	1	0.118 N

The deflection of the bottom of the constructed traverse system in the streamwise direction was measured by applying loads to the bottom corner of the traverse system in the +x direction, with the top of the traverse system clamped to the rails to prevent motion in the streamwise direction during the tests. For the ProE Mechanical simulations, one side of the traverse system was fixed where it interfaces with the rails in the x, y, and z directions, and the other side was fixed in the y and z directions but allowed to move freely in the x direction. The measured deflections and the deflections predicted by the ProE Mechanical simulations in the streamwise direction are presented in Figure 2.28.

**Figure 2.28 Streamwise Deflections in Traverse System under Load**

The results show that the deflections in the streamwise direction are less than originally anticipated by the computer simulations. Extrapolating from the measured deflections in the streamwise direction, the maximum drag force of 2.43 N on the probe stem should result in a deflection in the traverse system structure of 0.026 mm in the +x direction. Based on the dimensions of the traverse system and a probe stem length of 0.25 m, this results in a change in the location of the probe tip by 0.033 mm in the +x direction. This deflection does not include deflection due to flexibility in the probe stem.

2.11.3.2 Traverse System Deflection in Spanwise Direction

The deflection of the bottom of the constructed traverse system in the spanwise direction was measured by applying the loads to the bottom corner of the traverse system in the +z direction. For the ProE Mechanical simulations, both sides of the traverse system were fixed where it interfaces with the rails in the x, y, and z directions. The measured deflections and the deflections predicted by the ProE Mechanical simulations in the spanwise direction are presented in Figure 2.29.

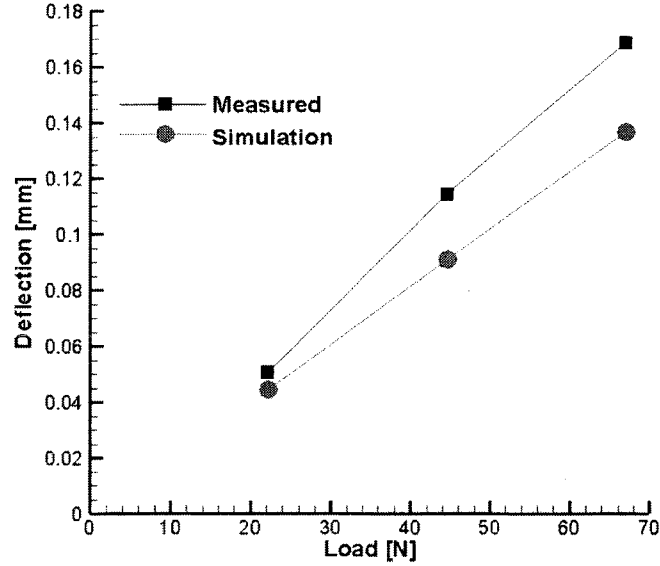


Figure 2.29 Spanwise Deflections in Traverse System under Load

The results show that the deflections in the spanwise direction are larger than originally anticipated by the computer simulations. The extra deflection in the constructed traverse system is likely due to looseness in the brackets that attach the traverse system to the rails. These deflections should not affect the positioning accuracy of the probe since there are no direct loads on the structure in the spanwise direction during normal operation of the wind tunnel.

2.11.3.3 Traverse System Deflection in Vertical Direction

The deflection of the support structure is caused by the 222.4 N (50 lbs) weight of the traverse system. The uncertainty in the probe's vertical position as it moves along the length of the support structure is determined by measuring the deflection of the support structure under the weight of the traverse system at different points along the rails. The stiffest points in the support structure are at the posts that connect to the ceiling, and the

weakest points are midway between the posts, as indicated by labels A and B in Figure 2.30.

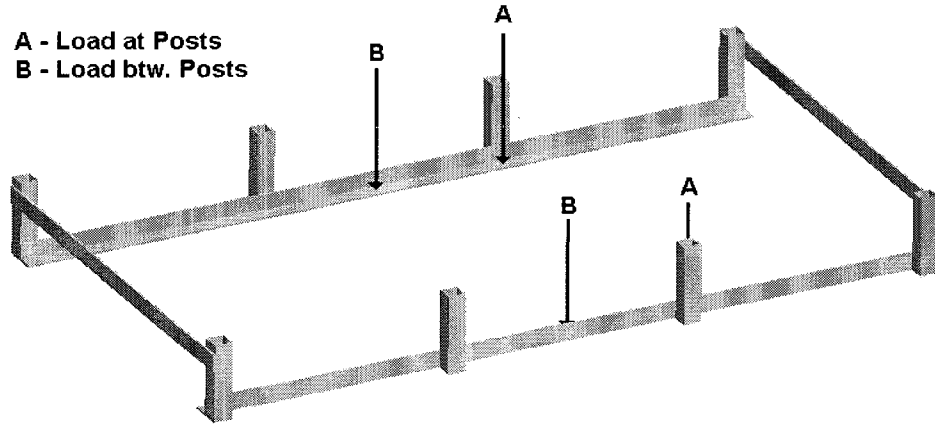


Figure 2.30 Location of Loads on Traverse System Support Structure

Computer simulations using ProEngineer Mechanical software indicate that under a 222.4 N load, the support structure deflects 0.561 mm when the load is applied at the posts (A) and 0.593 mm when the load is applied between the posts (B). Therefore, the vertical position of a probe can be expected to change by up to 0.032 mm as the traverse system moves in the streamwise direction. For the ProE Mechanical simulations, the ceiling mounting brackets of the support structure were fixed at the center of their mounting holes in the x and y, and z directions. The deflection in the constructed support structure in the vertical direction was measured by loading the support structure at point B. The measured deflections and the deflections predicted by the ProE Mechanical simulations are presented in Figure 2.31.

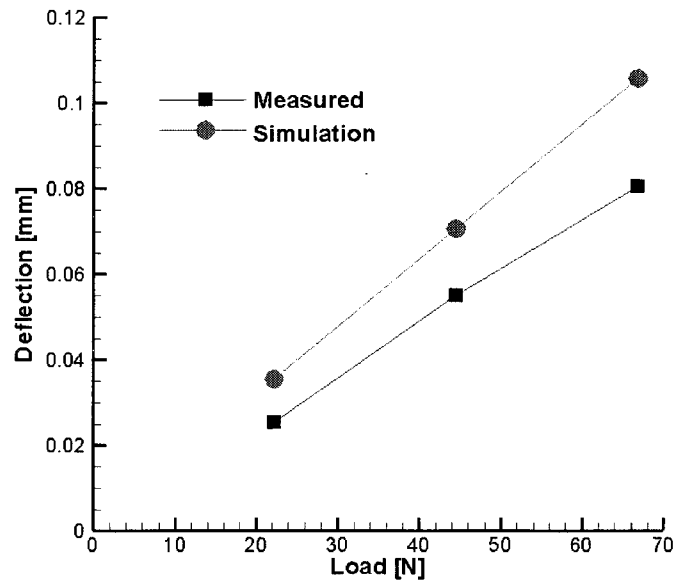


Figure 2.31 Vertical Deflections in Support Structure under Load

The results indicate that the support structure deflections in the vertical direction are less than originally anticipated by the computer simulations, likely due to the added stiffening created by the rails mounted on the support structure. Extrapolation from the measured deflections indicates that the uncertainty in vertical position as the traverse system moves along the rails should be less than the 0.032 mm predicted using computer simulations. It was not possible to physically measure the change in support structure deflection as the traverse system moves along the rails in the streamwise direction due to difficulty in obtaining an absolute measurement reference along the length of the rails.

The deflection of the constructed traverse system (including the support structure) in the vertical direction was measured by applying loads to the bottom corner of the traverse system in the $-y$ direction, with the traverse system located at point B. For the ProE Mechanical simulations, both sides of the traverse system were fixed where it

interfaces with the rails in the x, y, and z directions. The measured deflections in the traverse system, including the deflections in the support structure, are compared to the deflections predicted by the ProE Mechanical simulations in Figure 2.32.

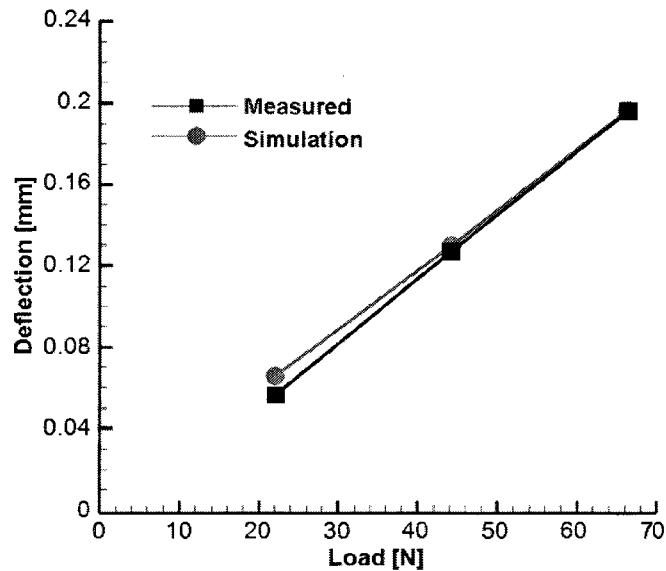


Figure 2.32 Vertical Deflections in Traverse System under Load

The results show that the deflections in the vertical direction are less than or equal to the deflections calculated by the computer simulations. These deflections in the vertical direction should not affect the positioning accuracy of the probe since the only load on the traverse system in the vertical direction is the weight of the probe, which is a small fraction of the weight of the traverse system and remains constant.

2.11.4 Range and Accuracy of Probe Placement

Accurate positioning of the probe depends on the motor stepping without slipping in a given direction and the backlash in the couplings that connect the step motors to the threaded rods. The linear motion in the streamwise, spanwise and vertical directions was measured by rotating the motor in each axis a set number of steps and measuring the resulting displacement. This process was repeated multiple times and for varying numbers of steps to ensure repeatability of the results. The measured displacement per step matches the expected displacement within the 0.0254 mm (0.001 in.) resolution of the measurement instrument, indicating that there is no slippage between the motors and any of the mechanical couplings in the vertical or spanwise directions.

During operation of the wind tunnel, the step motor had difficulty moving the traverse system in the streamwise direction due to friction between the brackets and the rails. The friction can be reduced by loosening the brackets, but doing so allows for rotation about the vertical axis of the traverse system that wedges the traverse system onto the rails and prevents motion in the streamwise direction. A slight force applied by the operator at the bottom of the traverse system in the direction of motion was found to be sufficient to overcome the friction and allow the traverse system to move in the streamwise direction. To improve the traverse system, it is recommended that a lubricant such as WD-40 be applied along the rails and that a larger sprocket be installed to increase the torque generated by the step motor.

The backlash in the streamwise, spanwise and vertical directions was measured by rotating each motor a set number of steps, and then rotating the motor the same number of steps in the opposite direction. This process was repeated a number of times in each axis to obtain a measurable displacement of the traverse system from its original position due to backlash in the mechanical couplings. The backlash in the vertical and spanwise directions originates in the mounted nuts that attach to the threaded rods, despite the fact that they were advertised as ‘zero-backlash’ nuts. A summary of the travel distance, positioning resolution, backlash per turn, and uncertainty in the location of the probe tip due to normal operating loads is shown in Table 2.6.

Table 2.6 Summary of Traverse System Motion Capabilities

Direction	Travel Distance	Deflection in Structure under Normal Operating Loads	Resolution	Backlash
Streamwise	1.83 m	0.033 mm	0.173 mm	0 mm
Spanwise	0.61 m	0 mm	0.0125 mm	0.00095 mm
Vertical	0.91 m	0.032 mm	0.0125 mm	0.00588 mm

2.12 SUMMARY OF WIND TUNNEL DESIGN AND CONSTRUCTION

The low-speed wind tunnel currently being designed has an open-circuit configuration and is designed in a modular fashion to allow it to be disassembled, moved to another laboratory and reassembled without damaging the wind tunnel structure. The flow enters the wind tunnel through a flow-conditioning screen to dampen unsteady flow motions in the laboratory environment. The contraction walls were designed using Morel’s equations and a length of 2.13 m (84 in.) to provide a flow with high spatial uniformity and low turbulence at the contraction outlet. Two contractions designed with

shorter lengths were shown in simulations to provide poor flow uniformity and high turbulence intensity at the contraction outlet. The test section is 0.508 m (20 in.) high, 0.762 m (30 in.) wide and 1.778 m (70 in.) long, and is compatible with the closed circuit wind tunnel in 3224 ME. The fan was sized to provide a test section velocity up to 10 m/s and was obtained from a commercial supplier. A 3-axis traverse system was designed to hold a measurement probe with a 6.35 mm (0.25 in.) diameter stem and move it over the entire volume of the test section is the final component of the wind tunnel. The capabilities of the traverse system were evaluated by measuring the structure deformation under load, the backlash and the positioning accuracy in all three axes.

The total cost of the materials to build the wind tunnel contraction and inlet was \$1600 and the total cost to build to traverse system plus its support structure over both the wind tunnel and water channel facilities was \$3300. Detailed cost breakdowns are provided in Appendix H.

2.13 INTRODUCTION TO WIND TUNNEL COMMISSIONING

The goal of commissioning the wind tunnel is to provide a complete description of the flow entering the test section over a range of operating conditions. This includes determining the spatial non-uniformity and turbulence intensity of the flow entering the test section and the properties of the boundary layer along the perimeter of the test section inlet. Due to the small size of the wind tunnel laboratory, the effect of the proximity of the wind tunnel inlet to the laboratory walls on the flow is also evaluated.

2.14 INSTRUMENTATION USED IN WIND TUNNEL COMMISSIONING

2.14.1 Description of Instrumentation

A pitot-static pressure probe was used to measure the time-averaged velocity properties of the flow entering the test section. The pitot-static pressure probe was inserted between the test section and the contraction, with closed-cell foam strips filling the gap between the two sections. Due to the length of the probe, the measurements were taken 0.2 m into the contraction instead of exactly at the interface between the contraction and test section, as shown in Figure 2.33. At the measurement location, the simulations of the flow through the contraction indicate that the pressure gradient is close to zero. Therefore, the measurements from the pitot-static pressure probe taken 0.2 m into the contraction may be assumed to represent the flow at the inlet of the test section.

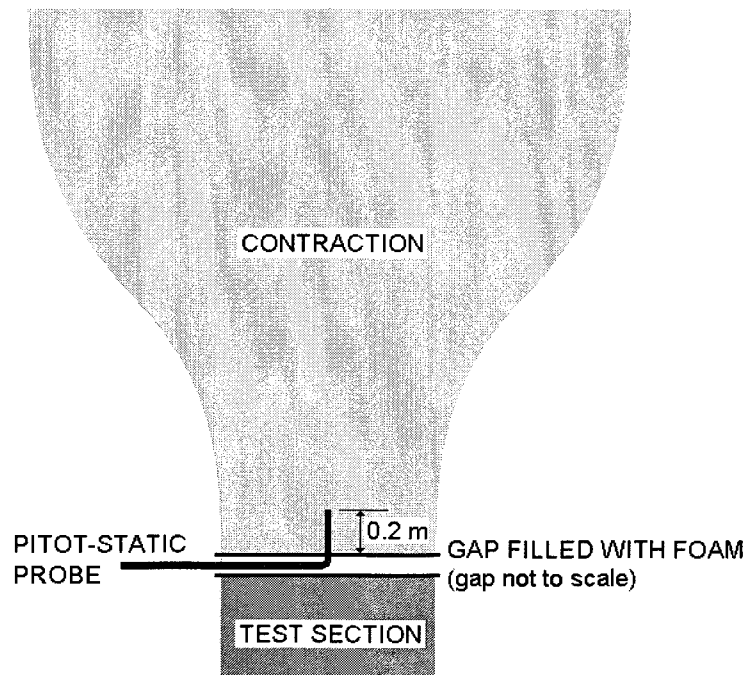


Figure 2.33 Location of Pitot-Static Pressure Probe (Top View)

The properties of the pitot-static pressure probe are provided in Table 2.7. Assuming that flow misalignment is due solely to the slope of the contraction walls, the misalignment of flow at the tip of the pitot-static pressure probe should not be more than ± 2.5 deg. For a pitot-static pressure probe with a hemisphere tip, the measured velocity should be accurate to within 2% of the actual velocity for misalignment angles up to ± 30 deg. (Chue, 1975). This level of accuracy is achieved over the given range of misalignment angles because the errors in the measured total and static pressures offset each other. The results of Chue (1975) were confirmed in the present study by placing the pitot-static pressure probe at the center of the test section and varying its inclination from -10 deg. to $+10$ deg. in 1 deg. increments, with the probe angle set using a digital level with a resolution of 0.1 deg. Over the range of angles tested, the velocity measured by the pitot-static pressure probe remained within 1.5% of the zero-yaw velocity, confirming the results of Chue (1975).

Table 2.7 Pitot-Static Pressure Probe Properties

Tip shape	Hemisphere
Outer diameter	7.94 mm
Inner diameter	2.77 mm
Number of static taps	8 (45 deg. separation)
Distance from probe tip to static taps	70 mm

A pitot-total pressure probe was used to measure the boundary-layer velocity profiles at the outlet of the contraction. The properties of the pitot-total pressure probe are provided in Table 2.8. Based on the range of expected Reynolds numbers in the test section, the calibration curves presented by Chue (1975) indicate that this pitot-total pressure probe is capable of measuring the stagnation pressure with an accuracy of $\pm 2\%$.

The pitot-total pressure probe has a finite diameter; therefore the measured stagnation pressure is the average stagnation pressure over the area of the probe opening. Due to the velocity gradient across the tip of the probe and the fact that the stagnation pressure is proportional to the square of the velocity, the measured stagnation pressure is higher than the stagnation pressure at the geometric center of the probe opening (Chue, 1975). As well, the blockage introduced by the pitot-total pressure probe causes the flow streamlines to deflect towards the region of lower velocity near the wall (Chue, 1975). The deflection of the flow also results in a measured stagnation pressure higher than that existing in the same location in the absence of the probe. From the given dimensions of the pitot-total pressure probe, the combination of the above two effects creates a measurement displacement error of less than 0.128 mm (Chue, 1975), or 1.28% of the boundary-layer thickness based on CFD simulations for a test section velocity of 5 m/s.

Table 2.8 Pitot-Total Pressure Probe Properties

Cross-section	Circular
Tip shape	Square-edge
Outer diameter	1.6 mm
Inner diameter	0.8 mm

Two inclined manometers were used to measure the pressures from the pitot-static pressure probe, pitot-total pressure probe relative to P_{C2} , and difference between the contraction wall static pressure taps. Preliminary calculations indicated that the manometers should be inclined at a 1:25 ratio, which is their maximum inclination and provides the best resolution. The largest uncertainty in the pressure measurements is due to the 1 mm resolution of the inclined manometers. The uncertainty is equal to half the

resolution and based on the specific gravity (SG) of the fluid in each manometer it is ± 0.162 Pa (SG = 0.826) or ± 0.196 Pa (SG = 1).

2.15 WIND TUNNEL STATIC TAP CALIBRATION

The calibration coefficient (K), defined as the ratio of the centerline dynamic pressure (q) to the pressure difference between the two contraction static pressure taps ($P_{C1}-P_{C2}$), allows the wind tunnel operator to calculate the velocity along the centerline of the test section through measurement of $P_{C1}-P_{C2}$ in subsequent wind tunnel tests. The value of K was established by measuring the centerline dynamic pressure simultaneously with the value of $P_{C1}-P_{C2}$ during the commissioning of the wind tunnel. The measurement results, shown in Figure 2.34, follow a linear trend line over the dynamic pressure range of interest. During the wind tunnel commissioning the majority of the tests were completed at lower fan speeds, accounting for the lack of measurements at higher dynamic pressures. By performing tests both with and without the flow-conditioning screen in place, it was determined that the calibration coefficient is independent of the presence of the flow-conditioning screen.

As mentioned in Section 2.9.2, the pressure measured by the contraction static pressure taps is greater than the true wall static pressure by 0.9% of the free-stream dynamic pressure. Since the free-stream dynamic pressure is larger at P_{C2} than at P_{C1} , the measured value of $P_{C1}-P_{C2}$ is less than the actual value of $P_{C1}-P_{C2}$. Incorporating this error into the calculation of K, the resulting calibration coefficient $K = q_c/(P_{C1}-P_{C2}) = 0.97$ (± 0.04 for a 95% confidence level).

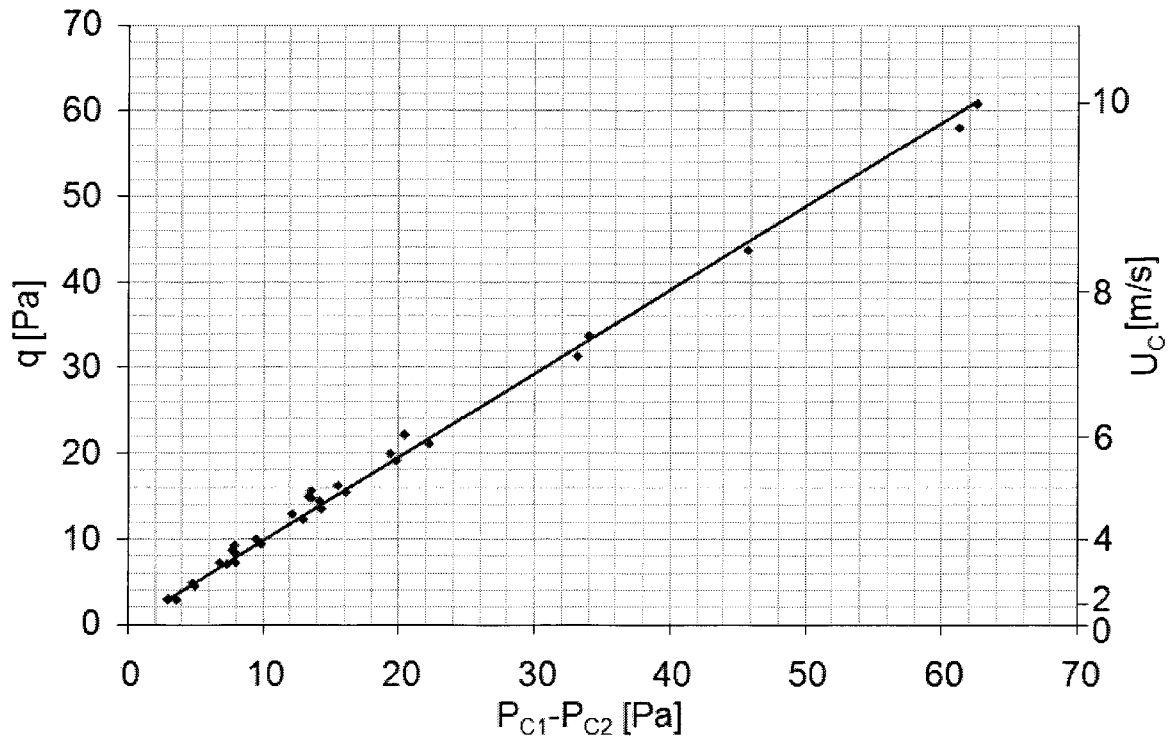


Figure 2.34 Calibration of Contraction Wall Static Pressure Taps

2.16 WIND TUNNEL TEST CONFIGURATIONS

A range of tests were performed to evaluate the velocity uniformity of the flow entering the test section under different operating conditions. Both a test section with a flat ceiling and constant cross-section, shown in Figure 2.35, and a test section with a contoured ceiling, shown in Figure 2.36, were placed in the wind tunnel to establish the location of the undisturbed-flow plane at the test section inlet that can serve as the reference flow condition in planned studies with the contoured-ceiling test section. The contoured ceiling creates a non-symmetric pressure profile over the cross section of the test section since only the ceiling is contoured and the other three walls are flat.

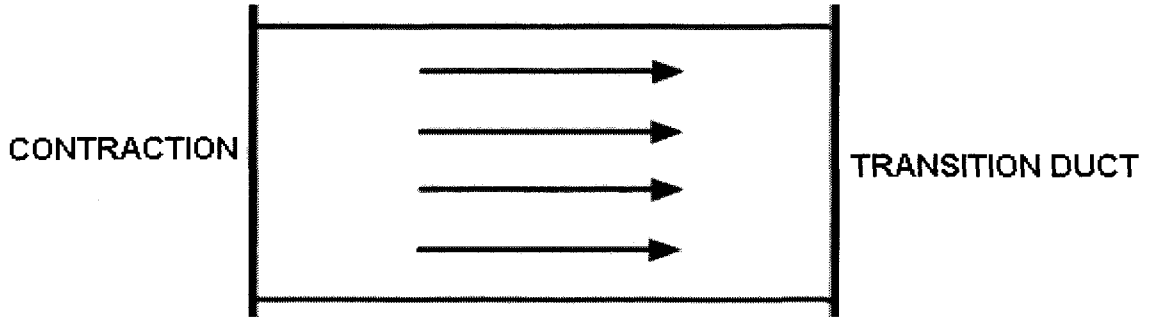


Figure 2.35 Test Section Profile with Flat Ceiling

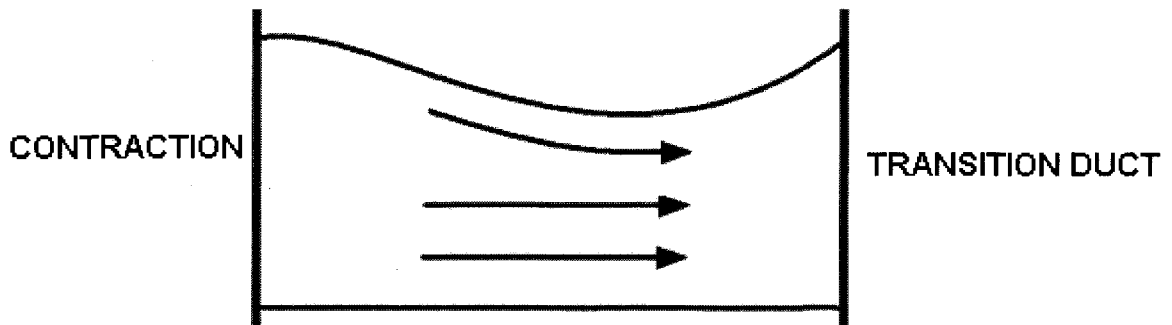


Figure 2.36 Test Section Profile with Contoured Ceiling

The effect of the proximity of the wind tunnel inlet to the laboratory walls on the flow entering the test section was evaluated by changing the position of the wind tunnel with respect to the walls and measuring the spatial uniformity of the resulting flow. The position of the wind tunnel inlet was measured from each corner of the inlet to the nearest wall, as shown in a top-view of the wind tunnel in Figure 2.37. The difference in wall spacing between sides 1 and 2 ($\Delta 1 - \Delta 2$) was increased during the tests from 0 m to 0.2 m, with the average distance $((\Delta 1 + \Delta 2)/2)$ maintained at 0.3 m.

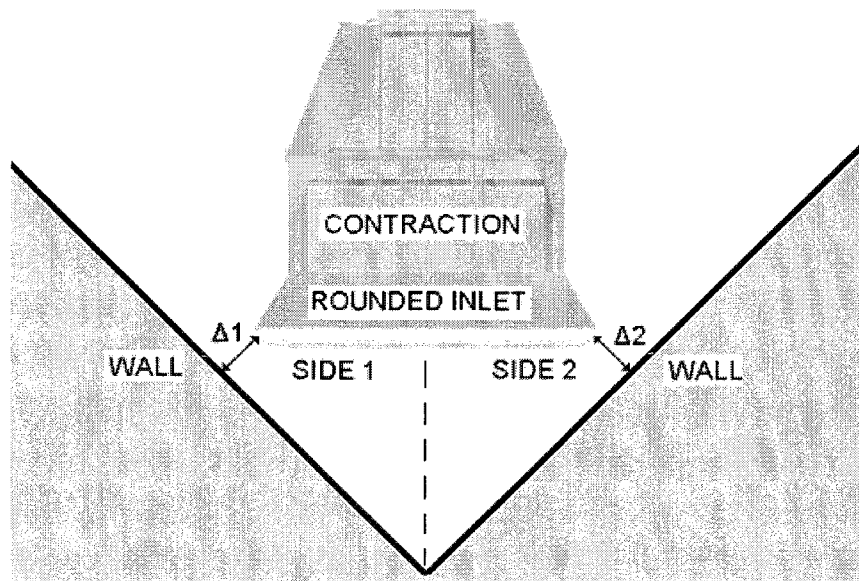


Figure 2.37 Contraction-to-Wall Spacing Measurement Locations

The spatial uniformity of flow at the test section inlet was measured for each configuration using a rectangular grid with 25 points. The measurement points were selected to exclude the boundary-layer regions along the walls of the test section inlet. The non-uniformity in the velocity at the test section inlet due to the proximity of the wind tunnel inlet to the laboratory walls was defined as the ratio of the average velocity on side 1 of the test section to the average velocity on side 2 of the test section. The results were non-dimensionalized with respect to the centerline velocity (U_C) at the test section inlet. During the commissioning tests, the flow in the test section was varied from 3 m/s to 10 m/s. Although the wind tunnel was intended for use from 1 m/s to 10 m/s, the limited resolution of the manometers would not allow for accurate measurements at lower test section velocities.

2.17 MEASURED WIND TUNNEL BOUNDARY-LAYER PROFILES

The properties of the boundary layer along the wall at the inlet of the test section and their variation along the perimeter of the test section inlet were used as indicators of the quality of the contraction design. The boundary-layer profiles for three different wind tunnel configurations are compared in Figure 2.38, with equal spacing from each side of the wind tunnel inlet to the laboratory walls. Boundary-layer profiles for other wind tunnel velocities and configurations are provided in Appendix I. The results are non-dimensionalized with respect to the centerline velocity of the test section (U_C), and the boundary-layer profiles are offset by 0, 1 and 2 for clarity.

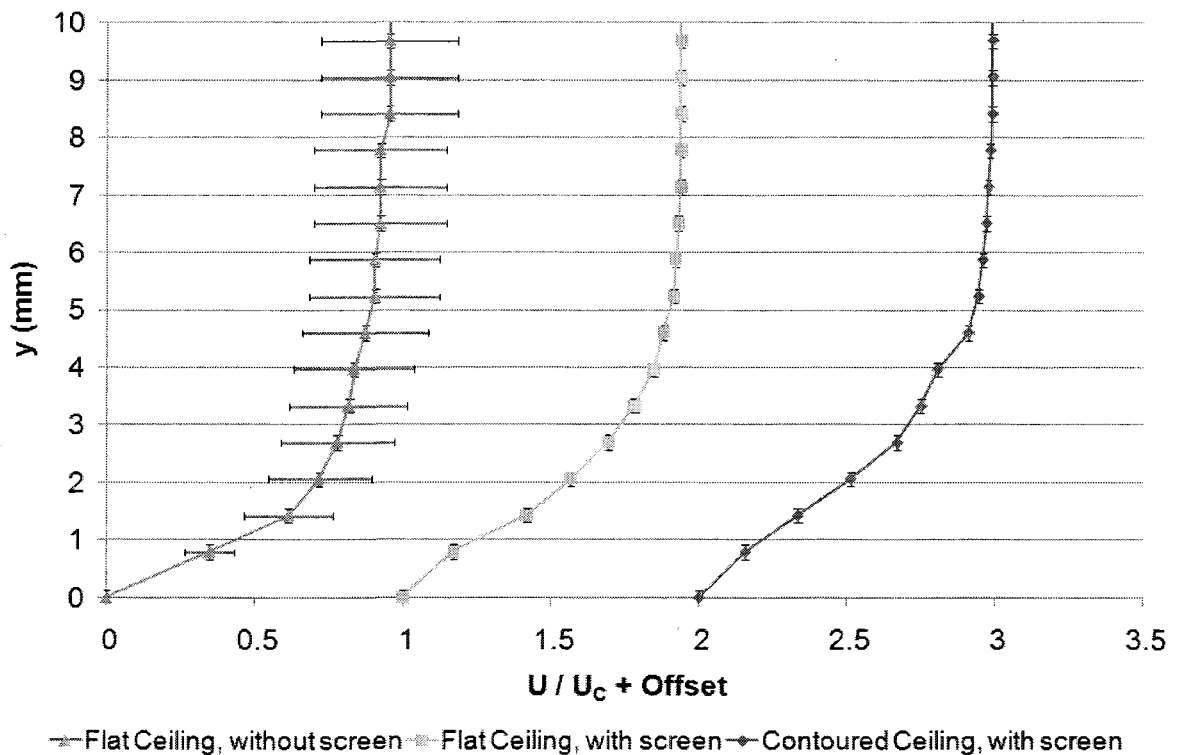


Figure 2.38 Boundary-Layer Profiles at Test Section Inlet

The boundary layer was measured using the pitot-total pressure probe referenced to P_{C2} . As mentioned in Section 2.9.2, the static pressure measured by P_{C2} is greater than the true wall static pressure by 0.9% of the free-stream dynamic pressure. This error introduces a pressure offset dependent on the test section velocity, but otherwise does not affect the velocity profile of the boundary layer. The horizontal error bars are based on the visually observed fluctuations in the manometer readings. In the configurations with the flow-conditioning screen in place, the fluctuations in the manometer readings were smaller than could be observed by the human eye. The vertical error bars are based on the effects of the finite-sized pitot-total pressure probe on the boundary layer flow, as mentioned in Section 2.14.1.

The measured boundary-layer displacement thickness is 2.0 mm for a test section velocity of 5 m/s, which is comparable to the displacement thickness of 1.85 mm calculated from the CFD simulation results using the SST turbulence model. Significant fluctuations in velocity were observed in the boundary-layer profiles with the flow-conditioning screen removed, with a mean fluctuation $\pm 24.2\%$ of the time-averaged local velocity. These results suggest the presence of the flow-conditioning screen is necessary to reduce unsteadiness in the flow. Therefore, only the flow uniformity measurements with the flow-conditioning screen in place are included in the following sections.

2.18 MEASURED WIND TUNNEL BOUNDARY-LAYER SHAPE FACTORS

The shape factor of the boundary layer was calculated from experimental data using the definition of the parameter provided in Section 2.8.3.7. The measured shape factors of the boundary layer entering the test section, with the flow-conditioning screen in place, vary from 2.26 for a test section velocity of 3 m/s to 1.88 for a test section velocity of 10 m/s. The measured shape factors indicate that the boundary layer remains attached to the walls at it exits the contraction. Due to the fluctuations in velocity, it was not possible to accurately calculate the shape factor with the flow-conditioning screen removed.

2.19 MEASURED FLOW UNIFORMITY AT TEST SECTION INLET

The flow uniformity at the test section inlet was evaluated with the flat-ceiling test section, the flow-conditioning screen installed and equal distance of 0.3 m from each side of the wind tunnel inlet to the laboratory walls (Configuration 1). The standard deviation of velocity at the test section inlet remains within $\pm 1.5\%$ of U_C over the entire range of test section velocities. The maximum velocity of the flow entering the test section is $1.036 U_C$, a value that is comparable to the value of $1.04 U_C$ predicted by CFD simulations during the design stage of the wind tunnel contraction. The mean velocity on side 1 of the test section is 0.45% higher than the mean velocity on side 2 for equal wall spacing. The contour plot of the velocity at the test section inlet for Configuration 1 is shown in Figure 2.39, with the values between the measured data points obtained from linear interpolation.

During the commissioning of the wind tunnel, it was observed that the tension of the flow-conditioning screen has a significant effect on the flow entering the test section. The flow-conditioning screen was re-tensioned after a number of wind tunnel test results showed a decrease in velocity at the center of the top and the bottom of the test section inlet. Contour plots of the velocity before the screen was re-tensioned are presented in Appendix J.

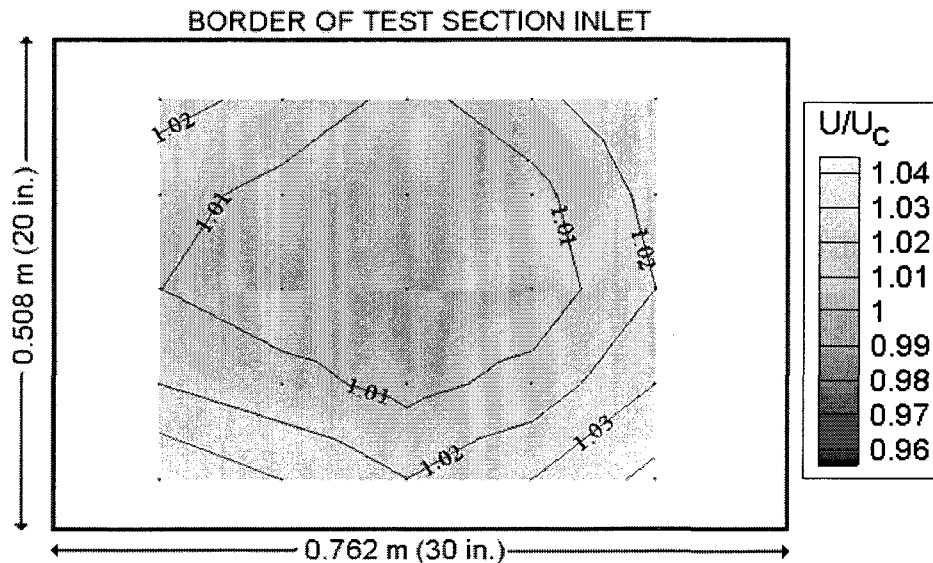


Figure 2.39 Velocity Uniformity at Test Section Inlet for Configuration 1

The effect of the test section ceiling configuration on the upstream flow was evaluated using the test section with the contoured ceiling, with the flow-conditioning screen in place and equal distance from each side of the wind tunnel inlet to the walls (Configuration 2). The standard deviation of velocity at the test section inlet remains within $\pm 1.5\%$ of U_C over the entire range of test section velocities. The maximum velocity measured in the test section is $1.041 U_C$, which again corresponds well with the

flow predictions from the CFD simulations. The contour plot of the velocity at the test section inlet for Configuration 2 is shown in Figure 2.40. The decrease in velocity at the center of the top and bottom of the test section inlet is caused by the un-even tensioning of the screen, as these measurements were taken before the screen tension was adjusted.

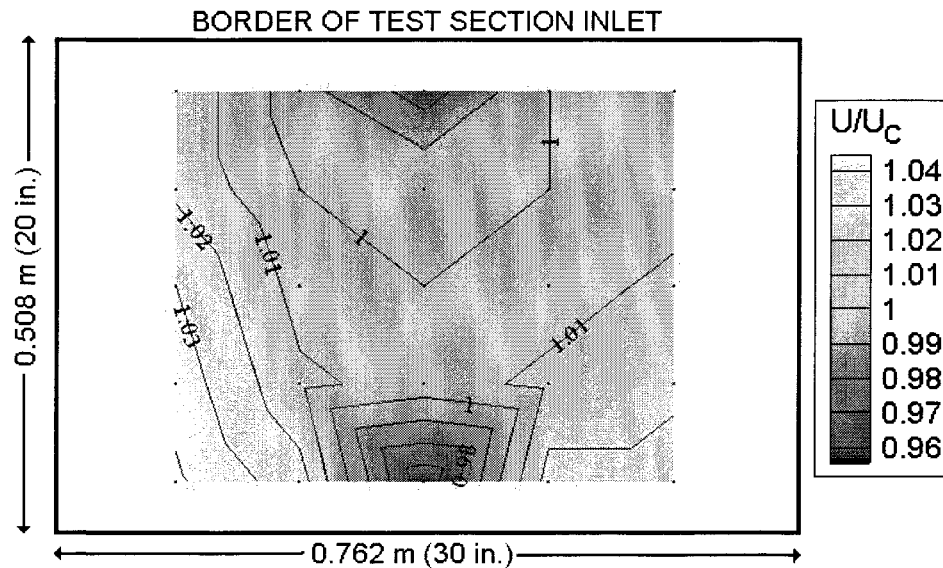


Figure 2.40 Velocity Uniformity at Test Section Inlet for Configuration 2

The non-uniformity with Configuration 2 is similar in magnitude to the non-uniformity calculated with Configuration 1, indicating that the ceiling profile of the test section does not significantly influence the uniformity of the flow at the test section inlet. However, the contoured-ceiling test section does block a portion of the test section flow as indicated by the need to increase the fan speed to maintain the same mean velocity. Despite this flow blockage, it is recommended that the velocity at the test section inlet plane be used to obtain the reference flow conditions for wind tunnel configurations with the contoured-ceiling test section.

The effect of the proximity of the wind tunnel inlet to the laboratory walls on the test section flow was evaluated for a difference in wall spacing ($\Delta 1 - \Delta 2$) of 0.2 m and an average wall spacing $((\Delta 1 + \Delta 2)/2)$ of 0.3 m, using the empty, flat-ceiling test section with the flow-conditioning screen in place (Configuration 3). The standard deviation of velocity at the test section inlet remains within $\pm 1.5\%$ of U_C over the entire range of test section velocities. The contour plot of the velocity at the test section inlet for Configuration 3 is shown in Figure 2.41.

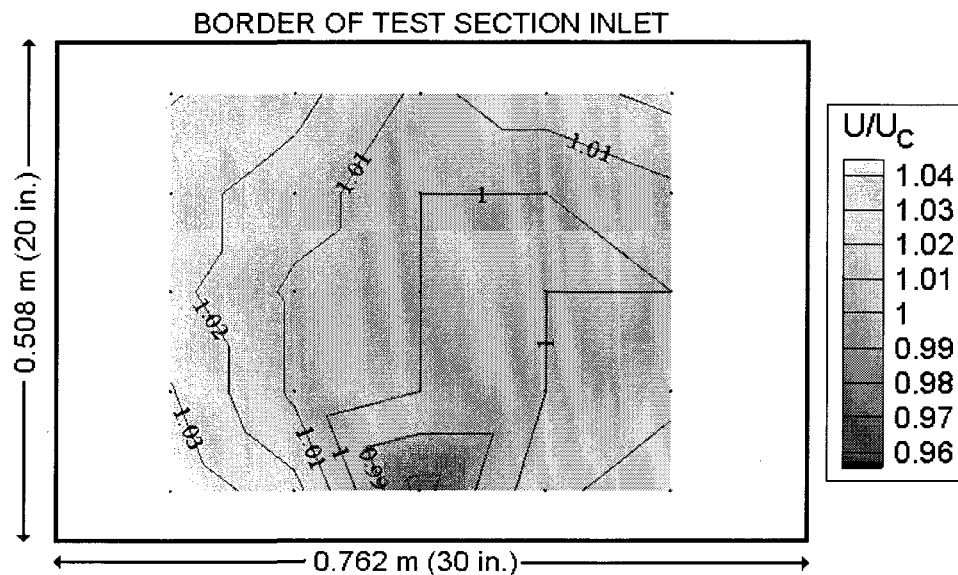


Figure 2.41 Velocity Uniformity at Test Section Inlet for Configuration 3

The velocity on side 1 of the test section is 1.45% higher than on side 2, compared to a 0.45% difference for $\Delta 1 = \Delta 2$ and a 0.49% difference for $\Delta 1 - \Delta 2 = 0.1$ m. The details of the flow for a difference in walls spacing of 0.1 m are presented in Appendix J. The results indicate that the distance from each side of the wind tunnel inlet to the wall does affect the overall flow uniformity, and for the most spatially-uniform test section

flow, the difference between $\Delta 1$ and $\Delta 2$ should be less than 0.1 m for an average wall spacing of $((\Delta 1 + \Delta 2)/2) = 0.3$ m.

2.20 MEASURED TURBULENCE INTENSITY AT TEST SECTION INLET

The turbulence intensity of the flow entering the test section was measured using an in-house, constant-temperature hotwire anemometer with frequency response of 15 kHz. The single-wire hotwire sensor was operated with a hot-to-cold sensor resistance ratio of 1.6. The signal from the hotwire anemometer was sampled at a frequency of 10 MHz for periods of 0.05 s by a LeCroy Wavejet 324 oscilloscope, which processes the signal using an 8-bit analog-to-digital converter. The measured signal was processed digitally to remove high-frequency noise, the details of which are presented in Appendix K. The resultant uncertainty in the measured turbulence intensity of the flow is estimated to be $\pm 0.04\%$ for a test section velocity of 1 m/s and $\pm 0.01\%$ for a test section velocity of 10 m/s.

The turbulence intensities measured along the centerline of the test section are presented in Figure 2.42. At the lowest measured wind tunnel velocity of 1.65 m/s, the turbulence intensity in the test section is less than 0.24% ($\pm 0.028\%$). Although slightly above the target turbulence intensity of 0.1%, the measured turbulence intensities are of the same order of magnitude and were achieved through proper design of the wind tunnel contraction and transition duct, without the use of turbulence-reducing screens that wind tunnels typically require to reduce turbulence levels.

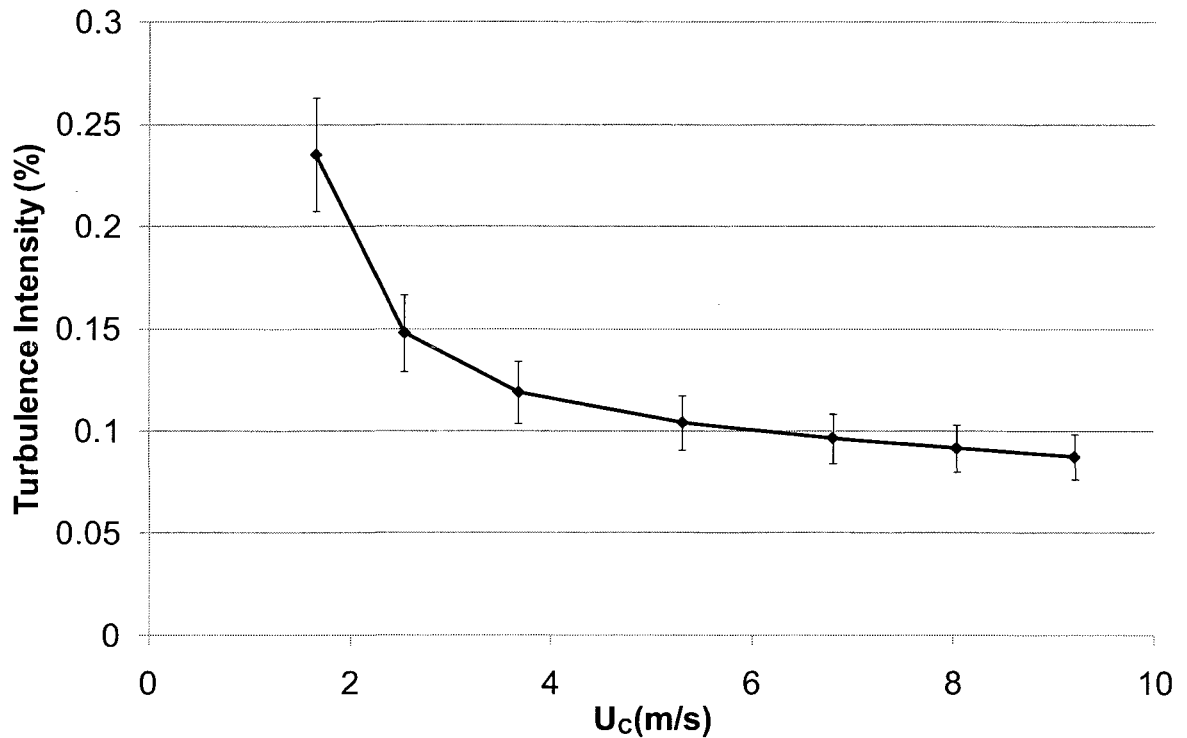


Figure 2.42 Variation in Turbulence Intensity with Wind Tunnel Velocity

2.21 SUMMARY OF WIND TUNNEL COMMISSIONING

The behaviour of the wind tunnel was recorded to provide a complete description of the flow entering the test section. The centerline dynamic pressure was related to the pressure difference between the contraction static pressure taps, and this relationship was shown to be independent of the flow Reynolds number over the velocity range of the wind tunnel. Measurements of the boundary layer at the test section inlet indicate that the flow-conditioning screen upstream of the contraction is necessary to dampen unsteady flow motions, and that the boundary layer remains attached and of a substantially full profile as it enters the test section. The standard deviation of the velocity over the core region of flow at the test section inlet remains within $\pm 1.5\%$ of the centerline velocity over the entire range of operating conditions tested. To maintain this level of spatial

uniformity, the distances from each side of the wind tunnel inlet to the walls should be within 0.1 m of each other and the average distance from the inlet to these two walls should be greater than 0.3 m. Although the measured spatial uniformity of the core flow does not meet the target uniformity of $\pm 0.5\%$, it is still acceptably low and can be expected to improve if the wind tunnel is moved to a larger laboratory. The turbulence intensity of the core flow entering the test section varies from 0.24% for a test section velocity of 1.65 m/s to 0.09% for a test section velocity of 9.2 m/s. The target turbulence intensity of 0.1% for test section velocities from 1 m/s to 5 m/s was not achieved, but the measured turbulence intensity is of the same order of magnitude and considered acceptable. These flow conditions were achieved through proper design of the wind tunnel contraction and transition duct, without the use of extensive flow conditioning devices upstream of the contraction. Overall, this wind tunnel facility provides experimental testing conditions that are comparable to other state-of-the-art low-speed wind tunnel facilities.

3 HYDRODYNAMICS OF THE EXHAUST DUCT OF A HYDROKINETIC TURBINE

3.1 INTRODUCTION TO HYDROKINETIC TURBINES

As the demand on the world's power grids increases, the energy available from river and tidal currents continues to be explored as a way to satisfy the public's demand for renewable energy. The traditional method of extracting energy from a mass of water is through the construction of a hydroelectric dam, which has very high infrastructure costs, a lengthy construction period, and a significant impact on local ecosystems. Modern turbine designs are therefore starting to focus on low-head and free-stream (hydrokinetic) configurations that extract energy from water currents without significantly affecting the local ecosystem.

A hydrokinetic turbine design developed at Carleton University is expected to substantially increase the power output of a turbine in a river or tidal current setting compared to existing alternatives. The remainder of this thesis focuses on evaluating the pressure-recovery performance of the exhaust duct of the Carleton Hydrokinetic Turbine and determining its sensitivity to certain geometric parameters.

3.2 CARLETON HYDROKINETIC TURBINE

The Carleton Hydrokinetic Turbine is a patented design for generating electrical power from water currents (Patent CA 2544108 in the Canadian Patents Database and

Patent 736766 in the U.S. Patent Application Database). The design includes a housing containing a pair of exhaust ducts in the shape of wide-angle conical diffusers, a pair of turbine assemblies and a pair of generator assemblies. Each exhaust duct has an axial intake and an axial discharge, as well as a side intake that extends along the length of the exhaust duct and faces upstream, as shown in Figure 3.1. The purpose of shaping each exhaust duct into a wide-angle conical diffuser is to use the pressure recovery through the diffuser to increase the mass flow rate through the turbine rotor. The purpose of the side intake is to direct a portion of the flow up against the interior surface of the exhaust duct, as shown in Figure 3.2, to control the boundary layer and prevent it from separating in the presence of substantial diffusion. The velocity magnitude and direction of the flow entering the side intake are determined primarily by the velocity of the currents at the installation site and the inclination angle (α) of the Carleton Hydrokinetic Turbine relative to the local currents, as shown in Figure 3.3. This figure also shows the location of the tether line that connects the Carleton Hydrokinetic Turbine to its fixed base. The value of α is dictated by the weight, buoyancy force and hydrodynamic loads acting on the Carleton Hydrokinetic Turbine. The idea of using the prevailing water currents that do not pass through the turbine rotor to enhance the pressure recovery downstream is the primary distinguishing feature of the Carleton Hydrokinetic Turbine. (Yaras & Golriz, 2006).

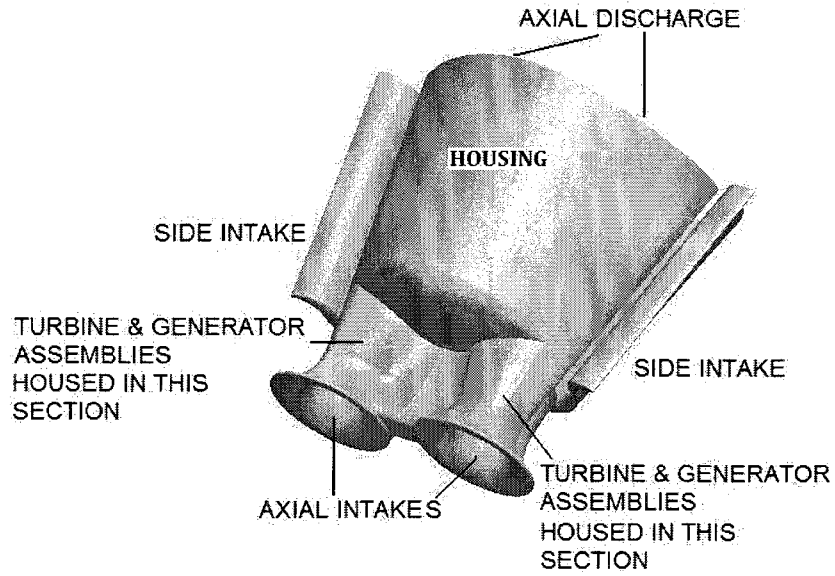


Figure 3.1 Carleton Hydrokinetic Turbine Components

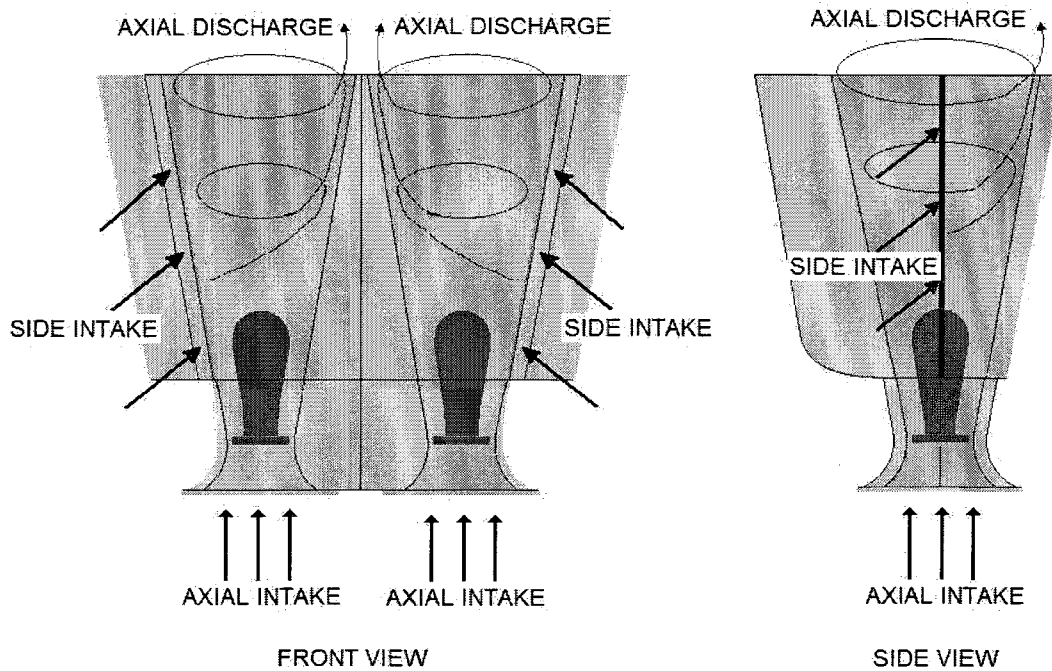


Figure 3.2 Schematic of Flow through Carleton Hydrokinetic Turbine

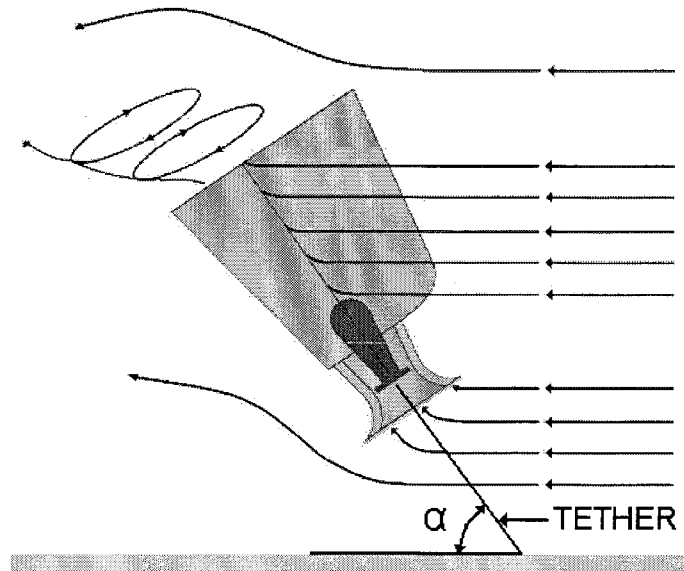


Figure 3.3 Orientation of Carleton Hydrokinetic Turbine Relative to Local Currents

3.2.1 Internal Geometry of the Carleton Hydrokinetic Turbine Exhaust Duct

On the Carleton Hydrokinetic Turbine, the exhaust duct downstream of each of the turbine and generator assemblies is designed to create a high rate of static pressure recovery in a relatively short streamwise distance. The flow entering the exhaust duct through the axial intake is a combination of flow through the turbine rotor and flow through an annular bypass around the turbine rotor, as shown in Figure 3.4. The generator assembly partially blocks the axial intake, creating an annular opening for the fluid.

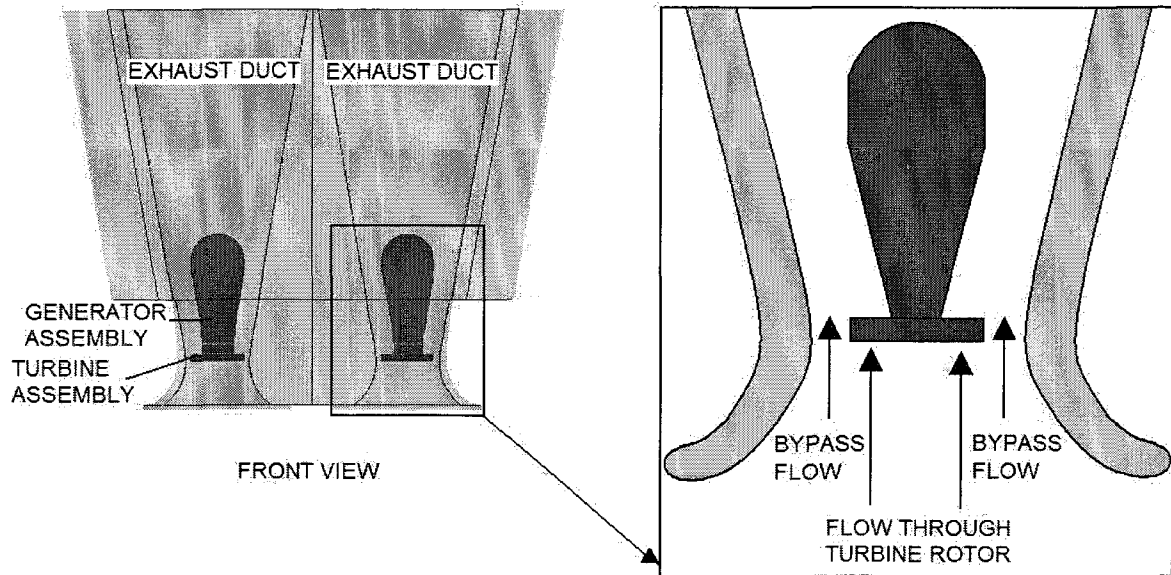


Figure 3.4 Internal Geometry of Carleton Hydrokinetic Turbine Exhaust Duct

Computational fluid dynamics (CFD) is the most cost-effective way to analyze the pressure-recovery performance of the exhaust duct for a range of geometries, operating conditions and inclination angles. Based on the favourable experience of using ANSYS CFX CFD software to design the wind tunnel contraction in the previous chapter of this thesis, the same software is used to evaluate the pressure-recovery performance of the exhaust duct of the Carleton Hydrokinetic Turbine.

In addition to a significant pressure gradient in the exhaust duct, there is also relatively high streamline curvature that poses a challenge for the typical turbulence models of a Reynolds-Averaged Navier-Stokes (RANS) solution. Therefore, the present chapter includes an evaluation of the available turbulence models suitable for modeling flows with both streamwise pressure gradients and streamline curvature, before presenting the study of the pressure-recovery performance of the exhaust duct.

3.3 REVIEW OF FLOWS THROUGH CONICAL DIFFUSERS

The exhaust duct of the Carleton Hydrokinetic Turbine is formed in the shape of a wide-angle conical diffuser in order to maximize the pressure recovery through the duct. A wide-angle diffuser is one where boundary-layer control methods are required to prevent separation due to the rapid streamwise increase in cross-sectional area (Bradshaw & Mehta, 2003). In the absence of a boundary-layer control method, separation can typically be expected in diffusers with opening angles (2θ) greater than 10 deg. (Sparrow et al., 2009).

In the exhaust duct of the Carleton Hydrokinetic Turbine, the boundary layer is controlled through the vortex generated by the flow from the side intake. A study by Senno and Nishi (1974) found that vortex generators are capable of preventing flow separation in conical diffusers with opening angles up to 16 deg. Their experiment tested diffusers with opening angles ranging from 8 deg. to 30 deg., with the vortex generated by small blades at the diffuser inlet. A more recent experiment by Clausen et al. (1993) on flow through a conical diffuser with an opening angle of 20 deg. also used a vortex generated at the diffuser inlet to control the boundary-layer development. The vortex approximated solid-body rotation, and was shown to prevent both boundary-layer separation and recirculation in the diffuser core. In the exhaust duct of the Carleton Hydrokinetic Turbine, the vortex is generated by the tangential component of the flow from the side intake; not at the axial inlet of the diffuser as in the previous examples. Therefore, while the papers by Senno and Nishi (1974) and Clausen et al. (1993) provide useful guidelines on vortex generation as a boundary-layer control method in diffusers, in

the present instance their results cannot be directly applied to the development of the exhaust duct of the Carleton Hydrokinetic Turbine.

The electricity generator assembly at the axial intake of the exhaust duct of the Carleton Hydrokinetic Turbine is a bluff body that affects the surrounding and downstream flow in the exhaust duct. A paper by Mahalakshmi et al. (2007) documents the effects of streamlined and bluff bodies at the inlet of a diffuser on the downstream flow for diffuser opening angles of 10 deg. and 14 deg. The experiment results indicate that the flow accelerated through the annular region between the bluff body and the diffuser walls and separated off the downstream end of the bluff body. The flow separation caused by the bluff body produced a large downstream wake that reduced the mean centerline velocity in the diffuser for a distance of 5.26 inlet diameters downstream. Based on these results, it is expected that the geometry of the generator housing will cause flow separation and a velocity deficit along the centerline of the exhaust duct of the Carleton Hydrokinetic Turbine. This velocity deficit could cause recirculation in the core of the diffuser, reducing the pressure-recovery performance of the exhaust duct.

3.4 TURBULENCE MODEL SELECTION

The choice of turbulence model for the evaluation of the pressure-recovery performance of the exhaust duct was limited to the models available with the ANSYS CFX CFD software. Although this software offers an extensive list of turbulence closure models, a number of the available turbulence models were not considered for this study based on published information about their performance. The popular k - ϵ and k - ω

turbulence models discussed in Section 2.8.3.2 are ill-suited to model the flow through the exhaust duct. The k - ϵ model is unable to accurately predict flow separation in adverse pressure gradients and is inaccurate in regions of highly anisotropic swirling flow (Gyllenram & Nilsson, 2004), and the k - ω model is highly sensitive to the free-stream turbulence conditions (Bardina, Coakley, & Huang, 1997).

The ANSYS CFX CFD software includes two methods for modeling the boundary layer near a wall. The first method is called the ‘automatic’ option. This is a hybrid method that automatically switches from a low-Reynolds-number formulation to wall functions based on the grid-node spacing, allowing for optimum near-wall treatment over a wide range of grid-node spacing. For a strict low-Reynolds-number implementation, the distance of the first grid-node perpendicular to the wall must satisfy the condition of $y^+ < 2$ and there must be at least 15 grid-nodes across the local thickness of the boundary layer (ANSYS, 2009). The second method to model the boundary layer uses wall functions exclusively. The use of wall functions to model the boundary layer significantly reduces the grid-node resolution requirements by taking advantage of the similar nature of the wall-region of many turbulent boundary layers (Patel, 1984). The main disadvantage with wall functions is that they are not accurate in regions with high pressure gradients or in separated flows (Patel, 1984). A low-Reynolds-number implementation is capable of modeling flows with high pressure gradients, but requires a higher number of grid-nodes that significantly increase the computational expense. For example, in the numerical study by Gyllenram and Nilsson (2004) on swirling flow through a conical diffuser, the grid-node count increased from 100,000 to 781,250 when

modeling the boundary layer using a low-Reynolds-number implementation instead of wall functions.

The SST turbulence model described in detail in Section 2.8.3.2 was used successfully to design the wind tunnel contraction in the previous chapter of this thesis, and was selected as a candidate to model the flow through the exhaust duct due to its ability to predict boundary-layer separation in adverse pressure gradients. The study by Sparrow et al. (2009) on flow through a conical diffuser over a range of Reynolds numbers and opening angles used the SST turbulence model successfully to predict flow separation. The SST turbulence model in ANSYS CFX treats the flow near the wall using the 'automatic' option. Therefore, the boundary layer can be calculated using a low-Reynolds-number formulation with the SST turbulence model, provided there is sufficiently fine wall-normal grid-node spacing.

Another turbulence model available in CFX that may be suitable for modeling the flow through the exhaust duct of the Carleton Hydrokinetic Turbine is the re-normalized group (RNG) k - ϵ turbulence model developed by Yakhot and Orszag (1992). The basic idea of RNG turbulence modeling is to systematically remove the smallest scales of turbulence to a point where the remaining scales are resolvable with the available computing capacity (Yakhot, 1992). Compared to the standard k - ϵ turbulence model, the RNG k - ϵ turbulence model calculates the model constants explicitly and contains additional terms and functions in the transport equations (Jawarneh, 2007). The RNG k - ϵ turbulence model has been suggested to offer improved accuracy over the standard k - ϵ turbulence model for flows with significant streamline curvature. A study by Jawarneh

(2007) of a two-phase, strongly swirling flow in a cylindrical separator found good agreement between the results of a simulation using the RNG k- ϵ turbulence model and the experiment data. Their paper suggests that simulations of swirling flow using the RNG k- ϵ turbulence model have improved accuracy because the effect of swirl on turbulence is calculated (Jawarneh, 2007). A study by Gupta and Kumar (2007) investigated three-dimensional flow in a cyclone and compared numerical simulations using the standard k- ϵ and the RNG k- ϵ turbulence models to experiment data. The results from this study indicate that the RNG k- ϵ turbulence model offers improved accuracy over the standard k- ϵ model in the presence of swirling flows. For the RNG k- ϵ turbulence model in CFX, the flow near the wall is modeled using wall functions.

Based on the available information, the SST and RNG k- ϵ turbulence models were selected as candidates to model the flow through the exhaust duct of the Carleton Hydrokinetic Turbine. The final decision about which turbulence model to use was made by testing both turbulence models against experimental data of a flow with streamwise adverse pressure gradients and streamline curvature.

3.5 TURBULENCE MODEL VALIDATION

3.5.1 Experimental Parameters

The benchmark test case selected to evaluate the abilities of the SST and RNG k- ϵ turbulence models is the experimental work of Clausen et al. (1993) on a conical diffuser with swirling inflow. In the experiment, air passes through a conical diffuser with an opening angle (2θ) of 20 deg. and a diffuser area ratio (ratio of outlet area to inlet area) of

2.84. The swirl at the intake of the diffuser approximates solid body rotation and was selected to avoid both boundary-layer separation along the walls and recirculation in the diffuser core. The axial velocity at the intake (U_{REF}) is 11.6 m/s and the swirl number (ratio of maximum tangential velocity to reference axial velocity) is 0.59. The velocity field in the diffuser was measured using a single hotwire probe, and the Reynolds stresses in the boundary layer were measured using a rotatable X-hotwire probe. The published data includes near- and far-wall axial and tangential velocity profiles and near-wall turbulence kinetic energy profiles. The experiment setup is shown in Figure 3.5.

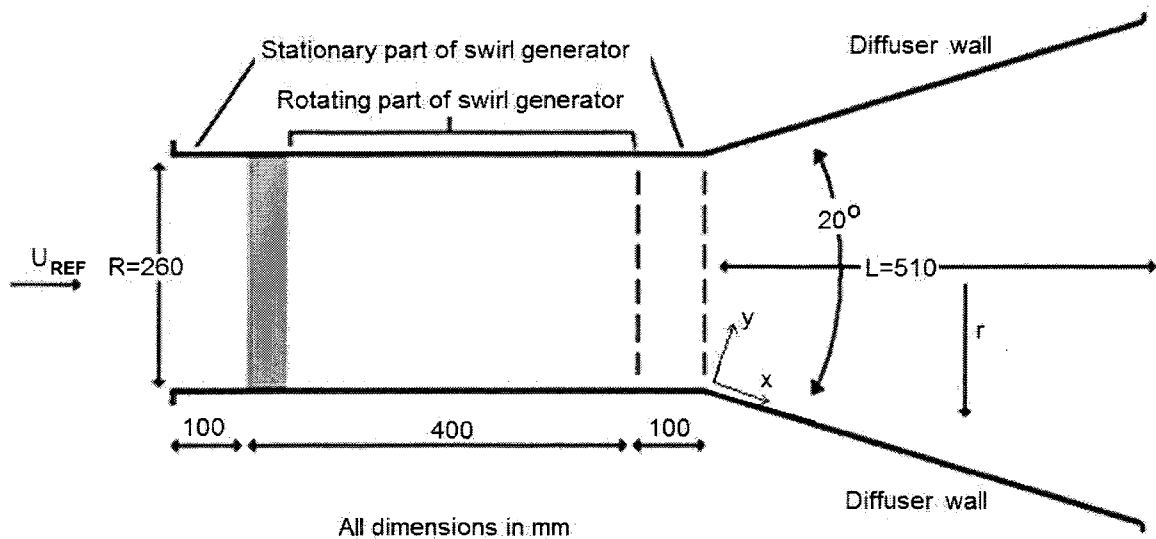


Figure 3.5 Experiment Setup for Turbulence Model Validation Study
(Modified from Clausen et al., 1993)

3.5.2 Computational Domain

The computational domain for the turbulence model validation study is shown in Figure 3.6. The inlet boundary of the domain is located 25 mm upstream of the diffuser. This is the most upstream streamwise location where experiment is data available to use

as the boundary condition for the inlet boundary of the computational domain. The outlet boundary includes part of the downstream region into which the diffuser flow discharges in order to prevent the selected boundary conditions from artificially influencing the diffuser flow field. The effect of placing the outlet boundary in the downstream region instead of at the exit plane of the diffuser is investigated as part of the turbulence model validation study.

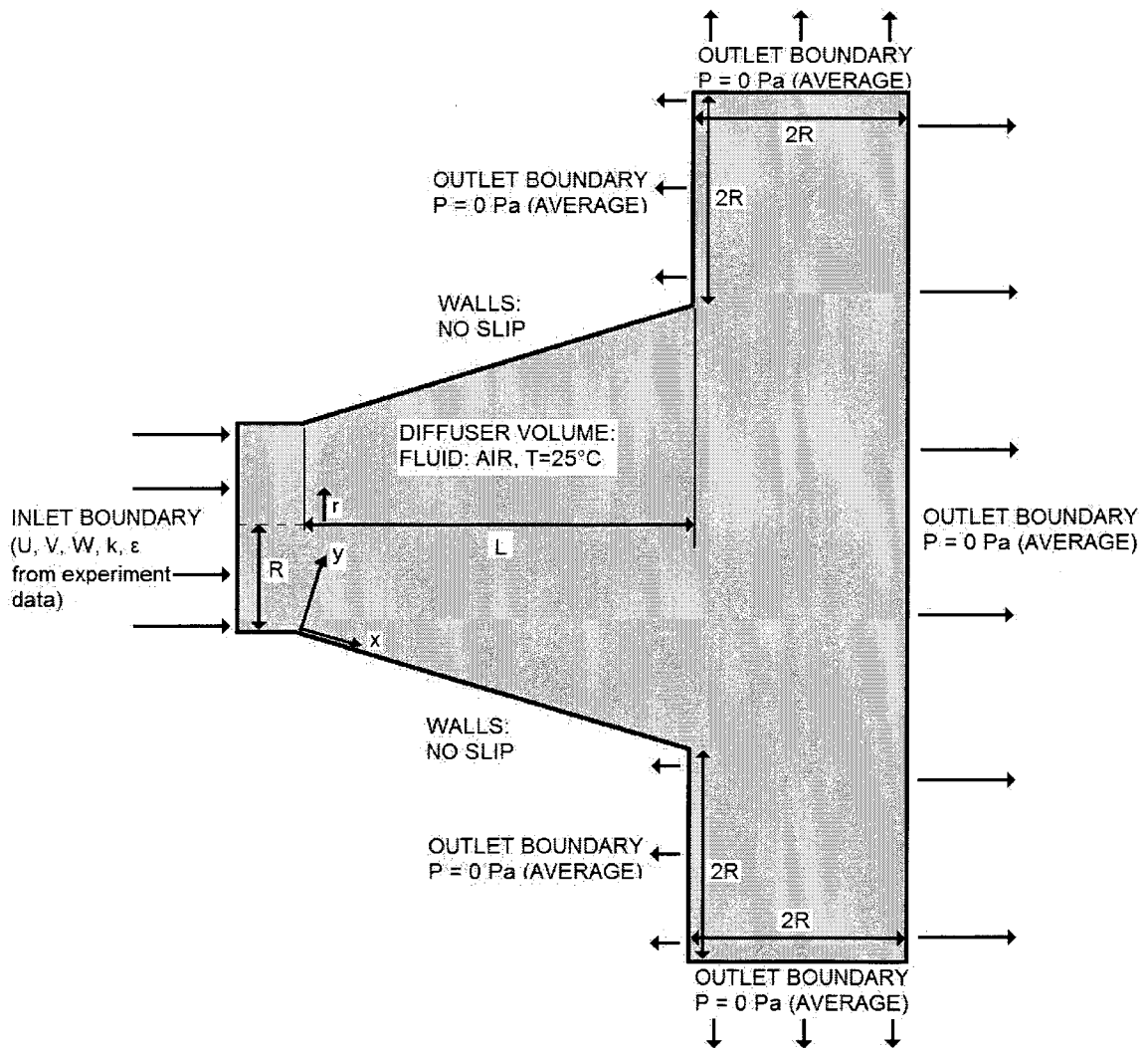


Figure 3.6 Computational Domain for Turbulence Model Validation Study

3.5.3 Boundary Conditions

3.5.3.1 Inlet Boundary Conditions

The inlet boundary of the computational domain requires the specification of the axial and tangential velocities and the turbulence parameters k and ε . The magnitudes of the axial and tangential velocity components were obtained directly from experimental data. The definitions for k and ε are shown below for a three-dimensional flow, where u is the fluctuating component of velocity, ν is the kinematic viscosity of the fluid, x is the spatial distance, and the subscripts ' i ' and ' j ' refer to a Cartesian direction in three-dimensional space.

$$k = \frac{1}{2} \sum_{i=1}^3 (u_i)^2 \quad (3.1)$$

$$\varepsilon = \frac{\nu}{2} \sum_{i,j=1}^3 \left(\frac{\partial u_i}{\partial x_j} + \frac{\partial u_j}{\partial x_i} \right)^2 \quad (3.2)$$

The value of k was calculated from the components of the Reynolds stresses measured by Clausen et al. (1993). The equation for ε includes the spatial gradients of the velocity fluctuations, which are difficult to obtain from experimental data since they require the simultaneous measurement of velocity fluctuations at multiple closely-spaced locations. Therefore, the semi-empirical equation given below was used to calculate ε at the inlet boundary of the domain, where D is the hydraulic diameter of the diffuser inlet. The constant appearing the denominator of this expression is based on an integral length

scale of turbulence (L) that is taken to be 7% of the hydraulic diameter and a constant C_μ of 0.09.

$$\varepsilon = \frac{C_\mu^{3/4} k^{3/2}}{L} = \frac{k^{3/2}}{0.426 D} \quad (3.3)$$

It is important to impose the correct integral length scale of turbulence at the inlet boundary to obtain the correct decay of k and U in the core region of the duct flow. A lower turbulence length scale will increase the streamwise rate of decay of k and U along the centerline of the diffuser (Cho & Fletcher, 1991). The sensitivity of the simulation results to the chosen turbulence length scale at the inlet boundary is examined as part of the turbulence model validation study.

3.5.3.2 Wall Boundary Conditions

The walls of the diffuser were defined as no-slip, smooth surfaces to simulate the surfaces used in the experiment.

3.5.3.3 Outlet Boundary Conditions

At the outlet boundary of the domain, the average static pressure was specified and the first derivatives of the flow variables in the direction perpendicular to the boundary plane were set to zero (Neumann boundary condition). Other computational studies of flows through diffusers, such as those by Prodal (1993), Martin (2004) and Sparrow (2009), also specify the average outlet pressure and apply Neumann boundary-conditions at the outlet boundaries of their domains.

3.5.4 Type of Spatial Grid

Regardless of whether a grid is structured or unstructured in appearance, the ANSYS CFX program calculates the flow properties at each grid-node using an unstructured solver. Therefore, there is no computational advantage to using hexahedral elements (structured appearance) over tetrahedral elements (unstructured appearance). Due to the complex geometry of the exhaust duct of the Carleton Hydrokinetic Turbine, a grid with tetrahedral elements was selected to discretize the volume of the exhaust duct. A tetrahedral element shape allows for computationally efficient local refinement of the spatial grid. Based on this selection, tetrahedral elements were also used to define the diffuser grid for the turbulence validation study to ensure consistency with the simulations of the flow through the exhaust duct of the Carleton Hydrokinetic Turbine.

3.5.5 Discretization of Spatial Derivatives

In ANSYS CFX, the spatial derivatives in the Navier-Stokes equations are approximated using series expansions. The accuracy of the approximation of a continuous function using a series is based on the exponent of the grid-node spacing or time-step factor of the largest term in the truncated part of the series expansion. The ANSYS CFX program uses 2nd-order accurate approximations to solve the equations of motion of the flow unless otherwise specified by the user (ANSYS, 2009).

The numerical scheme used by ANSYS CFX to approximate the advection terms of the Navier-Stokes equations is shown in Equation 3.4, where Φ_{up} is the value of a

variable at the upwind node, Φ_{ip} is the value of the variable at the integration point, β is the blending factor, and \vec{r} is the vector from the upwind node to the integration point.

$$\Phi_{ip} = \Phi_{up} + \beta \cdot \nabla\Phi \cdot \vec{r} \quad (3.4)$$

There are three different options for solving the advection term in CFX: upwind differencing, specified blend factor, and high resolution. The upwind differencing scheme is 1st-order accurate and sets $\beta = 0$. This solution is robust but tends to introduce excessive discretization errors that smear steep spatial gradients. The specified blend factor scheme allows the user to specify the value of β between 0 and 1. The choice of $\beta = 1$ is 2nd-order accurate in space and is better able to reproduce steep spatial gradients, but tends to cause non-physical oscillations in the solution. The high resolution scheme uses a special non-linear formulation to compute β as close to 1 as possible at each grid-node. This scheme calculates a minimum and maximum value for each variable at a node based on the values of the adjacent nodes, and then ensures that the solution falls within those bounds. The high resolution scheme only reduces to 1st-order solutions near discontinuities. For the present turbulence validation study and the study of the flow through the exhaust duct of the Carleton Hydrokinetic Turbine, the specified blend scheme was used with $\beta = 1$ to obtain a 2nd-order accurate solution. (ANSYS, 2009)

The numerical scheme used by ANSYS CFX to solve the diffusion term of the Navier-Stokes equations is shown in Equation 3.5, where the left-hand side of the equation is the spatial derivative of the diffusion term at the integration point, N_n is the

shape function at each grid-node, and Φ_n is the value of a variable at each grid-node. (ANSYS, 2009)

$$\left[\frac{\partial\Phi}{\partial x}\right]_{ip} = \sum_n \left[\frac{\partial N_n}{\partial x}\right]_{ip} \Phi_n \quad (3.5)$$

Finite-element shape functions are used by ANSYS CFX to describe how a variable varies within an element, and are defined by the shape of the element. For a single tetrahedral element there are four grid-nodes, therefore the summation on the right-hand side of Equation 3.5 is over four points ($n = 4$). The solution for the diffusion term of the Navier-Stokes equations is 2nd-order accurate. (ANSYS, 2009)

3.5.6 Solution Algorithm and Convergence Study

For steady-state simulation of flows, the CFX solver automatically applies a false time step as a means of under-relaxation as the equations iterate towards a converged solution. If the time scale is too large the convergence may be oscillatory, but if the time scale is too small the convergence will be slow. A typical solution requires between 50 and 100 iterations to achieve convergence (ANSYS, 2009), and the majority of the simulations for the turbulence model validation study converged within 80 to 100 iterations.

For the turbulence model validation study, the root-mean square (RMS) residual convergence criteria for the continuity, momentum and turbulence partial-differential equations were set to 10^{-5} . To ensure that the ANSYS CFX solutions for the turbulence

model validation study are independent of the selected RMS convergence criteria, simulations were also completed with the RMS convergence criteria set to 10^{-6} . The simulation results indicate that lowering the RMS convergence criteria by an order of magnitude causes negligible differences in the velocity and turbulence profiles of the flow through the diffuser. The RMS convergence criteria for the turbulence model validation study are comparable to other numerical studies, such as the study by Sparrow et al. (2009) that sets the RMS convergence criteria to 10^{-6} .

3.5.7 Grid Convergence Study

The effect of grid-node spacing on the simulations of the flow through the diffuser was examined to ensure the solution is grid-independent. To establish a grid-independent solution using Richardson extrapolation, the grid-node spacing in each spatial direction should be refined by a factor of two (Roach, 1994). Applying this procedure to a three-dimensional domain, the grid-node count will increase by a factor of eight for each level of grid refinement; this is not feasible with the available computational resources. Instead of a Richardson extrapolation, selective grid refinement was used in the core volume of the diffuser and in the boundary-layer region. The grid-convergence of the solution was assessed by evaluating the change in the predicted velocity and turbulence kinetic energy profiles along the length of the diffuser for each level of grid refinement. A change in the peak axial velocity, tangential velocity, and turbulence kinetic energy of less than 1% in a given plane when the grid-node count was doubled or the height of the first grid-node perpendicular to the wall was halved was considered to provide a grid-independent solution. The total grid-node count for the grid-

independent solution of the flow through the diffuser is 1×10^6 . An image of the grid for the turbulence model validation study is shown in Figure 3.7.

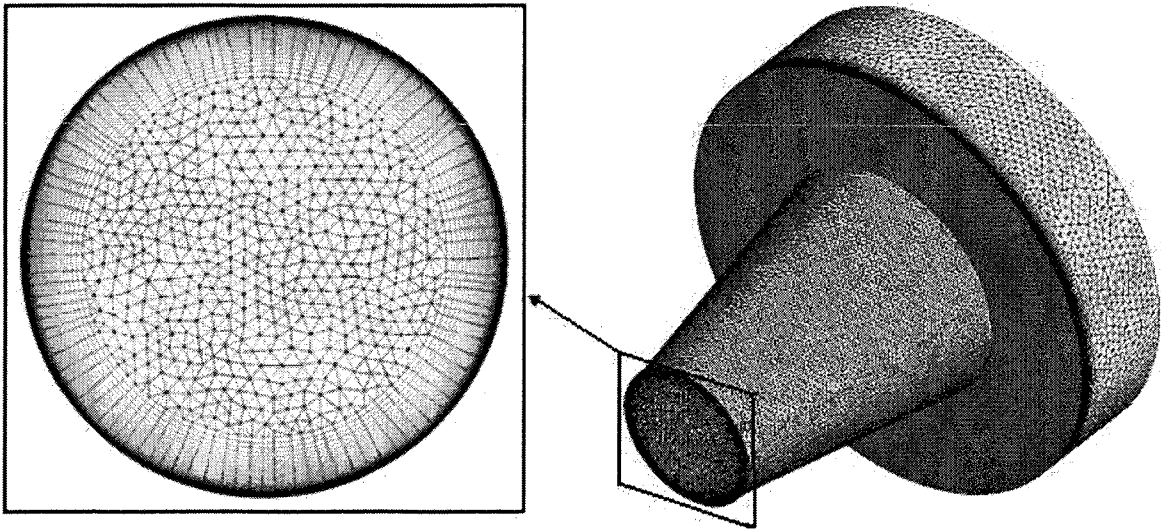


Figure 3.7 Computational Grid for Turbulence Model Validation Study

Experimental data from Clausen et al. (1993) indicates that the boundary-layer thickness varies from 15 mm at the inlet to 30 mm at the outlet of the diffuser. The distance of the first grid-node in the wall-normal direction was based on the requirement that $y^+ < 2$ for a low-Reynolds-number implementation of the SST turbulence model. Preliminary simulations indicate that setting the distance of the first grid-node in the wall-normal direction equal to 0.05 mm results in y^+ values between 1 and 1.5 along the walls of the diffuser. The expansion ratio of the grid-nodes in the wall-normal direction was set to 1.15 and a total of 45 inflation layers were required to reach a thickness that is comparable to the boundary layer thickness of 30 mm at the outlet plane of the diffuser (refer to Section 2.8.3.4 for information on the use of inflation layers in ANSYS CFX).

3.5.8 Simulation Results for the Turbulence Model Validation Study

Using the grid-node spacing that was determined in the previous section to provide a grid-independent solution, the flow through the diffuser was simulated using the SST and RNG k- ϵ turbulence models. The solution computed using the SST turbulence model is compared to the experiment data in Figure 3.8 to Figure 3.11. The profiles in each measurement plane along the length of the diffuser are offset by five times the value of x/L for clarity, where x is the streamwise location of the measurement plane.

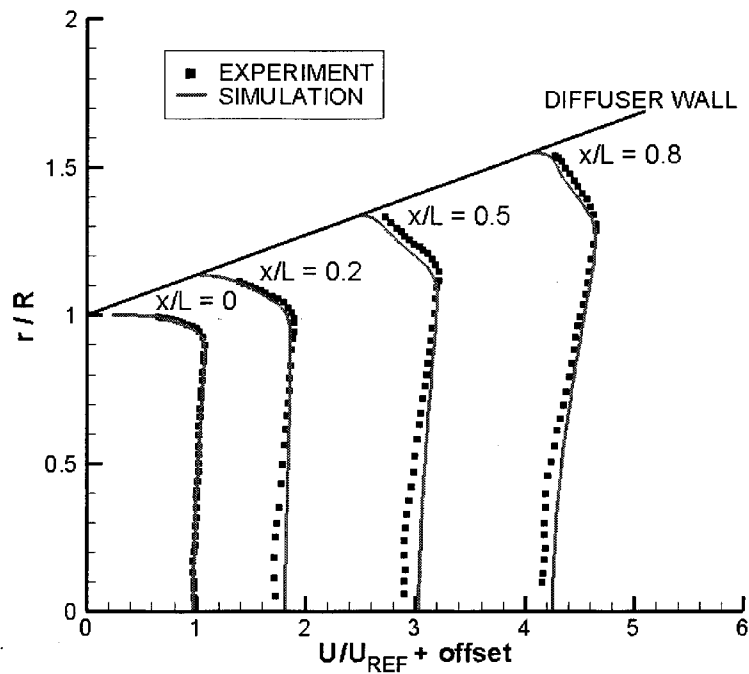


Figure 3.8 Axial Velocity (U/U_{REF}) Results with SST Model

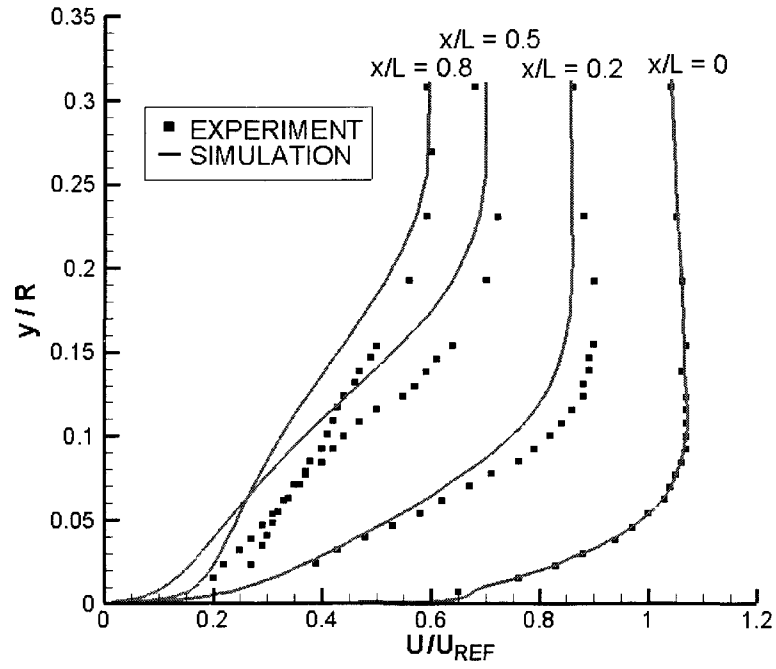


Figure 3.9 Near-Wall Axial Velocity (U/U_{REF}) Results with SST Model

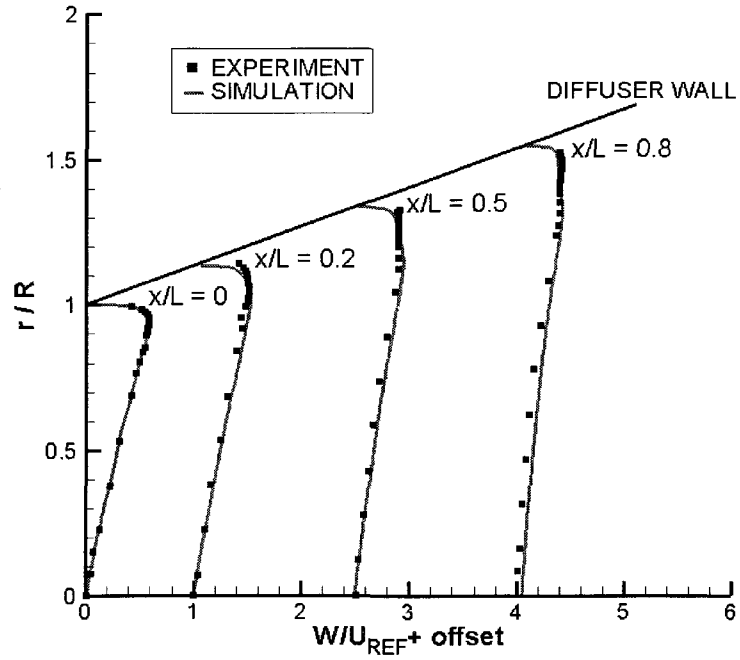


Figure 3.10 Tangential Velocity (W/U_{REF}) Results with SST Model

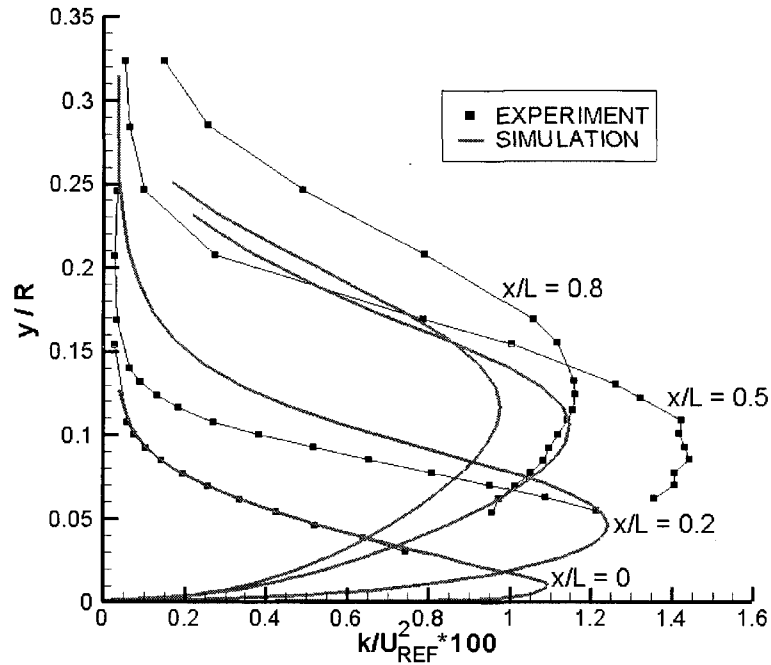


Figure 3.11 Turbulence Kinetic Energy ($k/(U_{REF}^2)*100$) Results with SST Model

Overall, the flow simulations using the SST turbulence model agree reasonably well with the experiment data. For example, at $x/L = 0.8$ the simulations predict the maximum axial velocity within 0.43% and the maximum tangential velocity within 1.3% of the experiment data. Figure 3.8 and Figure 3.9 show that the simulations tend to under-predict the axial velocity near the wall and over-predict it towards the center of the diffuser. Figure 3.10 shows that the computed tangential velocity component matches the experimental data well over the entire length and radius of the diffuser. The simulation results under-predict the peak turbulence kinetic energy by up to 20% at $x/L = 0.8$, as shown in Figure 3.11. The prediction accuracy of the turbulence kinetic energy for the swirling diffuser flow of Clausen et al. (1993) is similar to the prediction accuracy of non-swirling diffuser flows shown in studies by Cho and Fletcher (1991) and Grosvenor (2000) for the SST turbulence model. This may suggest that the finite streamline

curvature in this study does not significantly contribute to the accuracy of the turbulence kinetic energy calculated using the SST turbulence model.

The solution computed using the RNG $k-\epsilon$ turbulence model is compared to the experiment data in Figure 3.12 through Figure 3.15. The profiles in each measurement plane along the length of the diffuser are offset by five times the value of x/L for clarity, where x is the streamwise location of the measurement plane.

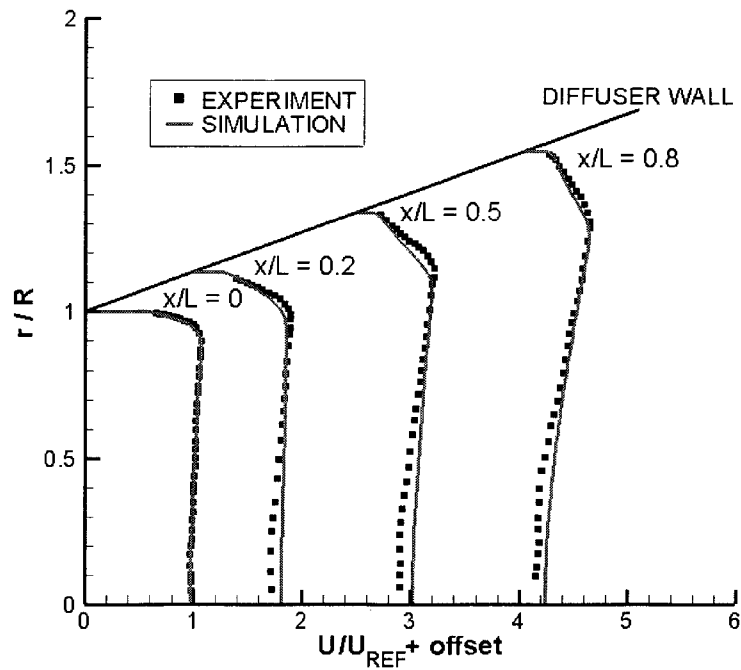


Figure 3.12 Axial Velocity (U/U_{REF}) Results with RNG $k-\epsilon$ Model

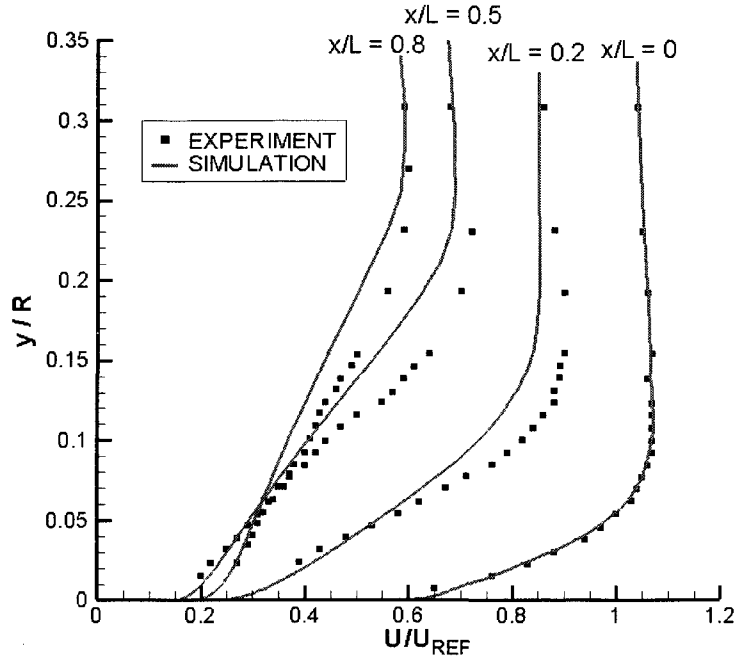


Figure 3.13 Near-Wall Axial Velocity (U/U_{REF}) Results with RNG k- ϵ Model

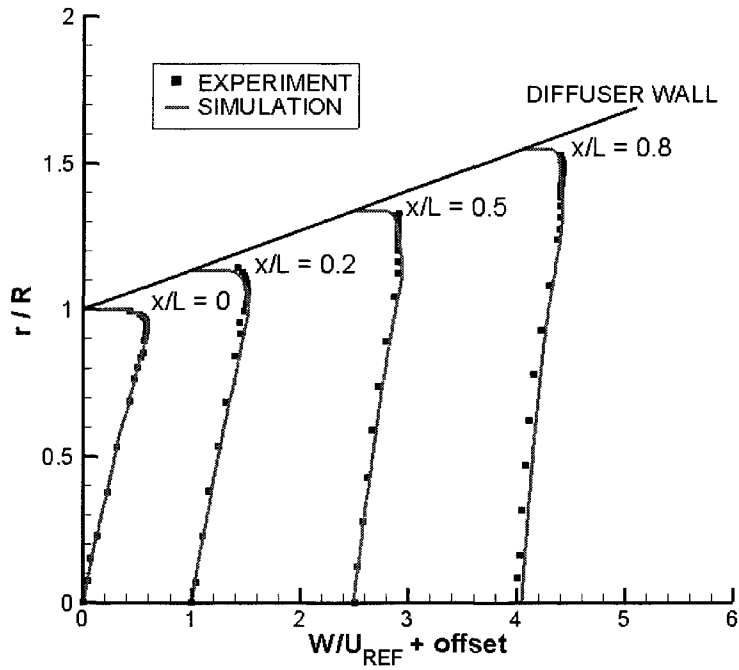


Figure 3.14 Tangential Velocity (W/U_{REF}) Results with RNG k- ϵ Model

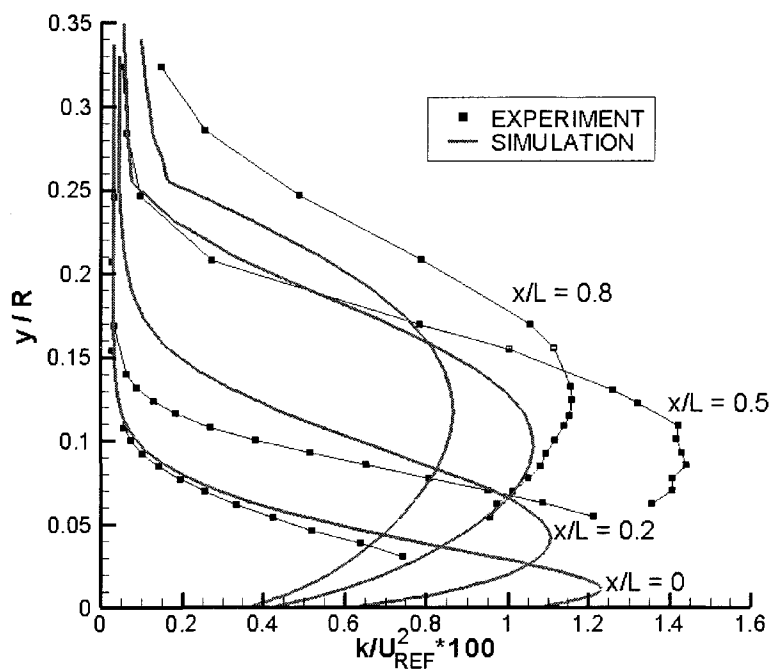


Figure 3.15 Turbulence Kinetic Energy ($k/(U_{REF}^2)*100$) Results with RNG k- ϵ Model

The flow simulations using the RNG k- ϵ turbulence model also agree reasonably well with the experiment data. For example, at $x/L = 0.8$ the simulations predict the maximum axial velocity within 1.7% and the maximum tangential velocity within 2.5% of the experiment data. The differences between the simulation results and the experiment data are of the same order of magnitude as the results calculated with the SST turbulence model. Figure 3.12 and Figure 3.13 demonstrate that the simulations again tend to under-predict the axial velocity near the wall and over-predict it towards the center of the diffuser. Figure 3.14 shows that the tangential velocity component matches well with the experiment data over the length and radius of the diffuser. The simulation results using the RNG k- ϵ turbulence model under-predict the peak turbulence kinetic energy by up to 26% at $x/L = 0.8$, as shown in Figure 3.15. This prediction accuracy is of the same order of magnitude as the accuracy of the results calculated using the SST

turbulence model, indicating that the explicit calculation of the effect of streamline curvature on turbulence does not improve the prediction of turbulence kinetic energy in the present instance.

The computer simulations of the benchmark validation case of Clausen et al. (1993) indicate that both the SST and RNG k- ϵ turbulence models are equally capable of accurately predicting the flow field in a diffuser with a strong adverse pressure gradient and notable streamline curvature. Therefore, either turbulence model could be used to evaluate the pressure-recovery performance of the Carleton Hydrokinetic Turbine exhaust duct. Given that the flow from the side intake of the exhaust duct has a significant impact on the wall boundary-layer development, the SST turbulence model was chosen over the RNG k- ϵ model to take advantage of the low-Reynolds-number wall treatment in ANSYS CFX.

As part of the turbulence model validation study, the sensitivity of the results to the integral length scale of turbulence used to define ϵ was examined. For the preliminary simulations, the integral length scale of turbulence was set to 7% of the hydraulic diameter of the diffuser inlet. Setting the integral length scale to 3.5% and 10.5% of the hydraulic diameter yielded negligible changes in the axial velocity, tangential velocity and turbulence kinetic energy profiles of the flow through the diffuser. These results indicate that the solution for the flow through the diffuser using the SST turbulence model is relatively insensitive to the turbulence conditions at the diffuser inlet.

The effect of the location of the outlet boundary of the computational domain on the flow through the diffuser was examined by relocating the outlet boundary of the computation domain to the exit plane of the diffuser. Relocating the outlet boundary of the domain changed the axial velocity, tangential velocity and turbulence kinetic energy values at $x/L = 0.8$ by less than 1%. These results indicate that the location of the outlet boundary of the computational domain has negligible effect on the flow through the diffuser.

3.6 EVALUATION OF THE CARLETON HYDROKINETIC TURBINE EXHAUST DUCT

The exhaust duct of the Carleton Hydrokinetic Turbine is designed to create a high rate of static pressure recovery in a relatively short streamwise distance, using tangential flow from the side intake to control the boundary-layer development. The goal of this study is to select an exhaust duct geometry that improves the pressure-recovery performance of the exhaust duct over a range of inclination angles, and to establish the sensitivity of the pressure recovery to changes in the exhaust duct geometry. This effort provides the groundwork for a future study aimed at identifying an optimum exhaust duct geometry for the Carleton Hydrokinetic Turbine.

3.6.1 Computational Domain

The computation domain used to simulate the flow through the exhaust duct of the Carleton Hydrokinetic Turbine is shown in Figure 3.16. The upstream end of the domain includes the generator assembly and extends to, but does not include, the turbine

assembly. The generator assembly was included in the domain because it is expected to have a significant impact on the flow through the exhaust duct. The axial intake boundary is divided into two regions: one representing the flow discharging from the turbine rotor and one representing the bypass flow around the turbine. The side intake boundary is located at the throat of the contoured side intake of the Carleton Hydrokinetic Turbine. Modeling the flow over the contoured region would require extending the computational domain far upstream where the local currents are undisturbed by the presence of the Carleton Hydrokinetic Turbine, and would significantly increase the computational expense of each simulation. The outlet boundary of the computational domain is located at the axial discharge plane of the exhaust duct. This location was selected based on the results of the turbulence model validation study, which indicated that the location of the outlet boundary of the computational domain has negligible impact on the velocity and turbulence profiles of the flow upstream in a diffuser.

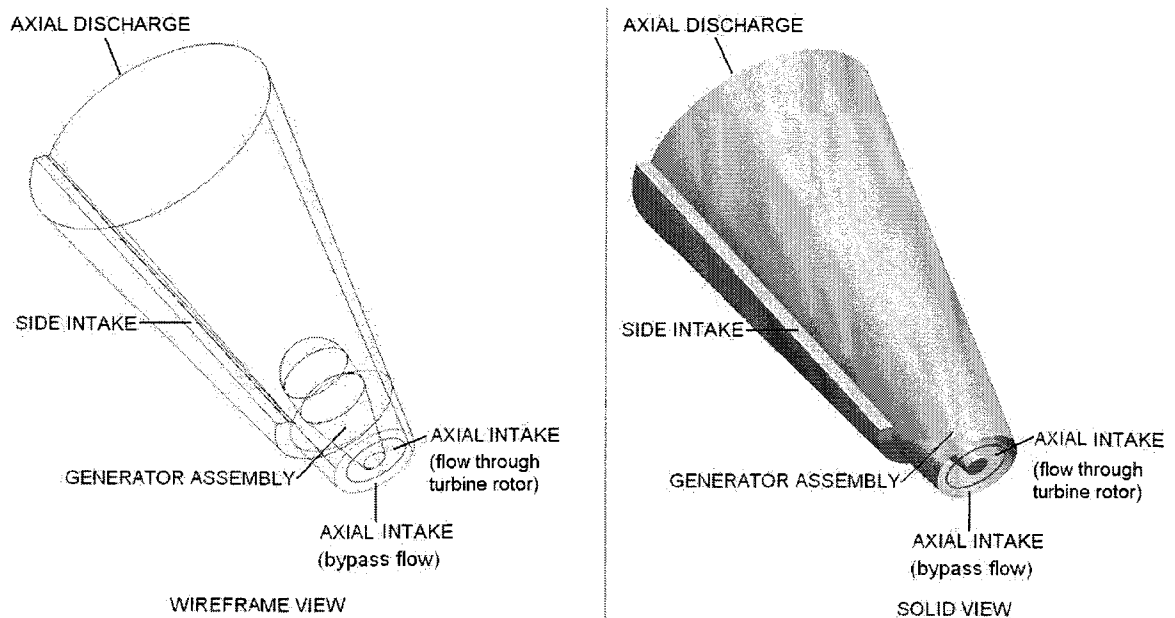


Figure 3.16 Computational Domain for Exhaust Duct Flow Simulations

The shell of the Carleton Hydrokinetic Turbine is intended to fit over any commercially available turbine assembly, with the diameter of the turbine rotor dictating the size of the housing structure. Since turbine assemblies vary in size depending on the manufacturer's design and the desired shaft power, the diameter of the turbine rotor was selected as the scaling factor for the geometry of the exhaust duct in the present study. Therefore, the width of the side intake (w), the diameter of the axial intake (D_{IN}), and the length of the exhaust duct (L) are all scaled relative to the diameter of the turbine rotor (D_{REF}), shown in Figure 3.17.

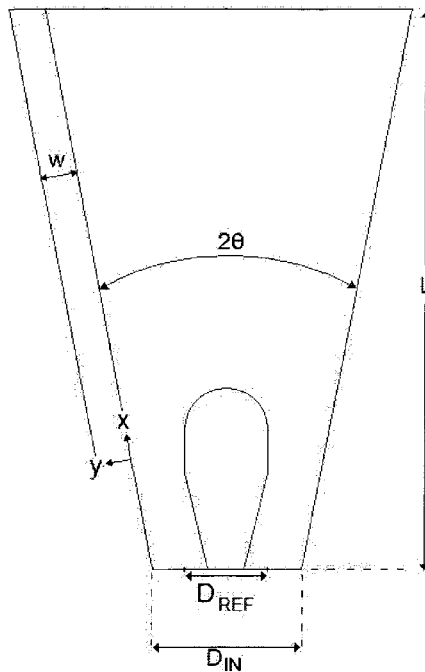


Figure 3.17 Geometric Parameters for Evaluation of Exhaust Duct Performance

Based on geometric specifications of various bulb-turbine and generator assemblies currently in production, a generator housing length of $2.25 D_{REF}$ and maximum diameter equal to D_{REF} were selected. Although the exact geometry of the

generator housing installed in the Carleton Hydrokinetic Turbine will depend on the manufacturer, the overall dimensions and shape are expected to conform to these conventional specifications.

The geometry of the downstream end of the generator housing creates a sudden expansion in cross-sectional flow area in the exhaust duct. This will likely cause the flow to separate and re-circulate downstream of the generator housing, which will reduce the pressure-recovery performance of the exhaust duct. One option to improve the pressure-recovery performance of the exhaust duct of the Carleton Hydrokinetic Turbine is to tailor the generator housing into a more streamlined shape. Another option to prevent the sudden expansion in cross-sectional flow area at the downstream end of the generator housing is to contour the exhaust duct shown in Figure 3.17 into a more complicated shape that provides a gradual increase in cross-sectional area with streamwise distance. These options are not pursued in the present study, which is aimed at evaluating the pressure-recovery performance of an exhaust duct with a conventional conical shape.

3.6.2 Boundary Conditions

3.6.2.1 Axial Intake Boundary Conditions

The stagnation pressure, direction and turbulence intensity of the flow are specified at the axial intake boundary of the exhaust duct computational domain. These properties are specified separately for the bypass and turbine discharge areas of the axial intake boundary.

The bell-mouth axial intake of the Carleton Hydrokinetic Turbine is designed to turn the local water currents and align the flow with the centerline axis of the exhaust duct over a range of inclination angles. Due to the limited length of the bell-mouth passage, it is likely that there will be some residual misalignment of the flow and some variation in the stagnation pressure profile through the bypass area of the axial intake of the exhaust duct, especially at high inclination angles. Therefore, the present study includes an evaluation of the sensitivity of the pressure-recovery performance of the exhaust duct to the stagnation pressure distribution around the bypass area of the axial intake boundary. The effect of misalignment of the bypass flow on the pressure-recovery performance of the exhaust duct is not evaluated in this study.

For the simulations of the flow through the exhaust duct, the stagnation pressure of the bypass flow at the axial intake boundary was set equal to the stagnation pressure of the local water currents, the flow direction was set perpendicular to the axial intake boundary plane, and the turbulence intensity was set to 5%. The sensitivity of the pressure-recovery performance of the exhaust duct to the specified turbulence intensity is included in the present study.

The flow that passes through the turbine rotor will likely have some residual swirl when it reaches the axial intake of the exhaust duct. This swirl could be removed with the addition of a row of stators after the turbine assembly, and is assumed to be negligible in the present study. The flow discharging from the turbine rotor at the axial intake of the computational domain will have a uniform stagnation pressure lower than the stagnation

pressure of the local water currents due to the extraction of mechanical energy from the fluid as it passes through the turbine. The value of the stagnation pressure drop in the flow across the turbine rotor is calculated in Appendix L, for an axial turbine that is suitable for integration with the Carleton Hydrokinetic Turbine. The flow direction was set perpendicular to the boundary, and the turbulence intensity of the flow discharging from the turbine was set to 5%. The sensitivity of the pressure-recovery performance of the exhaust duct to the stagnation pressure drop across the turbine rotor is included in the present study.

3.6.2.2 Side Intake Boundary Conditions

The side intake boundary of the computational domain is located at the throat of the side intake of the Carleton Hydrokinetic Turbine and excludes the contoured entrance region. Two-dimensional simulations of the flow through the side intake were performed to provide stagnation pressure, turbulence kinetic energy and turbulence dissipation rate profiles to apply at the side intake boundary of the exhaust-duct computational domain. The curvature of the outer shell of the Carleton Hydrokinetic Turbine is designed to smoothly guide the local water currents into the exhaust duct over a range of inclination angles. Therefore the flow profile at the throat of the side intake is not expected to change significantly as the inclination angle changes. For each side intake width, the flow profile from a single two-dimensional simulation corresponding to $\alpha = 90$ deg. was applied as a boundary condition for simulations of the flow through the exhaust duct at multiple inclination angles. The location of the two-dimensional computational domain is shown in Figure 3.18.

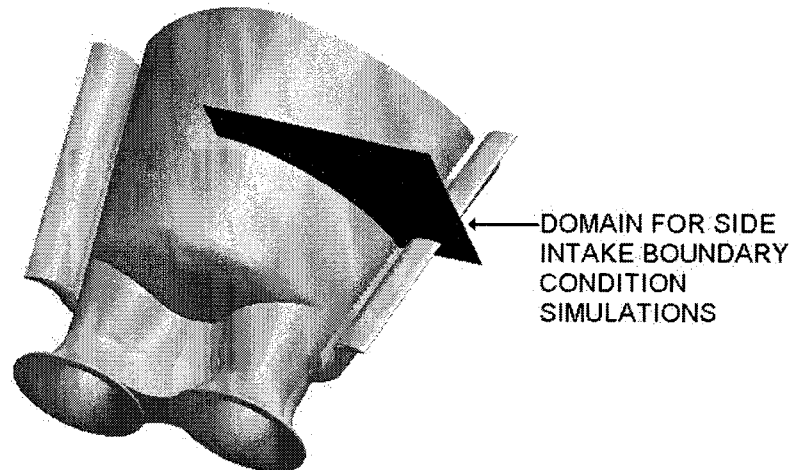


Figure 3.18 Location of Domain for Side Intake Boundary Condition Simulations

An image of the computational domain and the grid used for the two-dimensional simulations of the flow for the side intake boundary conditions is shown in Figure 3.19. The stagnation pressure at the inlet boundary of the computational domain for the two-dimensional flow simulations was set equal to the stagnation pressure of the local water currents, the flow direction was set perpendicular to the boundary, and the turbulence intensity was set to 5%. The computational domain has two outlet boundaries; one representing the area where the flow enters the side intake of the exhaust duct and one representing the area where the local water currents continue past the Carleton Hydrokinetic Turbine. The average reference static pressure at both boundaries was set to zero and the first derivatives of the flow variables in the direction perpendicular to the boundary plane were set to zero (Neumann boundary conditions).

The grid-convergence of the solution was evaluated by selectively refining the grid-node spacing and the height of the first grid-node in the wall-normal direction. The solution was considered to be converged when there was less than a 1% change in

maximum velocity and turbulence kinetic energy at the outlet boundary representing the flow entering side intake of the exhaust duct, when the grid-node spacing near this outlet boundary was halved and the height of the first grid-node in the wall-normal direction was halved. The effect of the location of the domain inlet and the free-slip wall on the stagnation pressure and turbulence properties of the flow entering the side intake of the exhaust duct was evaluated by completing simulations with the distance from the side intake to the domain inlet and the free-slip wall doubled. The results indicate that the selected location of the domain inlet and free-slip wall boundaries has negligible impact on the flow entering the side intake of the exhaust duct.

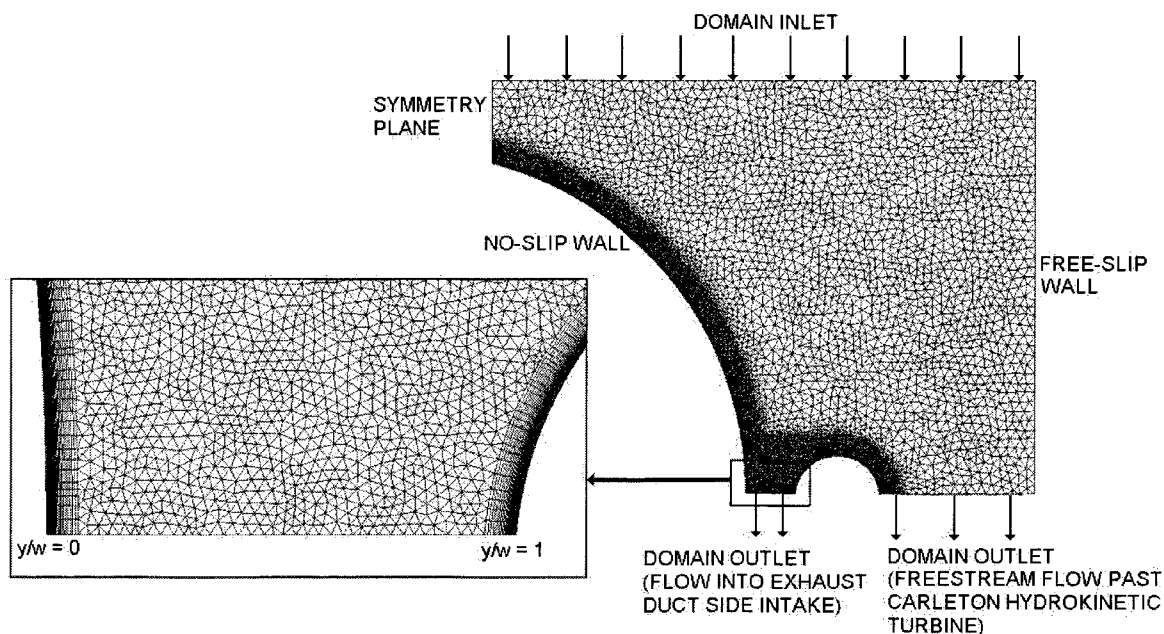


Figure 3.19 Computational Domain for Side Intake Boundary Condition Simulations

Due to the diffusing nature of the flow through the interior of the exhaust duct, the average static pressure at the throat of the side intake varies along the length of the exhaust duct. The average static pressure of the flow continuing past the exhaust duct is

dictated by the flow field around the contours of the Carleton Hydrokinetic Turbine. Therefore, it may not be realistic to apply the same average static pressure to both outlet boundaries of the computational domain. The difference in static pressure between the outlet boundaries dictates the location of the stagnation point on the side intake lip. With proper design of the rounded lip, it is expected that the minor variations in the location of this stagnation point will not significantly affect the profile of the flow entering the side intake of the exhaust duct. Examples of the stagnation pressure and turbulence kinetic energy profiles the two-dimensional simulations yielded for various side intake widths are shown in Figure 3.20 and Figure 3.21. To test the sensitivity of the pressure-recovery performance of the exhaust duct to the flow profile at the side intake, the side-intake stagnation pressure and turbulence profiles were replaced with a uniform stagnation pressure equal to the stagnation pressure of the local currents ($P_{o\text{ REF}}$) and a turbulence intensity of 5%. The simulation results indicate that applying these boundary conditions to the side intake boundary changes the pressure-recovery performance of the exhaust duct by less than 1%.

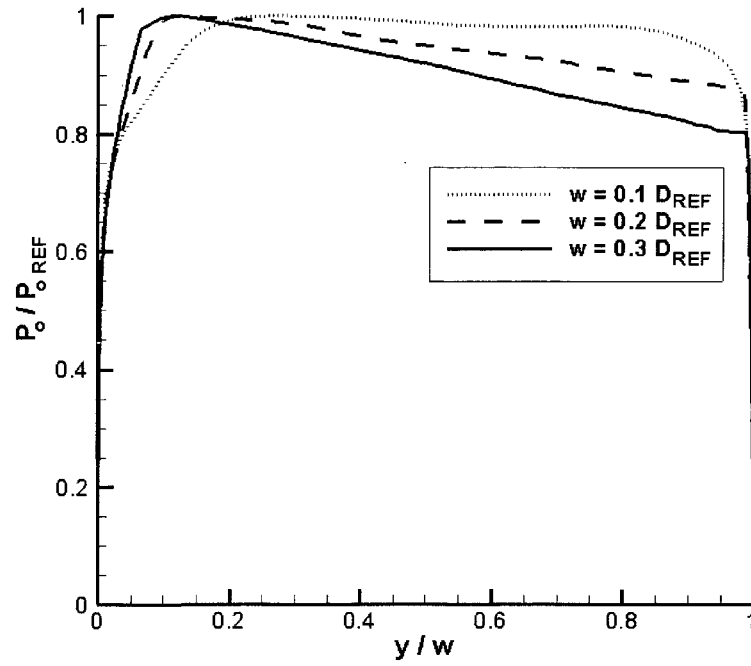


Figure 3.20 Stagnation Pressure Profile for Side Intake Boundary Condition

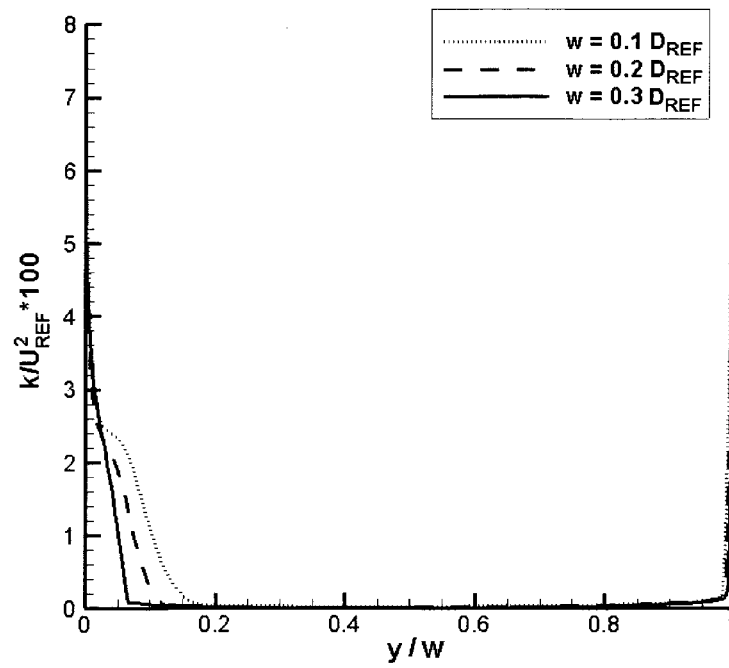


Figure 3.21 Turbulence Kinetic Energy Profile for Side Intake Boundary Condition

3.6.2.3 Outlet Boundary Conditions

The outlet boundary of the computational domain coincides with the axial outlet plane of the exhaust duct of the Carleton Hydrokinetic Turbine. The area-averaged static pressure was fixed at this plane, and the derivatives of the flow variable in the direction perpendicular to the boundary plane were set to zero (Neumann boundary condition).

3.6.2.4 Wall Boundary Conditions

The walls were set as smooth, no-slip walls on the inside of the exhaust duct and the exterior of the bulb-shaped enclosure housing the generator assembly.

3.6.3 Grid Convergence Study

A grid convergence study was performed to ensure the predicted pressure-recovery performance of the exhaust duct is independent of the grid-node spacing. A grid with tetrahedral elements was applied to the domain and systematically refined in areas of high spatial gradients of flow variables in order to establish grid-independency. The effect of the grid-node spacing on the solution was determined by examining the velocity and turbulence kinetic energy profiles along the side intake, axial intake and center of the exhaust duct. The effect of the wall-normal grid refinement on the solution was determined by examining the velocity and turbulence profiles of the boundary layer for variations in the height of the first grid-node in the wall-normal direction and the number of inflation layers resolving the boundary-layer flow. The grid-node spacing was selected to ensure low-Reynolds-number modeling of the boundary-layer flow, which requires a $y^+ < 2$ throughout the domain and at least 15 grid-nodes across the local thickness of the

boundary layer. The total grid-node count for the grid-independent solution of the flow through the exhaust duct is 2.5×10^6 . Images of the grid used to evaluate the pressure-recovery performance of the exhaust duct are shown in Figure 3.22.

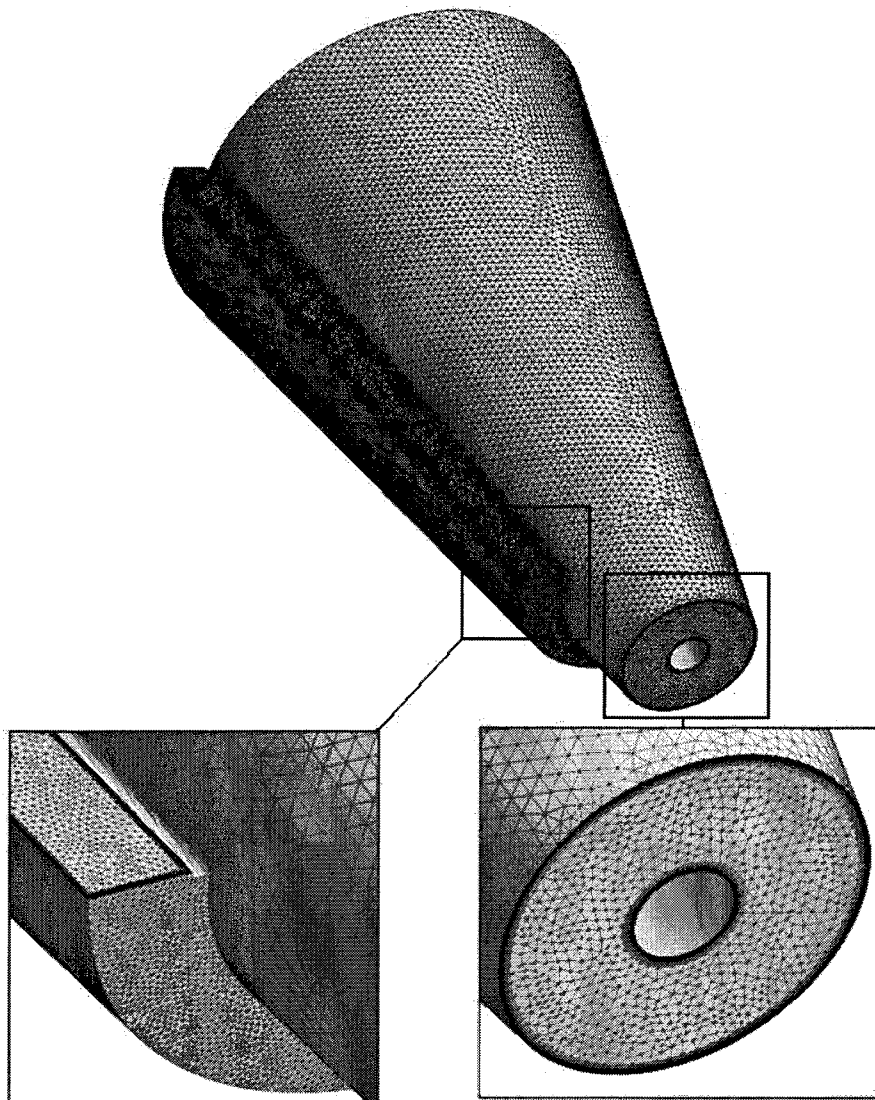


Figure 3.22 Computational Grid for Evaluation of Exhaust Duct Performance

3.6.4 Exhaust Duct Flow Field and Pressure-Recovery Performance

3.6.4.1 Exhaust Duct Geometry for Improved Pressure-Recovery Performance

The sensitivity of the pressure-recovery performance of the exhaust duct to the exhaust duct geometry was evaluated by systematically changing each geometric parameter. The pressure-recovery performance of the exhaust duct was quantified using the mass flow rate across the turbine (\dot{m}_T), normalized by a reference mass flow rate ($\dot{m}_{REF} = \rho U_{REF} \pi \left(\frac{D_{REF}}{2}\right)^2$) based on the local free-stream velocity (U_{REF}). The normalized mass flow rate (\dot{m}_T/\dot{m}_{REF}) provides a conservative estimate of the pressure-recovery performance of the exhaust duct, since the mass flow rate through an unshrouded turbine of the same diameter in the same flow should be less than \dot{m}_{REF} . The test matrix used to evaluate the exhaust duct pressure-recovery performance with changes in exhaust duct geometry is presented in Table 3.1. The exhaust duct geometries were evaluated for inclination angles (α) ranging from 30 deg. to 70 deg.

Table 3.1 Geometric Parameters for Evaluation of Exhaust Duct Performance

Geometric Parameter	Symbol	Min. Value	Max. Value
Exhaust Duct Opening Angle	2θ	16 deg.	24 deg.
Side Intake Width	w	0.1 D_{REF}	0.4 D_{REF}
Axial Intake Diameter (Including Bypass)	D_{IN}	1.0 D_{REF}	1.75 D_{REF}
Exhaust Duct Length	L	5.5 D_{REF}	6.5 D_{REF}

3.6.4.2 Predicted Exhaust Duct Pressure-Recovery Performance

The exhaust duct geometry selected for further evaluation has an opening angle (2θ) of 20 deg., an exhaust duct length (L) of 6.5 D_{REF} , an axial intake diameter (D_{IN}) of 1.25 D_{REF} , and a side-intake width (w) of 0.3 D_{REF} . This geometry was selected because it

was shown to provide the greatest increase in mass flow rate through the turbine rotor over the largest range of inclination angles. The effect of the inclination angle on the pressure-recovery performance of this exhaust duct geometry is shown in Figure 3.23. For this geometry, the simulations predict that the normalized mass flow rate across the turbine will vary from 1.07 to 1.26 for $30 \text{ deg.} < \alpha < 70 \text{ deg.}$, with the highest mass flow rate corresponding to $\alpha = 65 \text{ deg.}$ These results demonstrate that with the correct geometry, the exhaust duct of the Carleton Hydrokinetic Turbine is effective at increasing the mass flow rate through the turbine rotor over a wide range of inclination angles. The results from a simulation with no mass inflow through the side intake (approximately corresponding to $\alpha = 0 \text{ deg.}$ in Figure 3.23) predict a normalized mass flow rate of 0.84, indicating that the flow from the side intake is essential to improve the pressure-recovery performance of the exhaust duct as expected.

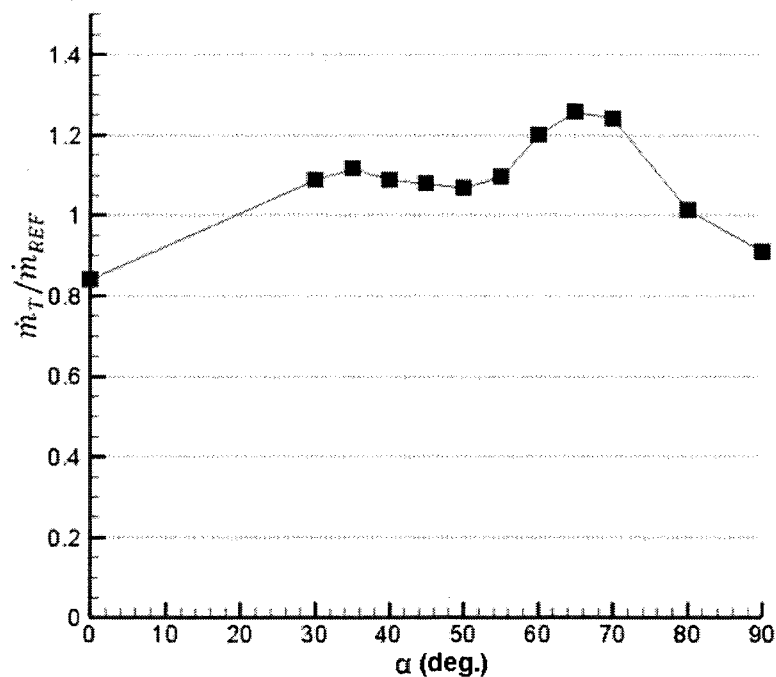


Figure 3.23 Effect of Inclination Angle (α) on Exhaust Duct Performance

3.6.4.3 Predicted Exhaust Duct Flow Field at $\alpha = 60$ deg.

The flow through the exhaust duct is examined in detail for an inclination angle of $\alpha = 60$ deg. Understanding the flow through the exhaust duct at this inclination angle allows for further discussion of the impact of the inclination angle on the pressure-recovery performance of the exhaust duct, which is presented in the next section.

The flow field through the exhaust duct at $\alpha = 60$ deg. is shown in multiple planes for three different views in Figure 3.24 to Figure 3.26, with an arrow representing the velocity magnitude of the local free-stream velocity (U_{REF}) provided as a scale. The simulation results indicate that the flow from the side intake follows the contours of the exhaust duct and its tangential component prevents the boundary layer from separating from the exhaust duct walls around the circumference of the exhaust duct. The flow from the axial intake slows down as it diffuses through the exhaust duct, and the adverse pressure gradient causes a portion of this flow to reverse direction and form a recirculation zone (RCZ 1) in the core of the exhaust duct.

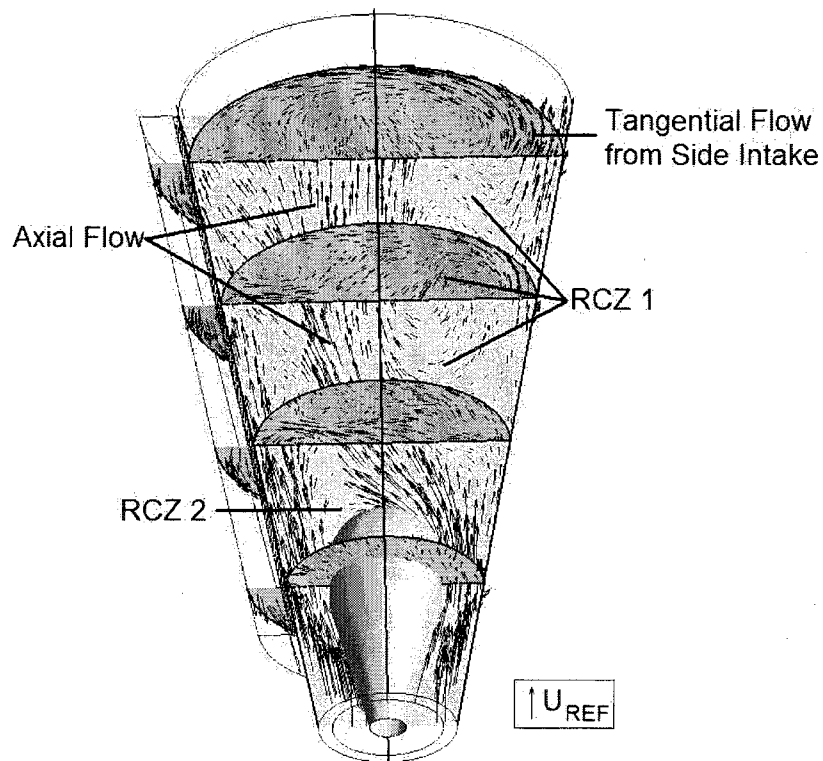


Figure 3.24 Flow Field through Exhaust Duct at $\alpha = 60$ deg. (View 1)

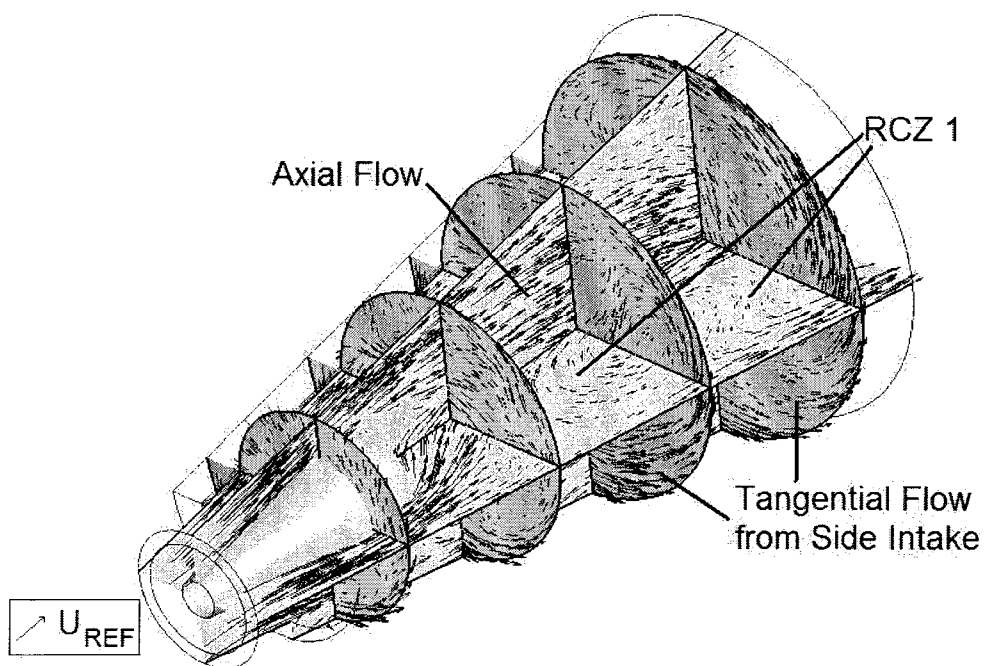


Figure 3.25 Flow Field through Exhaust Duct at $\alpha = 60$ deg. (View 2)

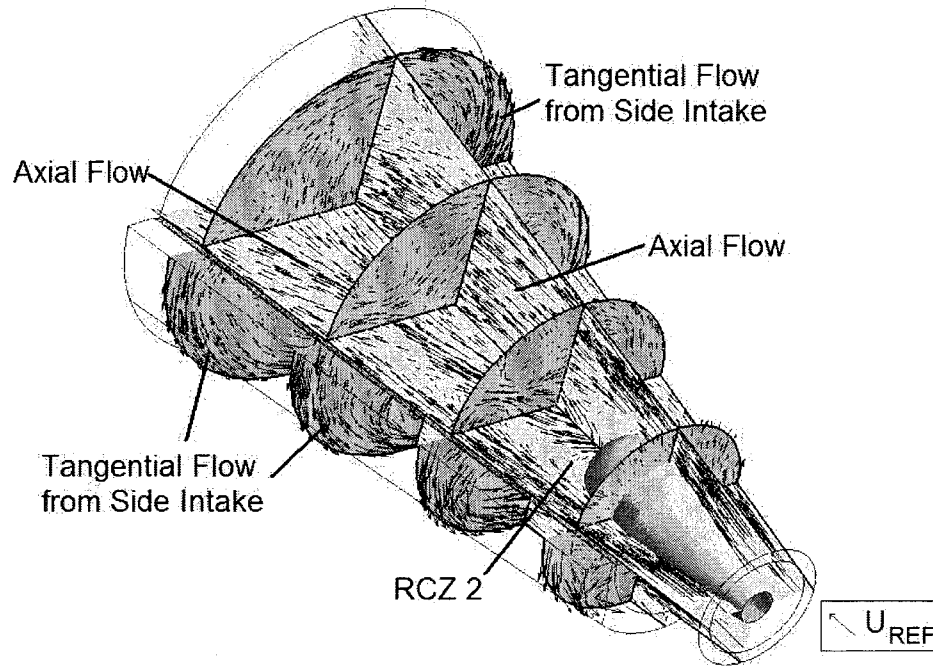


Figure 3.26 Flow Field through Exhaust Duct at $\alpha = 60$ deg. (View 3)

The recirculation zone labelled RCZ 2 in Figure 3.24 to Figure 3.26 is created by the flow separating over the downstream end of the generator housing. Since the CFD simulations were run for steady-state results, the flow separation is presented as a time-averaged recirculation zone. In reality, the flow separating off the downstream end of the generator housing is likely transient in nature. The small size of RCZ 2 suggests that efforts to streamline the generator housing will result in relatively small changes to the overall pressure-recovery performance of the exhaust duct. It may therefore be more effective to have future exhaust duct geometry optimization efforts concentrate on reducing the extent of the recirculation zone RCZ 1.

The axial velocity of the flow through the exhaust duct at $\alpha = 60$ deg. is presented in Figure 3.27. The streamlines clearly show that the flow discharging from the turbine

rotor is directed to one side of the exhaust duct and exits the axial discharge plane without recirculating. The high-pressure flow from the side intake creates a tangential force that redirects a small portion of the flow discharging from the turbine rotor. This redirected flow follows the contours of the exhaust duct walls to the axial discharge plane without recirculating. Although not shown in the figure below, the simulation results indicate that the recirculation zone RCZ 1 is composed of fluid entering the domain through the bypass area of the axial intake.

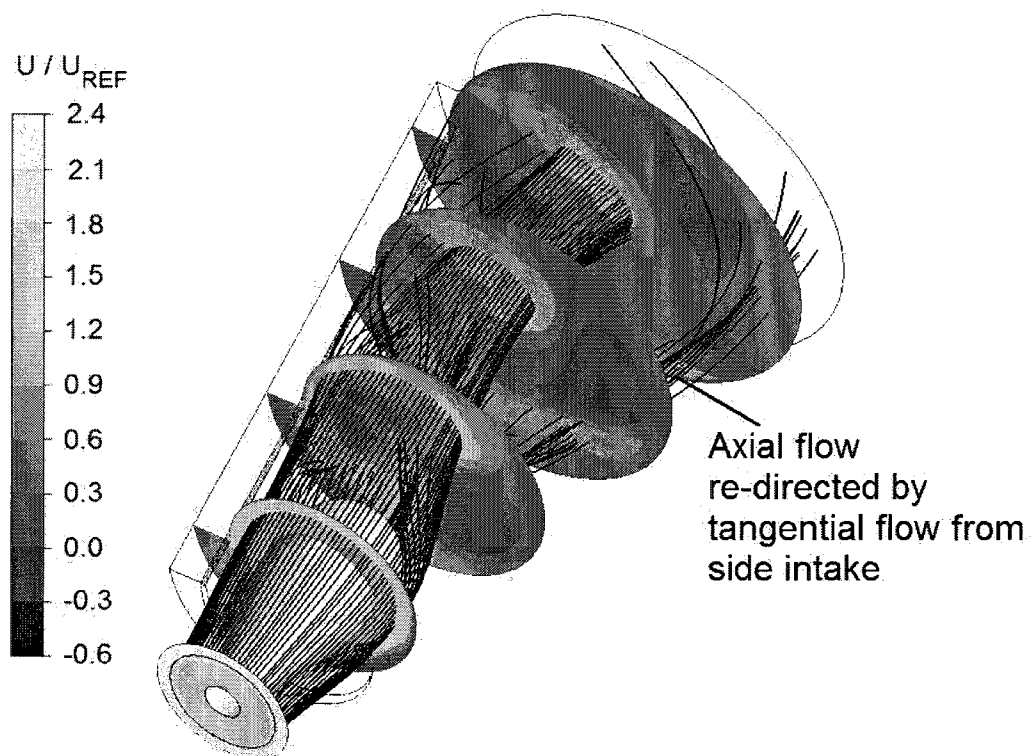


Figure 3.27 Axial Flow through Exhaust Duct at $\alpha = 60$ deg.

The static pressure field through the exhaust duct at $\alpha = 60$ deg. is presented in Figure 3.28. As expected, the diffusion of the flow through the exhaust duct causes the overall static pressure to increase with streamwise distance. A small, low-pressure area is

visible in Figure 3.28 (a) near the upstream end of the side intake. The axial flow past the generator housing creates this low-pressure area downstream of where the exhaust duct walls expand to include the side intake. This low-pressure area diffuses quickly and does not have a significant impact on the overall flow through the exhaust duct. The large low-pressure area towards the downstream end of the exhaust duct corresponds to the recirculation zone RCZ 1, as shown by the streamlines superimposed on the pressure field in Figure 3.28 (b). This low-pressure area develops to counter the centrifugal forces caused by the streamline curvature of the flow and maintain radial equilibrium on the fluid particles in the exhaust duct.

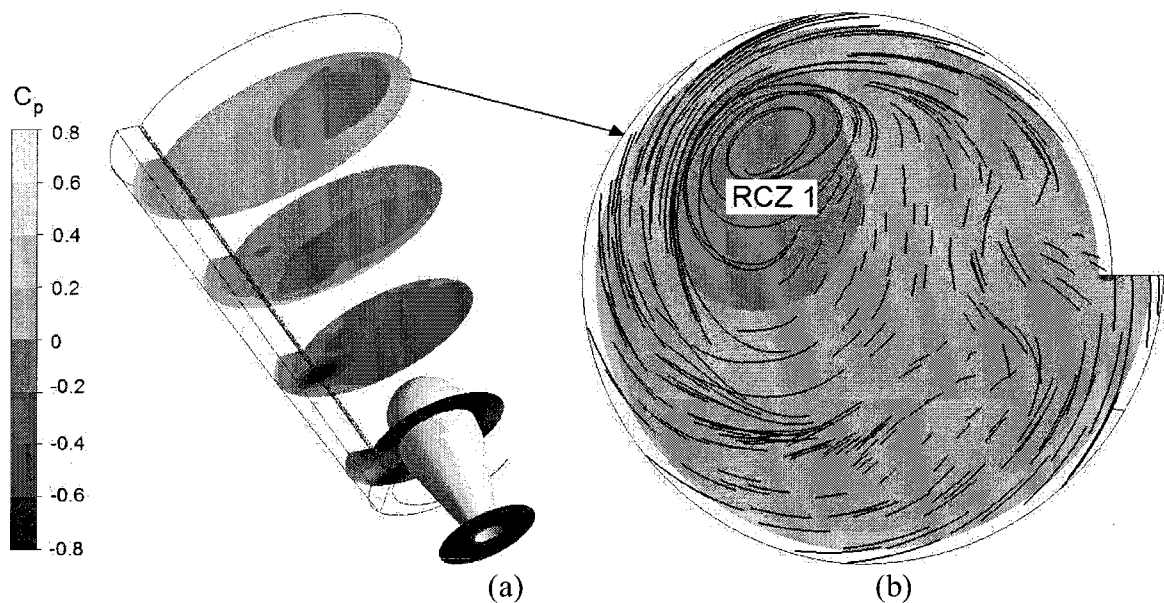


Figure 3.28 Static Pressure Field through Exhaust Duct at $\alpha = 60$ deg.

The stagnation pressure of the flow through the exhaust duct at $\alpha = 60$ deg. is presented in Figure 3.29, with vectors of the tangential flow superimposed on each contour plot. The tangential momentum of the flow from the side intake prevents

boundary-layer separation along the walls of the exhaust duct. This high-pressure flow blocks the lower-pressure flow from the axial intake from interacting directly with the no-slip boundary along the exhaust duct walls. Since the flow from the side intake has an axial velocity component similar in magnitude to the flow from the axial intake, the flow from the axial intake is not constrained by a zero-velocity condition around its outer radius. This reduces the losses in axial momentum through the exhaust duct, which subsequently reduces the size of the recirculation zone RCZ 1. A smaller recirculation zone improves the pressure-recovery performance of the exhaust duct.

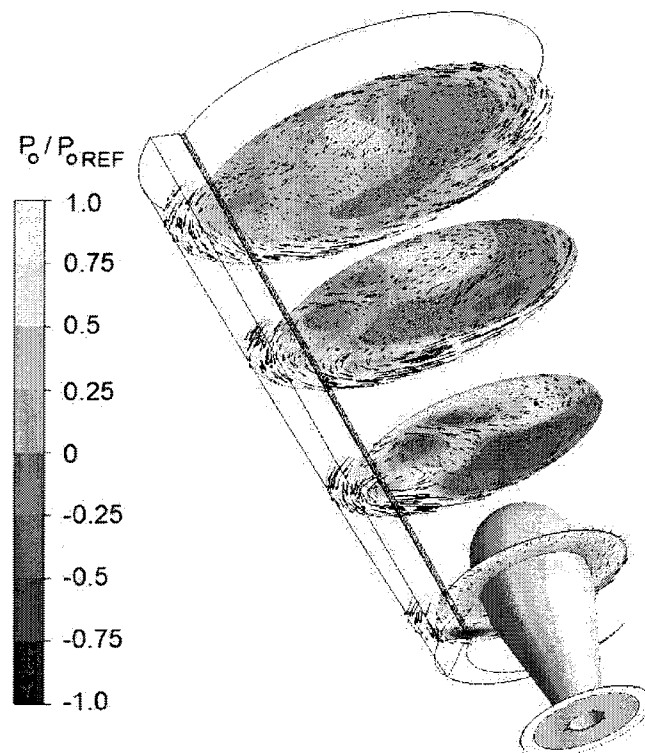


Figure 3.29 Stagnation Pressure Field through Exhaust Duct at $\alpha = 60$ deg.

3.6.4.4 Effect of Inclination Angle on Exhaust Duct Flow Field

The effect of the inclination angle on the flow field through the exhaust duct is examined in detail for $\alpha = 30$ deg., $\alpha = 60$ deg. and $\alpha = 90$ deg. These inclination angles were selected because they create three distinct flow fields, only one of which significantly improves the mass flow rate through the turbine rotor. Streamlines of the flow from the side intake through the exhaust duct are shown in Figure 3.30.

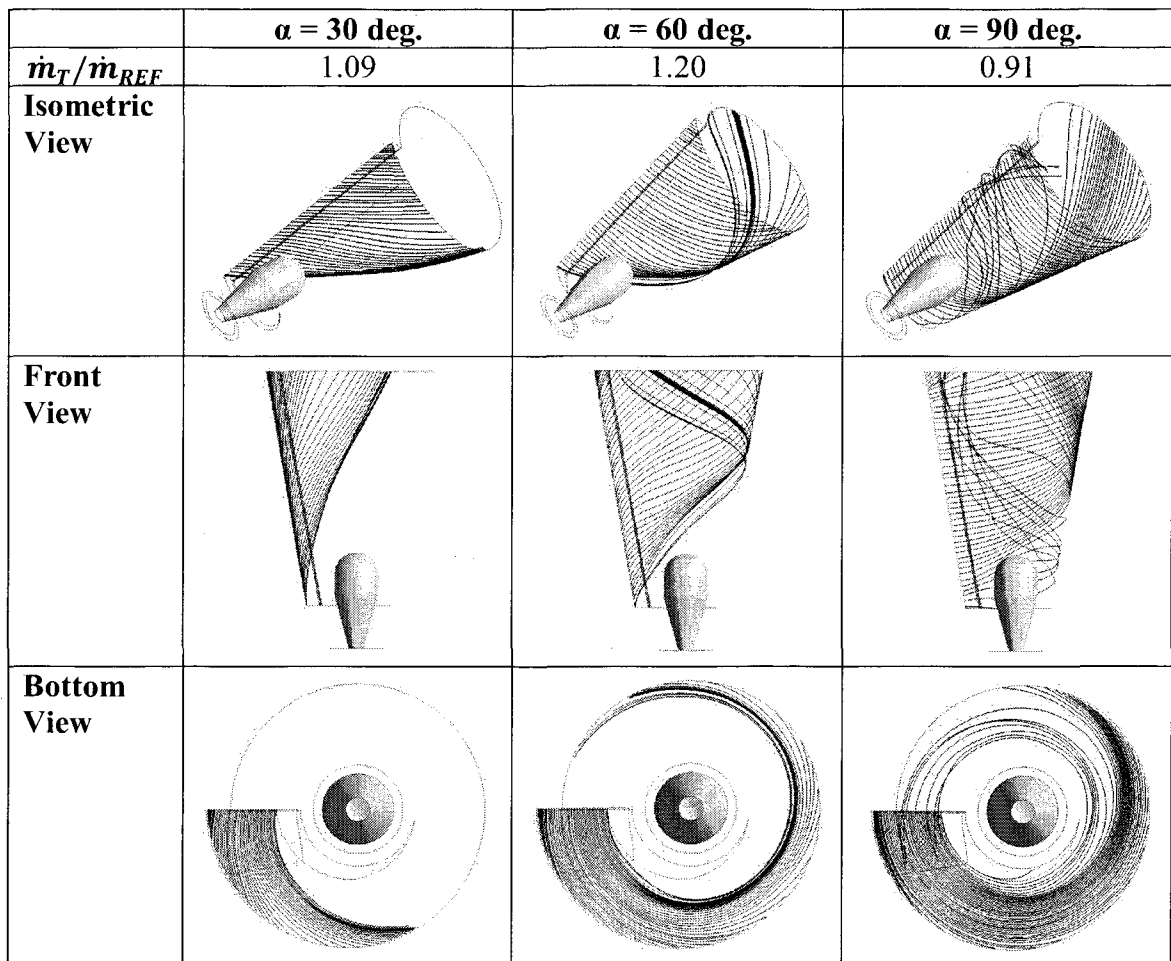


Figure 3.30 Side Intake Flow through Exhaust Duct for Multiple Inclination Angles

At $\alpha = 30$ deg., the inclination angle dictates that the flow through the side intake has more axial momentum than tangential momentum. The flow from the side intake remains attached to the walls of the exhaust duct, but reaches the axial discharge plane before travelling around more than a quarter of the circumference of the exhaust duct, as shown in Figure 3.30. Therefore, the flow from the axial intake is constrained over a large area by the no-slip boundary condition along the exhaust duct walls. The no-slip boundary condition reduces the momentum of the flow from the axial intake, resulting in a larger recirculation zone RCZ 1 and a reduction in the pressure-recovery performance of the exhaust duct. The flow field through the exhaust duct at $\alpha = 30$ deg. is presented in Figure 3.31 and Figure 3.32.

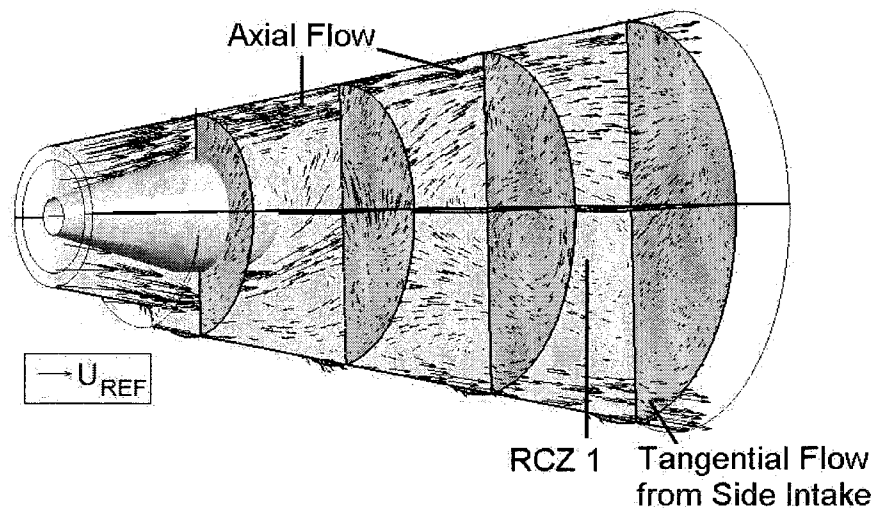


Figure 3.31 Flow Field through Exhaust Duct at $\alpha = 30$ deg. (Side View)

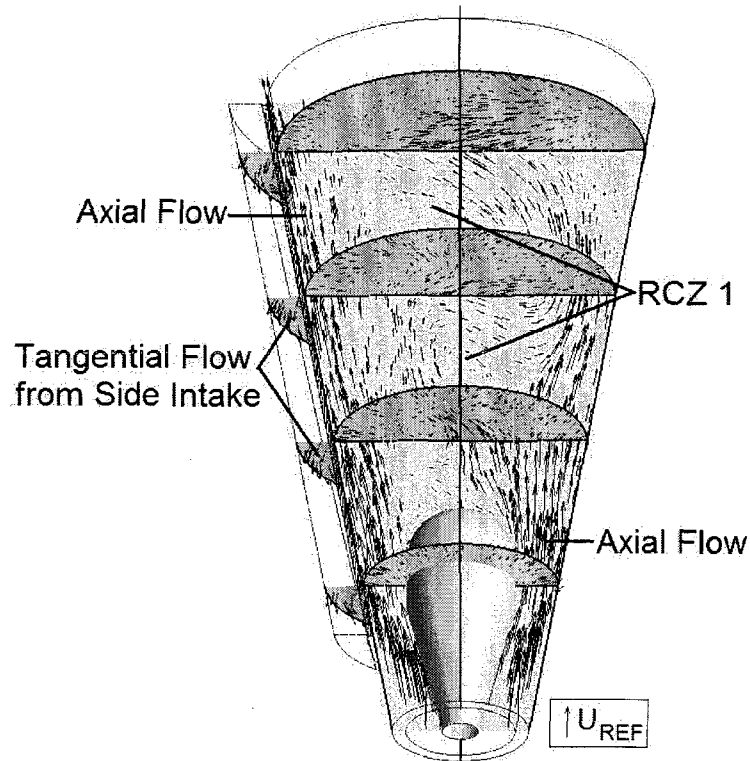


Figure 3.32 Flow Field through Exhaust Duct at $\alpha = 30$ deg. (Front View)

At $\alpha = 60$ deg., the inclination angle dictates that the flow through the side intake has more tangential momentum than axial momentum. The flow from the side intake remains attached to the walls of the exhaust duct, and travels around more than three-quarters of the exhaust duct circumference before reaching the axial discharge plane, as shown in Figure 3.30. Therefore, the flow from the axial intake is constrained over a smaller area by the no-slip boundary condition along the exhaust duct walls. The axial velocity component of the flow from the side intake is comparable to that of the flow from the axial intake, resulting in little interaction through shear forces between the two flows. Overall, there is a smaller loss in axial momentum in the flow from the axial intake, which reduces the size of the recirculation zone RCZ 1 and increases the pressure-

recovery performance of the exhaust duct. The flow field through the exhaust duct at $\alpha = 60$ deg. is presented in Figure 3.33 and Figure 3.34.

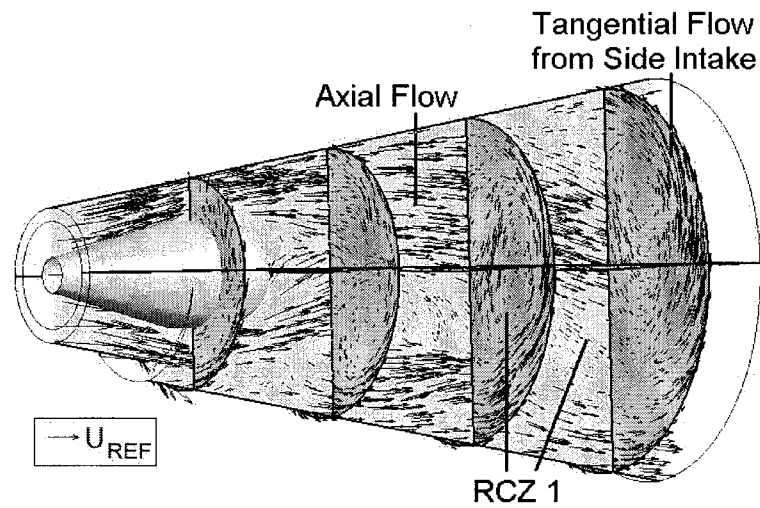


Figure 3.33 Flow Field through Exhaust Duct at $\alpha = 60$ deg. (Side View)

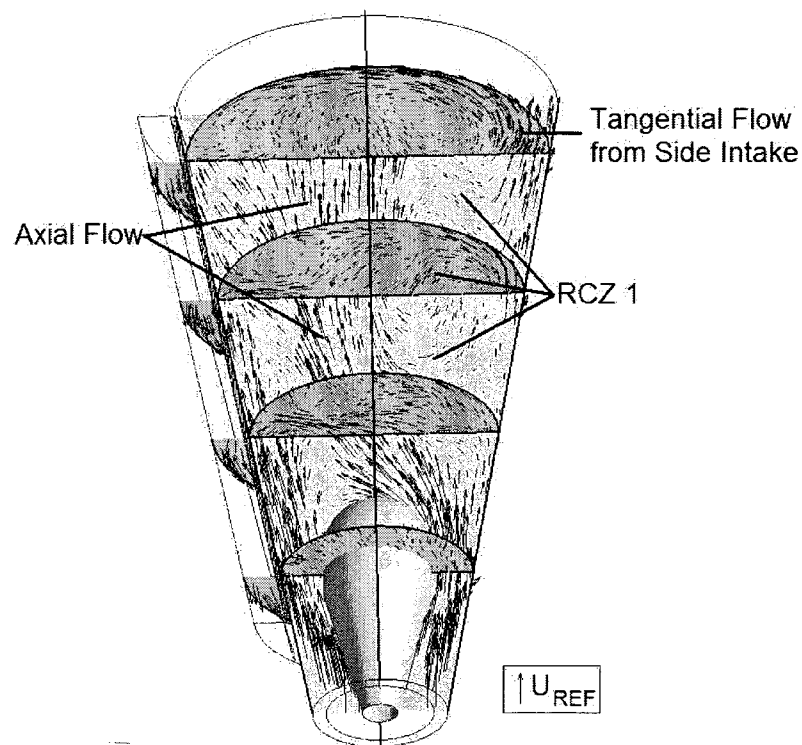


Figure 3.34 Flow Field through Exhaust Duct at $\alpha = 60$ deg. (Front View)

At $\alpha = 90$ deg., the inclination angle dictates that the flow through the side intake has no axial momentum. The flow from the side intake remains attached to the walls of the exhaust duct, and gains an axial component through shear force interaction with the flow from the axial intake. The trajectory of the flow from the side intake causes it to travel around more than three-quarters of the exhaust duct circumference before reaching the axial discharge plane, as shown in Figure 3.30. Therefore, the flow from the axial intake is constrained over a smaller area by the no-slip boundary condition along the exhaust duct walls. However, since the flow from the side intake has no axial component, there is significant interaction through shear forces between the flow from the axial intake and the flow from the side intake. This results in a reduction in the axial momentum of the flow from the axial intake, similar to the case with no mass inflow through the side intake presented in Section 3.6.4.2. The reduction in axial momentum increases the size of the recirculation zone RCZ 1 and reduces the pressure-recovery performance of the exhaust duct. The flow field through the exhaust duct at $\alpha = 90$ deg. is presented in Figure 3.35 and Figure 3.36.

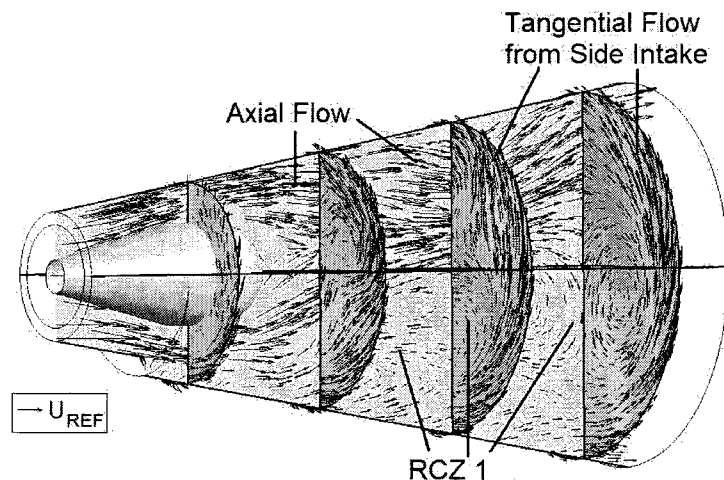


Figure 3.35 Flow Field through Exhaust Duct at $\alpha = 90$ deg. (Side View)

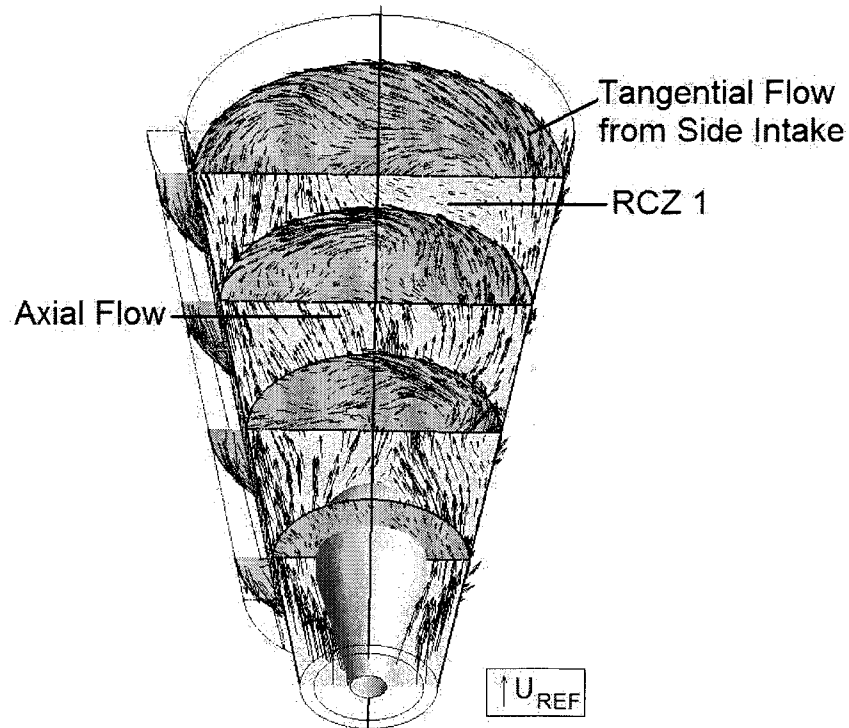


Figure 3.36 Flow Field through Exhaust Duct at $\alpha = 90$ deg. (Front View)

3.6.4.5 Sensitivity of Exhaust Duct Pressure-Recovery Performance to Boundary Conditions

One of the assumptions made regarding the bypass flow through the axial intake boundary was that the stagnation pressure is spatially uniform. As mentioned in the relevant boundary-condition section, there will likely be some variation in the stagnation pressure profile at the throat of the axial intake due to the limited length of the bell-mouth inlet, particularly at high inclination angles. To evaluate the sensitivity of the exhaust duct pressure-recovery performance to the axial intake boundary conditions, simulations were performed with a stagnation pressure profile over the bypass area of the axial intake varying from 50% to 100% of the stagnation pressure of the local water currents. The simulation results predict that a highly non-uniform stagnation pressure profile at the

bypass area of the axial intake reduces the normalized mass flow rate through the turbine rotor to 0.98 at $\alpha = 60$ deg. The reduction in stagnation pressure reduces the axial momentum of the flow through the bypass area, which increases the size of the recirculation zone RCZ 1. Therefore, it is important that the design of the bell-mouth intake of the Carleton Hydrokinetic Turbine aligns the incoming flow with the centerline of the exhaust duct with minimal losses in stagnation pressure.

The sensitivity of the pressure-recovery performance of the exhaust duct to the stagnation pressure drop across the turbine assembly is evaluated, since the stagnation pressure drop calculated in Appendix L is an estimate and will vary depending on the turbine design. For the sensitivity study, the stagnation pressure drop across the turbine rotor was set to half the value of the pressure drop calculated in Appendix L. The simulation results indicate that the reduction in stagnation pressure drop across the turbine rotor improves the pressure-recovery performance of the exhaust duct, with the normalized mass flow rate across the turbine increasing from 1.20 to 1.31 at $\alpha = 60$ deg. With a smaller stagnation pressure drop across the turbine rotor, there is an increase in the axial momentum of the flow through the axial intake. This reduces the size of the recirculation zone RCZ 1 and increases the pressure-recovery performance of the exhaust duct.

The sensitivity of the pressure-recovery performance of the exhaust duct to the specified turbulence intensity at the axial intake boundary was evaluated for turbulence intensity levels ranging from 1% to 10%. For this range of turbulence levels, the simulations predict that the pressure-recovery performance of the exhaust duct will

change by less than 1%. This insensitivity of the SST turbulence model to the turbulence intensity specified at the intake boundary was also observed during the turbulence model validation study.

3.6.5 Sensitivity of Exhaust Duct Pressure-Recovery Performance to Variations in Geometry

The sensitivity of the pressure-recovery performance of the exhaust duct to variations in the exhaust duct geometry is presented in this section for an exhaust duct length of $6.5 D_{REF}$. This length was selected after an iterative study indicated that for shorter exhaust duct lengths the residence time of the flow from the side intake in the exhaust duct is insufficient to improve the pressure-recovery performance of the exhaust duct. Once an exhaust duct length of $6.5 D_{REF}$ was shown to improve the pressure-recovery performance of the exhaust duct, longer exhaust duct lengths were not evaluated due to practical size limitations. For a given turbine size, a longer exhaust duct length would limit the depth of water for which the device could be installed since there must be sufficient clearance to allow for safe passage of ship traffic in the area.

3.6.5.1 Effect of Side Intake Width (w) on Exhaust Duct Pressure-Recovery Performance

The effect of side intake width on the pressure-recovery performance of the exhaust duct was evaluated for $2\theta = 20$ deg., $L = 6.5 D_{REF}$, and $D_{IN} = 1.25 D_{REF}$. An exhaust duct geometry defined using these dimensions and a side intake width of $w = 0.3$

D_{REF} has been shown to improve the pressure-recovery performance of the exhaust duct.

The results of the study are shown in Figure 3.37.

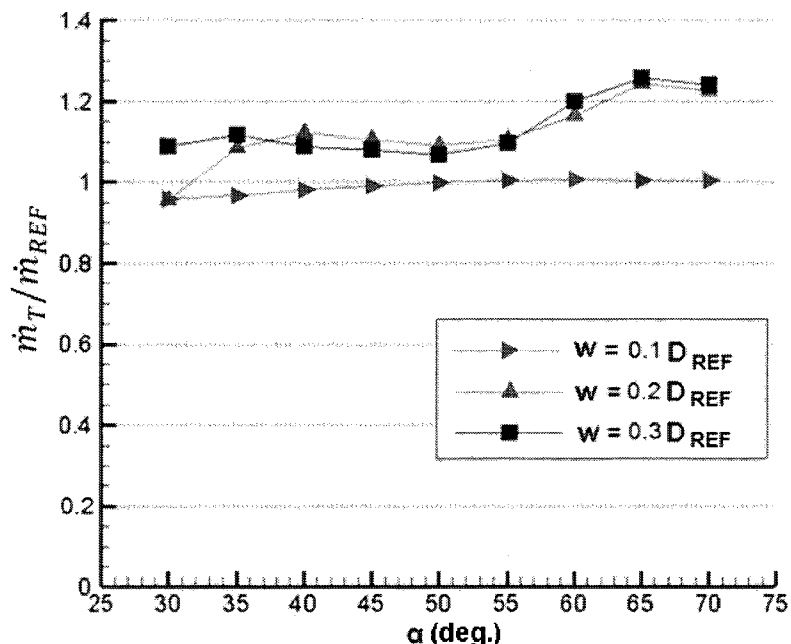


Figure 3.37 Effect of Side Intake Width on Exhaust Duct Performance

For a small side intake width ($w < 0.15 D_{REF}$), the mass flow rate through the side intake is reduced. Therefore, the flow from the axial intake has a greater influence on the flow from the side intake through shear forces and substantially increases its axial component of velocity. With this additional axial component of velocity, the flow from the side intake has insufficient tangential momentum to travel around the full circumference of the exhaust duct before reaching the axial discharge plane. Therefore, more of the flow from the axial intake is constrained by the no-slip boundary condition along the walls of the exhaust duct, the size of the recirculation zone RCZ 1 increases, and the pressure-recovery performance of the exhaust duct is reduced.

For a larger side intake width ($w > 0.2 D_{REF}$), the mass flow rate through the side intake is increased. Therefore, the flow from the axial intake has a smaller influence on the flow from the side intake through shear forces, and does not increase its axial component of velocity by the same amount as the case with a smaller side intake width. The flow from the side intake is therefore able to follow a trajectory that covers a larger portion of the exhaust duct walls before reaching the axial discharge plane. This reduces the area that the flow from the axial intake is influenced by the no-slip boundary condition along the exhaust duct walls, and the pressure-recovery performance of the exhaust duct improves. Increasing the side intake width to $w \geq 0.3 D_{REF}$ provides similar pressure-recovery performance as $w = 0.2 D_{REF}$, indicating that additional flow through the side intake does not further improve the pressure-recovery performance of the exhaust duct. The exhaust duct geometry recommended for further evaluation has a side intake width of $w = 0.3 D_{REF}$, which is a conservative design that provides sufficient mass flow through the side intake to improve the pressure-recovery performance of the exhaust duct regardless of any reasonable margin of error in the CFD predictions.

3.6.5.2 Effects of Axial Intake Diameter (D_{IN}) on Exhaust Duct Pressure-Recovery Performance

The effect of the axial intake diameter on the pressure-recovery performance of the exhaust duct was evaluated for $2\theta = 20$ deg., $L = D_{REF}$, and $w = 0.2 D_{REF}$. The exhaust duct geometry defined using these dimensions and an axial intake diameter of $D_{IN} = 1.25 D_{REF}$ has been shown to improve the pressure-recovery performance of the exhaust duct. The results of the study are shown in Figure 3.38.

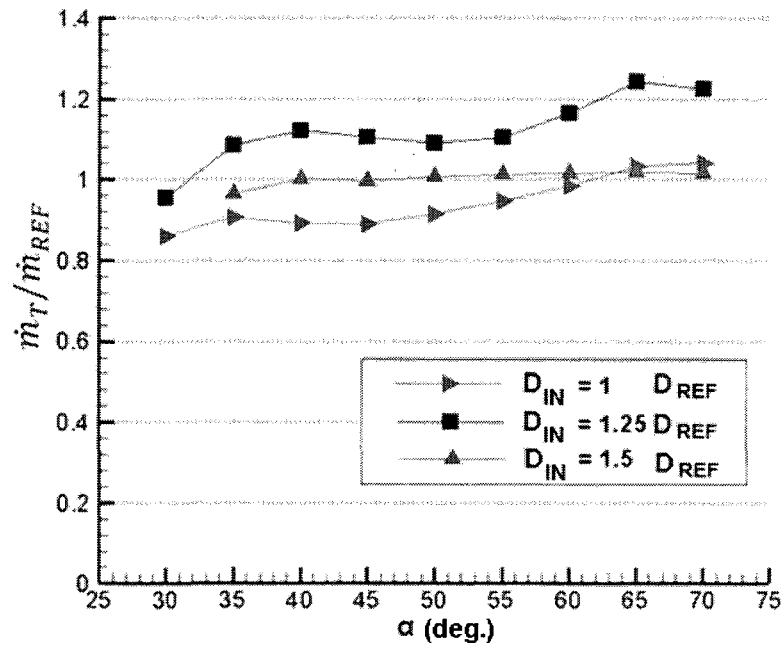


Figure 3.38 Effect of Axial Intake Diameter on Exhaust Duct Performance

For an axial intake diameter of $D_{IN} = D_{REF}$, the bypass area around the turbine assembly is completely removed. This results in a lower overall mass flow rate through the axial intake, since the area of the axial intake is reduced and the turbine rotor has lowered the flow stagnation pressure. The decrease in the axial momentum of the flow from the axial intake increases the size of the recirculation zone RCZ 1, which reduces the pressure-recovery performance of the exhaust duct.

For a larger axial intake diameter ($D_{IN} > 1.5 D_{REF}$), the mass flow rate through the axial intake increases, since the area of the axial intake increases and the bypass flow has a high stagnation pressure than the flow through the turbine rotor. The increase in axial momentum through the exhaust duct, in combination with the increase in the exhaust duct circumference, causes the flow from the side intake to travel around a smaller portion of

the exhaust duct before reaching the axial discharge plane. Therefore, more of the flow from the axial intake is constrained by the no-slip boundary condition along the walls of the exhaust duct, the size of the recirculation zone RCZ 1 increases, and the pressure-recovery performance of the exhaust duct is reduced.

3.6.5.3 Effects of Opening Angle (2θ) on Exhaust Duct Pressure-Recovery Performance

Performance

The effect of the opening angle on the pressure-recovery performance of the exhaust duct was evaluated for $L = 6.5 D_{REF}$, $w = 0.2 D_{REF}$, and $D_{IN} = 1.25 D_{REF}$. The results are shown in Figure 3.39.

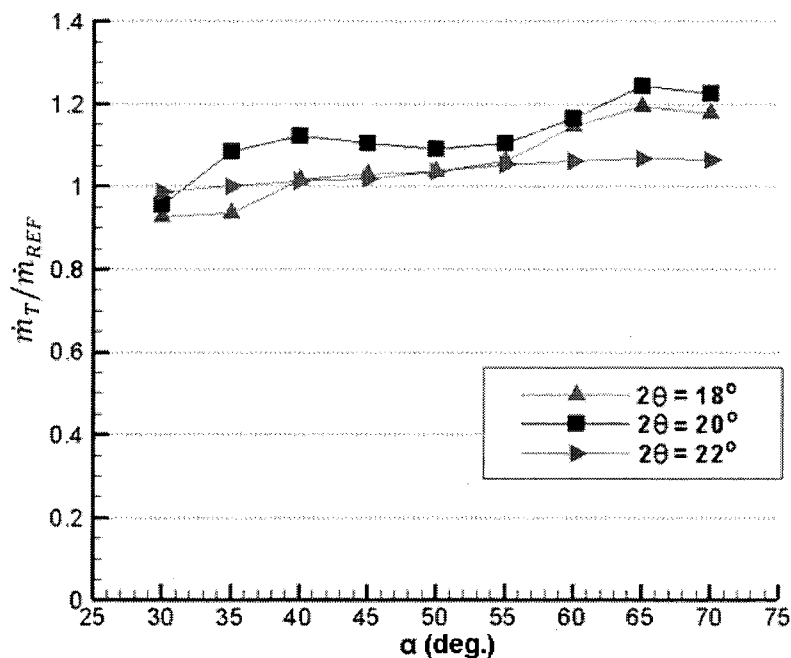


Figure 3.39 Effect of Opening Angle on Exhaust Duct Performance

For smaller exhaust duct opening angles ($2\theta = 18$ deg.), the flow from the side intake has sufficient tangential momentum to follow the contours of the exhaust duct

walls to the axial discharge plane without separating from the walls, providing similar flow patterns as the case where $2\theta = 20$ deg. The pressure-recovery performance of the exhaust duct is reduced for a smaller opening angle since there is a reduction in the diffuser area ratio. A smaller diffuser area ratio corresponds to a reduction in the pressure gradient that is used to increase the mass flow rate across the turbine assembly.

For larger exhaust duct opening angles ($2\theta = 22$ deg.), there is a larger diffuser area ratio and therefore a larger adverse pressure gradient acting through the exhaust duct. For the given geometry, the tangential momentum of the flow from the side intake is insufficient to keep the flow attached to the exhaust duct walls. The flow from the side intake separates from the exhaust duct walls, which increases the size of the recirculation zone RCZ 1 and decreases the pressure-recovery performance of the exhaust duct.

3.7 FLOW VISUALIZATION THROUGH THE CARLETON HYDROKINETIC

TURBINE EXHAUST DUCT IN A WATER CHANNEL

3.7.1 Manufacturing of the Exhaust Duct Model

A scale model of the Carleton Hydrokinetic Turbine exhaust duct was developed and tested in a laboratory water channel facility to produce flow visualization images that could corroborate the results of the computational efforts. The exhaust duct model is shown in Figure 3.40, with a scale included to provide an indication of its size. The walls of the exhaust duct model were formed using a 0.5 mm thick frosted plastic sheet that is flexible enough to easily bend into the shape of the exhaust duct and transparent enough to allow the operator to observe the dyes introduced into the flow. The plastic material

was formed into the desired shape using a support frame made out of brass. The side intake was held at the desired width using small brass spacers, as shown in Figure 3.41.

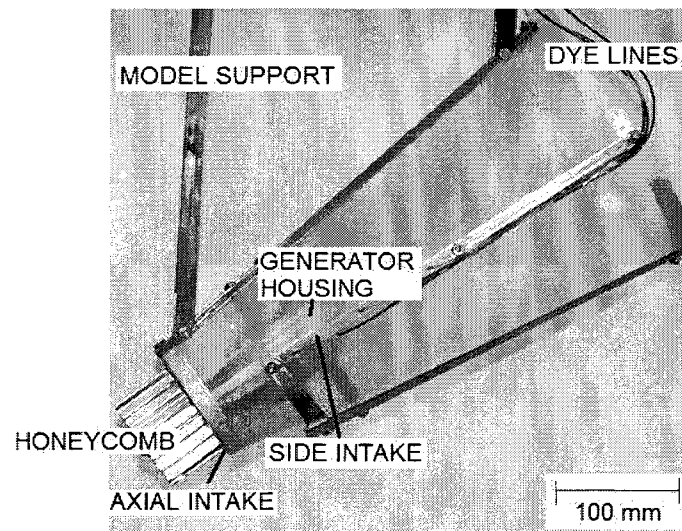


Figure 3.40 Scale Model of Carleton Hydrokinetic Turbine Exhaust Duct

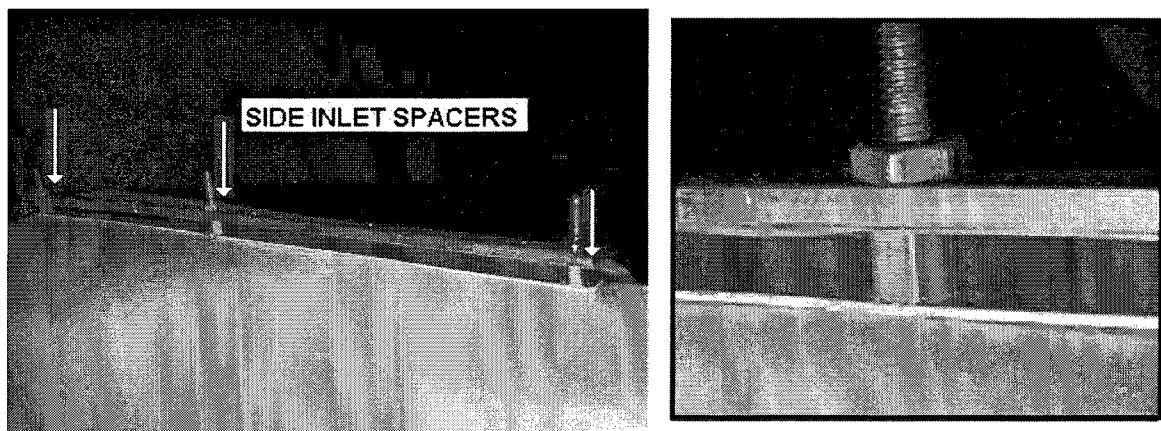


Figure 3.41 Brass Spacers for Maintaining Side Intake Width of Scale Model

The axial intake of the exhaust duct model contains a honeycomb section that aligns the flow with the axis of the exhaust duct and produces a stagnation pressure drop in relation to the bypass flow entering the exhaust duct through the annular opening

around the honeycomb. The pressure drop through the honeycomb is not meant to accurately represent the pressure drop that would be induced by an actual turbine; rather it is an idealized representation of one of the primary features of the axial intake of the full-scale Carleton Hydrokinetic Turbine. Simulations have shown that stagnation pressure drop across the turbine does not have a significant impact on the streamlines of the flow through the exhaust duct.

The honeycomb consists of hexagonal cells that are 7 mm wide and extend 45 mm in the direction of the flow. The length of the honeycomb should be 6 to 8 times larger than the cell diameter to ensure the flow is straightened and the larger turbulent structures are dissipated (Bradshaw & Mehta, 2003). The honeycomb is mounted over an aluminum solid body which protrudes into the exhaust duct to model the presence of the bulb-shaped generator assembly, as shown in Figure 3.42.

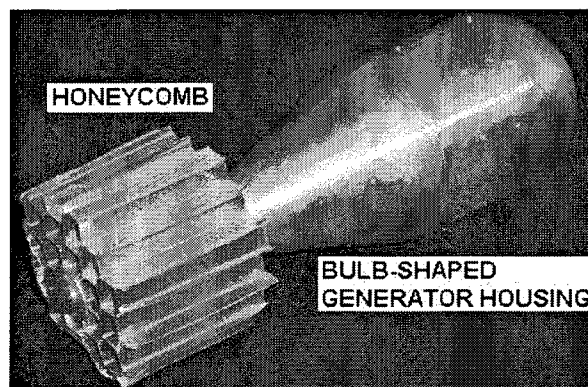


Figure 3.42 Honeycomb and Bulb-Shaped Generator Unit for Scale Model

The exhaust duct model was tested in a large-scale water channel facility that was added to the testing facilities of the Department of Mechanical and Aerospace

Engineering in March 2008. Details of the water channel facility and its flow visualization system can be found in Appendix M. Preliminary flow visualization exercises in the water channel facility are presented in Appendix N. The test section of the water channel is 0.61 m (24 in.) wide, 0.91 m (36 in.) deep and 1.83 m (72 in.) long. The water channel can provide a range of test section velocities, from 0.00254 m/s (0.1 in/s) to 0.3048 m/s (12 in/s). Up to six different colors of dye can be injected into the test section, with each color controlled using regulated compressed air. For the present experiments, the dye was introduced into the exhaust duct model through holes 2 mm in diameter along the side intake and bottom wall of the duct, as shown in Figure 3.43. The dye is injected into the exhaust duct flow perpendicular to the surface, and regulated so that it enters the exhaust duct at the same pressure as the rest of the flow. If the dye is injected at too high a pressure, it will disturb the boundary layer and change the flow-field through the exhaust duct.

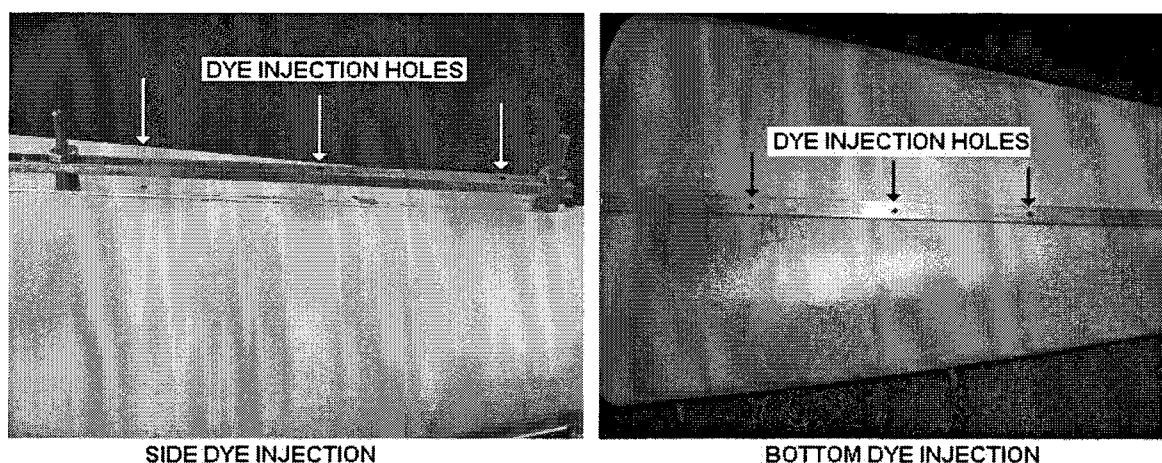


Figure 3.43 Dye Ports for Flow Visualization in Scale Model

The present flow visualization studies were performed with a test section velocity of 0.1 m/s (4 in/s), which corresponds to a Reynolds number of 4×10^3 based on an axial intake diameter of 50 mm. This is much lower than the Reynolds number that is expected in a typical field setting of the Carleton Hydrokinetic Turbine (1×10^6), and was selected to limit dye diffusion during the flow visualization study. The effect of the reduction in Reynolds number on the exhaust duct was determined using the CFD approach presented in the previous section. The results indicate that the streamline patterns and pressure-recovery performance of the scaled exhaust duct model are similar to the CFD results with the full-scale exhaust duct, despite the change in Reynolds number.

3.7.2 Evaluation of Exhaust Duct Performance Using Flow Visualization

3.7.2.1 Exhaust Duct with Geometry for Improved Performance

The geometry of the exhaust duct model was selected to match the geometry that was shown to be most effecting at improving the pressure-recovery performance of the exhaust duct in Section 3.6.4.1 ($L = 6.5 D_{REF}$, $w = 0.3 D_{REF}$, $D_{IN} = 1.25 D_{REF}$, $2\theta = 20$ deg.). The model was tested in the water channel for inclination angles of $\alpha = 30$ deg., $\alpha = 45$ deg. and $\alpha = 60$ deg.

Photographs of the flow through the exhaust duct model are shown in Figure 3.44 and Figure 3.45, and are compared to the streamlines predicted using CFD for the corresponding inclination angle. The transient nature of the flow separating over the downstream end of the generator assembly, mentioned in Section 3.6.4.3, does not appear to affect the streamlines of the flow in the exhaust duct.

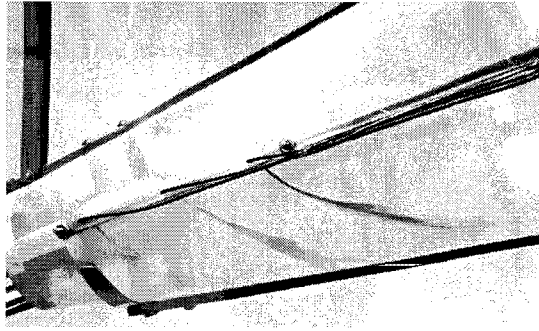
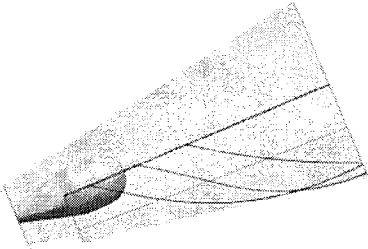
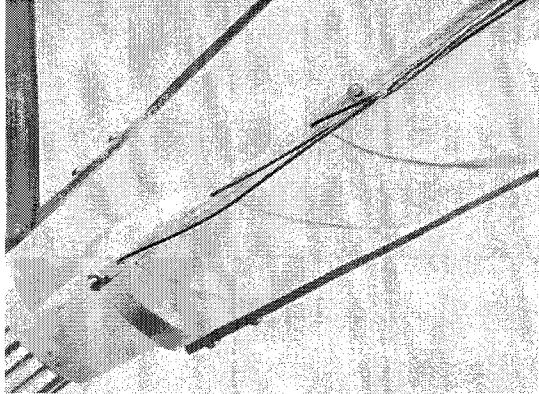
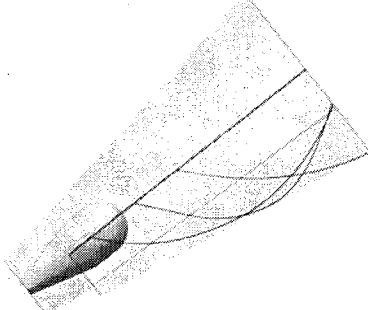
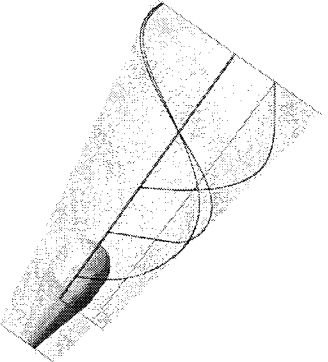
α	Exhaust Duct Model in Water Channel	Comments and CFD Results
30 deg.		<p>Flow from side intake remains attached to walls. The streamlines correspond well with the CFD results.</p> 
45 deg.		<p>Flow from side intake remains attached to walls. The most upstream streamline is disturbed by the flow over the brass side intake spacer. The remaining streamlines correspond well with the CFD results.</p> 
60 deg.		<p>Flow from side intake remains attached to walls. The streamlines correspond well with the CFD results.</p> 

Figure 3.44 Flow Visualization in Exhaust Duct Model with $w = 0.3 D_{REF}$ (Side)

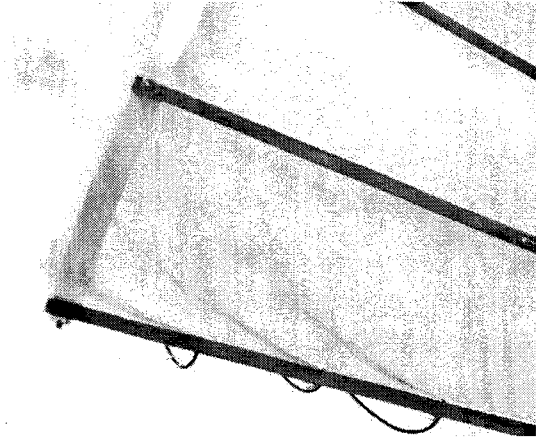
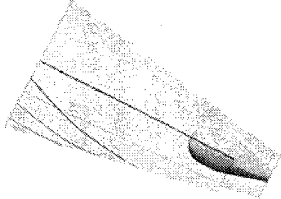
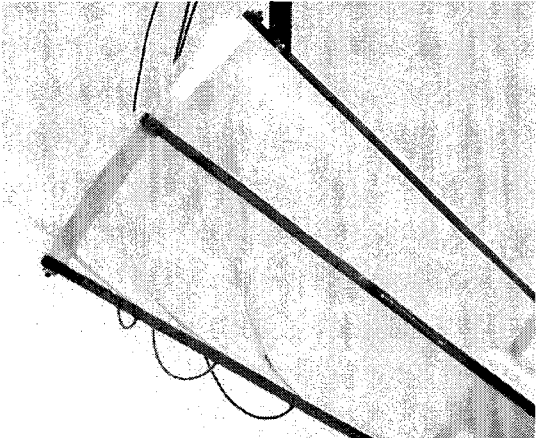
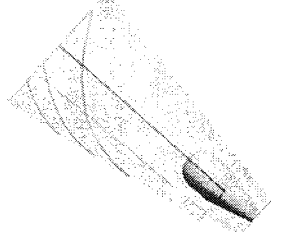
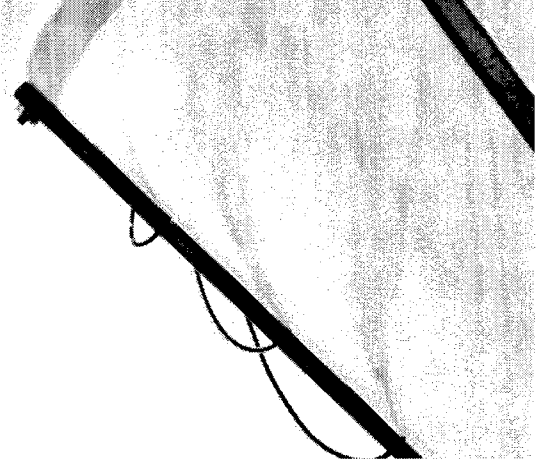
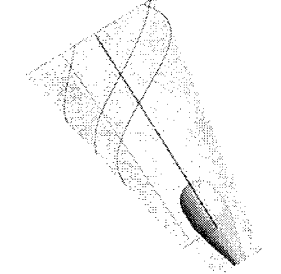
α	Exhaust Duct Model in Water Channel	Comments and CFD Results
30 deg.		<p>The flow from the side intake remains attached to the walls of the exhaust duct, but the trajectory of the flow causes it to reach the axial discharge plane before travelling very far around the circumference of the exhaust duct.</p> 
45 deg.		<p>The flow from the side intake remains attached to the walls of the exhaust duct, and the trajectory of the flow causes it to travel farther around the exhaust duct circumference before reaching the axial discharge plane.</p> 
60 deg.		<p>The flow from the side intake remains attached to the walls of the exhaust duct, and the trajectory of the flow causes it to travel around more than three-quarters of the exhaust duct circumference before reaching the axial discharge plane. The diffusion of the dye is clearly shown in this photograph.</p> 

Figure 3.45 Flow Visualization in Exhaust Duct Model with $w = 0.3 D_{REF}$ (Bottom)

3.7.2.2 Exhaust Duct with Geometry for Reduced Performance

The flow visualization exercise was also performed with an exhaust duct geometry that the CFD simulations indicate is less effective at increasing pressure-recovery performance of the exhaust duct. The side intake width was reduced to $w = 0.1 D_{\text{REF}}$, and the remaining parameters defining the exhaust duct geometry were kept the same as the previous case ($L = 6.5 D_{\text{REF}}$, $D_{\text{IN}} = 1.25 D_{\text{REF}}$, $2\theta = 20 \text{ deg.}$). As previously mentioned, for $w < 0.15 D_{\text{REF}}$ there is a significant increase in the axial component of the flow from the side intake through shear force interaction with the flow from the axial intake. This increase in axial momentum reduces the distance that the flow from the side intake travels around the circumference of the exhaust duct before reaching the axial discharge plane.

Photographs of the flow through the exhaust duct model are shown in Figure 3.46, and are compared to the CFD predictions for the corresponding inclination angle. Photographs with the dye injected at the side intake are not included, since at that location the flow is very similar to the flow with the previous geometry.

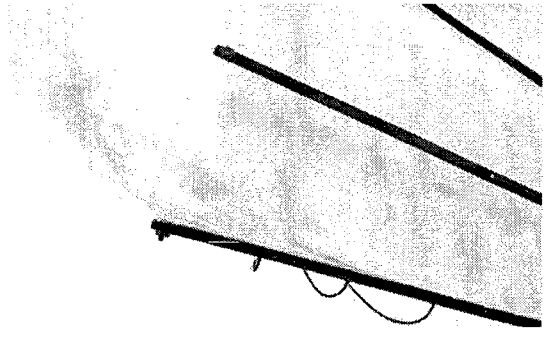
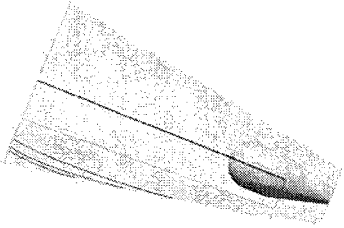
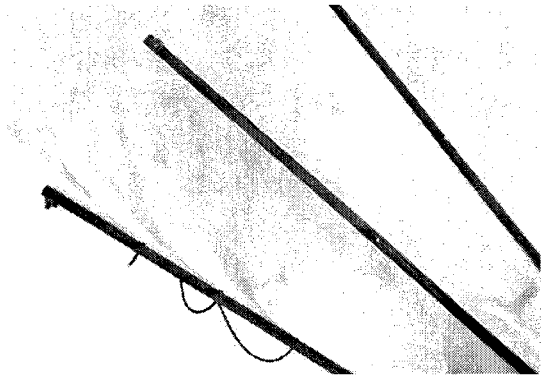
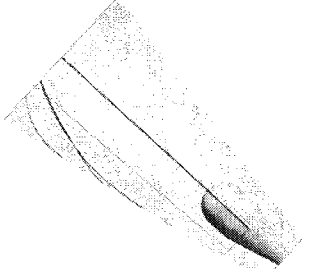
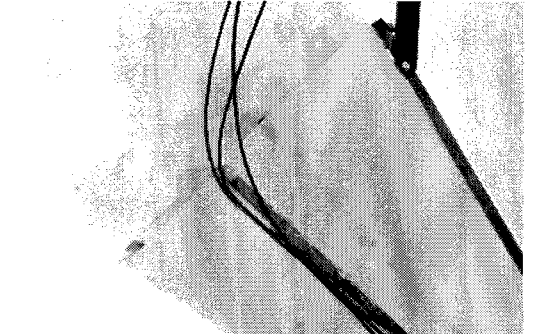
α	Exhaust Duct Model in Water Channel	Comments and CFD Results
30 deg.		<p>Higher axial momentum in the flow from the side intake results in the flow reaching the axial discharge plane before traveling very far around the circumference of the exhaust duct.</p> 
45 deg.		<p>Higher axial momentum in the flow from the side intake results in the flow reaching the axial discharge plane before traveling very far around the circumference of the exhaust duct. The axial flow along the exhaust duct walls is pulled into the recirculation zone RCZ 1 in the core of the exhaust duct.</p> 
60 deg.		<p>The dye injected into the flow separates from the wall and is pulled into the recirculation zone in the core of the exhaust duct. The dye is trapped there and builds up to form the cloud of dye shown in this photograph.</p>

Figure 3.46 Flow Visualization in Exhaust Duct Model with $w = 0.1 D_{REF}$

3.8 RECOMMENDATIONS AND FUTURE WORK

An exhaust duct geometry has been selected which has been shown to increase the pressure-recovery performance of the exhaust duct, but it is expected that the performance can be further improved if the recirculation zone (RCZ 1) can be reduced in size or eliminated. On the present exhaust duct geometry, the side intake starts one D_{REF} downstream of the axial intake. Extending the side intake upstream to the same plane as the axial intake may improve the pressure-recovery performance of the exhaust duct at a given inclination angle by allowing the flow from the side intake to travel farther around the circumference of the exhaust duct before reaching the axial discharge plane.

Before installing the Carleton Hydrokinetic Turbine in a river or tidal current, a study on the effects of the degradation of the wall surfaces in a marine environment on the pressure-recovery performance of the exhaust duct should be completed. If the performance of the exhaust duct is highly sensitive to wall roughness, extra research on a material or coating that resists the growth of underwater organisms would be required.

3.9 SUMMARY OF PRESSURE-RECOVERY PERFORMANCE OF EXHAUST DUCT

The geometry that is proposed as a starting point for further geometric refinement of the exhaust duct of the Carleton Hydrokinetic Turbine has an opening angle (2θ) of 20 deg., an exhaust duct length (L) of $6.5 D_{REF}$, an axial intake diameter (D_{IN}) of $1.25 D_{REF}$, and a side-intake width (w) of $0.3 D_{REF}$. This geometry has been shown to increase the mass flow rate through the turbine rotor by 7 to 26% for inclination angles (α) varying from 30 deg. to 70 deg. Refinement of the geometry is expected to further increase the

pressure-recover performance of the exhaust duct, but the current study was successful in demonstrating that the addition of tangential flow from the side intake is a feasible means of controlling the boundary layer and increasing the mass flow rate through the turbine rotor of the Carleton Hydrokinetic Turbine. Dye-injected streamlines through a model of the exhaust duct in a water channel facility corroborated the CFD predictions of the flow field through the exhaust duct.

4 CONCLUSIONS

The two design projects presented in this thesis successfully combine numerical predictions of fluid flows with experimental data to develop a low-speed, low-turbulence wind tunnel and evaluate the pressure-recovery performance of the exhaust duct of the Carleton Hydrokinetic Turbine. Furthermore, the numerical work in this thesis presents a useful study on the capabilities of the SST and RNG k - ϵ turbulence models in predicting flows influenced by pressure gradients and streamline curvature.

The low-speed wind tunnel was designed to offer a spatially uniform and low-turbulence testing environment for a velocity range not offered by the current experimental facilities at Carleton University. A unique feature of this wind tunnel is its modular design, which allows it to be efficiently and reversibly disassembled, moved and reassembled. Wall contours defined using Morel's equations and a contraction length of 2.13 m (84 in.) were shown using CFD simulations to provide uniform and low-turbulence flow into the test section. During the commissioning of the wind tunnel, it was necessary to add a flow-conditioning screen upstream of the contraction inlet to dampen unsteady flow motions from the laboratory environment. The average velocity at the inlet of the test section remains within $\pm 1.5\%$ of the centerline velocity over a range of operating conditions. The proximity of each side of the wind tunnel inlet to the laboratory walls does not affect the uniformity of the flow entering the test section, provided that the distances from each side of the inlet to the walls are within 0.1 m of each other when the average distance between the wind tunnel inlet and the walls is 0.3 m. The measured boundary layer displacement thickness at the test section inlet is 2.0 mm for a text section

velocity of 5 m/s, and has a boundary-layer shape factor indicating that the flow is attached as it enters the test section. Despite the absence of turbulence-reducing screens at the contraction inlet, a turbulence intensity of 0.24% was achieved for a test section velocity of 1.65 m/s. A traverse system was designed to provide a completely functional wind tunnel facility, and is capable of moving a probe through the volume of the test section with a positioning resolution of 0.173 mm in the streamwise direction and 0.0127 mm in the spanwise and vertical directions.

The flow through the exhaust duct of the Carleton Hydrokinetic Turbine was evaluated using CFD for the purpose of showing that the exhaust duct geometry is capable of increasing the mass flow rate through the turbine assembly over a range of operating conditions. A turbulence model validation study indicates that the SST and RNG k - ϵ turbulence models are equally capable of modeling flows influenced by both pressure gradients and significant streamline curvature. The SST model was selected to model the flow through the exhaust duct of the Carleton Hydrokinetic Turbine because the ANSYS CFX CFD software uses a low-Reynolds-number formulation with the SST model to simulate the boundary layer. The CFD simulation results predict that the addition of the exhaust duct to a bulb-turbine unit in a typical river or tidal current increases the mass flow rate across the turbine assembly by 7% to 26%, for inclination angles varying from 30 deg. to 70 deg. The momentum of the flow from the side intake was shown to be a critical factor in influencing the pressure-recovery performance of the exhaust duct. The final geometry selected for further evaluation of the Carleton Hydrokinetic Turbine has an opening angle of 20 deg., an exhaust duct length of 6.5

D_{REF} , an axial intake diameter of $1.25 D_{REF}$, and a side-intake width of $0.3 D_{REF}$. The validity of the CFD results was confirmed using a scale model of the exhaust duct in a large-scale water channel facility, with water-soluble dye used to visualize the streamlines of the flow through the exhaust duct.

REFERENCES

ANSYS. (2009). ANSYS CFX Help Files, V. 12.0.

Bardina, J., Coakley, T., & Huang, P. (1997). *Turbulence Modeling, Validation, Testing and Development*. NASA Technical Memorandum, NASA, Ames Research Center.

Bell, J., & Mehta, R. (1989). Boundary-Layer Predictions for Small Low-Speed Contractions. *AIAA Journal* , 27 (3), pp. 372 - 374.

Bradshaw, P., & Mehta, R. (2003, September 8). Retrieved from Wind Tunnel Design: www-htgl.stanford.edu/bradshaw/tunnel/index.html

Bradshaw, P., & Mehta, R. (1979). Technical Notes: Design rules for small low speed wind tunnels. *Aeronautical Journal of the Royal Aeronautical Society* , pp. 443-449.

Canadian Hydrographic Services. (2009). Retrieved from Canadian Hydrographic Services: www.chs-shc.gc.ca

Chen, J., Fang, F., & Hong, C. (2001). Experimental and analytical evaluation of flow in a square-to-square wind tunnel contraction. *J. Wind Engineering and Industrial Aerodynamics* (89), pp. 247-262.

Cho, & Fletcher. (1991). Computation of turbulent conical diffuser flow using a non-orthogonal grid system. *Computers and Fluids* , 19, pp. 347 - 361.

Chue, S. (1975). Pressure Probes for Fluid Measurement. *Progress in Aerospace Sciences* , 16 (2), pp. 127-223.

Clausen, P. K. (1993). Measurements of a Swirling Turbulent Boundary Layer Developing in a Conical Diffuser. *Experimental Thermal and Fluid Science* , 6, pp. 48-59.

Garg, R., & al, e. (1997). Some features of modeling spectral characteristics of flow in boundary layer wind tunnels. *Wind Engineering and Industrial Aerodynamics* , 72, pp. 1-12.

Gersten, K., & Schlichting, H. (2004). *Boundary Layer Theory* (8th Edition ed.). USA: Springer.

Grosvenor, A. (2000). *Numerical Simulations of Diffusing S-Duct and Vortex-Generator Jet Flows*. Masters Thesis, Carleton University, Mechanical and Aerospace Engineering, Ottawa.

Gupta, A., & Kumar, R. (2007). Three-dimensional turbulent swirling flow in a cylinder: Experiments and computations. *J. Heat and Fluid Flow* , 28, pp. 249-261.

- Gyllenram, W., & Nilsson, H. (2004). Numerical Investigations of Swirling Flow in a Conical Diffuser. *22nd IAHR Symposium on Hydraulic Machinery and Systems*. Stockholm, Sweden.
- Jawarneh. (2007). Strongly swirling flows in a cylindrical separator. *J. Minerals Engineering* , 21, pp. 366-372.
- Kundu, P., & Cohen, I. (2004). *Fluid Mechanics* (3rd ed.). San Diego, California, USA: Elsevier Academic Press.
- Mahalakshmi, N. V., Krithiga, G., Sandhya, S., Vikraman, J., & Ganesan, V. (2007). Experimental investigations of flow through conical diffusers with and without wake type velocity distortions at inlet. *J. Experimental Thermal and Fluid Science* , 32, pp. 133-157.
- Martin, A., & Thiele, F. (2004). Investigation of Flow Separation and Transition to Turbulence in an Axisymmetric Diffuser. *42nd AIAA Aerospace Sciences Meeting and Exhibit*. Nevada.
- Mattos, B. (2003). Design of ITA's Research Wind Tunnel Contraction Using CFD Tools. *21st Applied Aerodynamics Conference*. AIAA.
- Menter, F. (1994). Two-equation eddy-viscosity turbulence models for engineering applications. *AIAA* , 32 (8), pp. 1598-1605.
- Mikhail, M., & Rainbird, W. (1979). Optimum Design of Wind Tunnel Contractions. *AIAA Journal* , 23 (9), pp. 471-477.
- Morel, T. (1975). Comprehensive Design of Axisymmetric Wind Tunnel Contractions. *J. Fluids Engineering* , 225-233.
- National Research Council. (2009, 10 29). *NRC Institute for Aerospace Research Facilities*. Retrieved 10 29, 2009, from www.nrc-cnrc.gc.ca
- Nikjoo, M., & Mongia, H. (1999). Predictions of Flows with Adverse Pressure Gradients. *35th AIAA/ASME/SAE/ASEE Joint Propulsion Conference and Exhibit*. Los Angeles, California: AIAA.
- Nishi, A., & al, e. (1997). Turbulence control in multiple-fan wind tunnel. *Wind Engineering and Industrial Aerodynamics* , 67 & 68, pp. 861 - 872.
- Patel, V. R. (1984). Turbulence MOdesl for Near-Wall and Low Reynolds Number FLOws: A Review. *AAIA Journal* , 23, pp. 1308-1318.
- Pordal, H. e. (1993). Pressure Flux-split Viscous Solutions for Swirl Diffusers. *Computers Fluids* , 22 (4/5), pp. 663-683.
- Roach, P. (1994). Perspective: A Method for Uniform Reporting of Grid Refinement Studies. *J. Fluids Engineering* , 116, pp. 405-413.

- Saleh, J. (2002). *Fluid Flow Handbook*. New York, USA: McGraw-Hill.
- Senoo, Y., & Nishi, M. (1974). Improvement of the performance of conical diffusers by vortex generators. *J. Fluids Engineering* , 98, pp. 4-10.
- Sjolander. (2008). Turbomachinery Notes. Ottawa, Ontario, Canada: Carleton University.
- Sparrow, E., Abraham, J., & Minkowycz, W. (2009). Flow separation in a conical duct: Effect of Reynolds number and divergence angle. *Int. J. Heat and Mass Transfer* , 52, pp. 3079 - 3083.
- Su, Y. (1991). Flow Analysis and Design of Three-Dimensional Wind Tunnel Contractions. *AIAA* , 29 (11), pp. 1912-1920.
- Technology, D. U. (2009). *TU Delft Low-Speed Wind Tunnels*. Retrieved 10 29, 2009, from TU Delft: www.lr.tudelft.nl
- Tulapurkara, E., & Bhalla, V. (1988). Experimental Investigation of Morel's Method for Wind Tunnel Contractions. *ASME Journal of Fluid Engineering* , 110, pp. 45-47.
- University of Washington. (2009). *University of Washington Aeronautical Laboratory*. Retrieved 10 28, 2009, from www.aawashington.edu/uwal/
- Yakhot, V. e. (1992). Development of turbulence models for shear flows by a double expansion technique. *Physics of Fluids* , 4 (7), pp. 1510-1520.
- Yaras, M., & Golriz, M. (2006). *Patent No. 2544108*. Canada.

Appendix A. WIND TUNNEL THREE-VIEW DRAWINGS

All dimensions in the following figures are in meters.

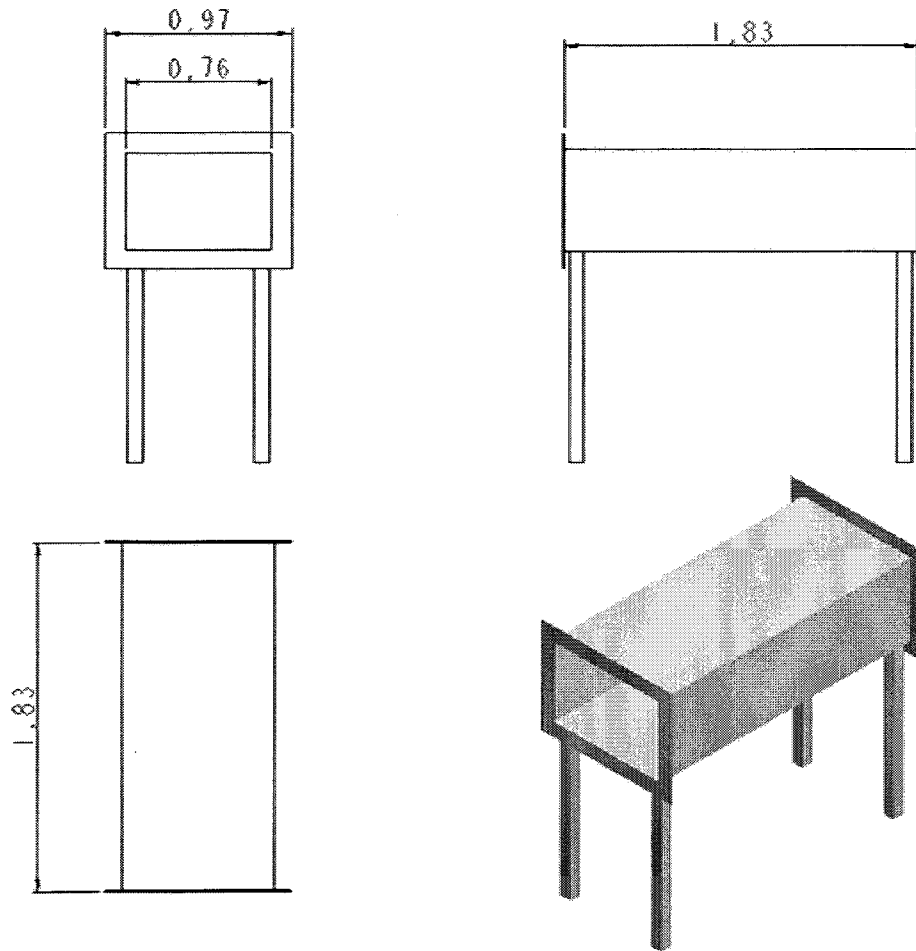


Figure A.1 Three-View Drawing of Wind Tunnel Test Section

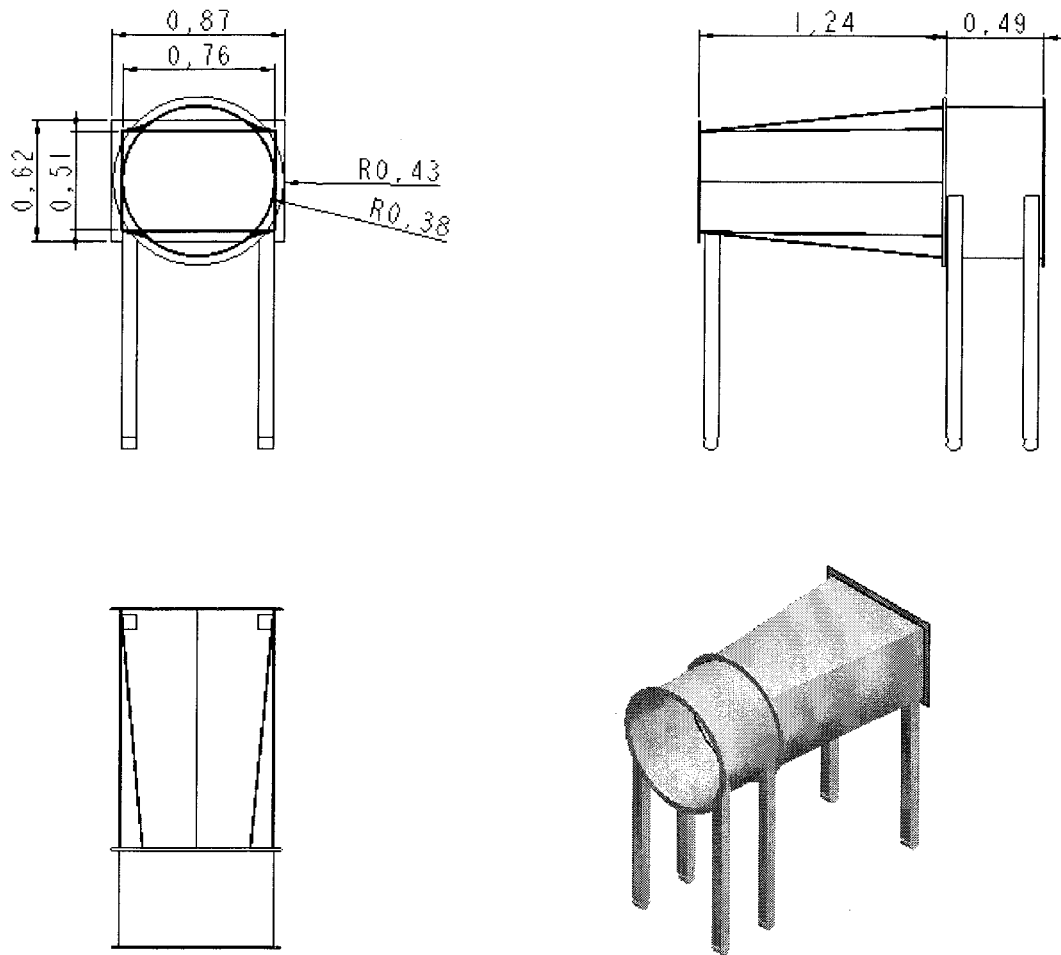


Figure A.2 Three-View Drawing of Wind Tunnel Transition Duct and Fan Module

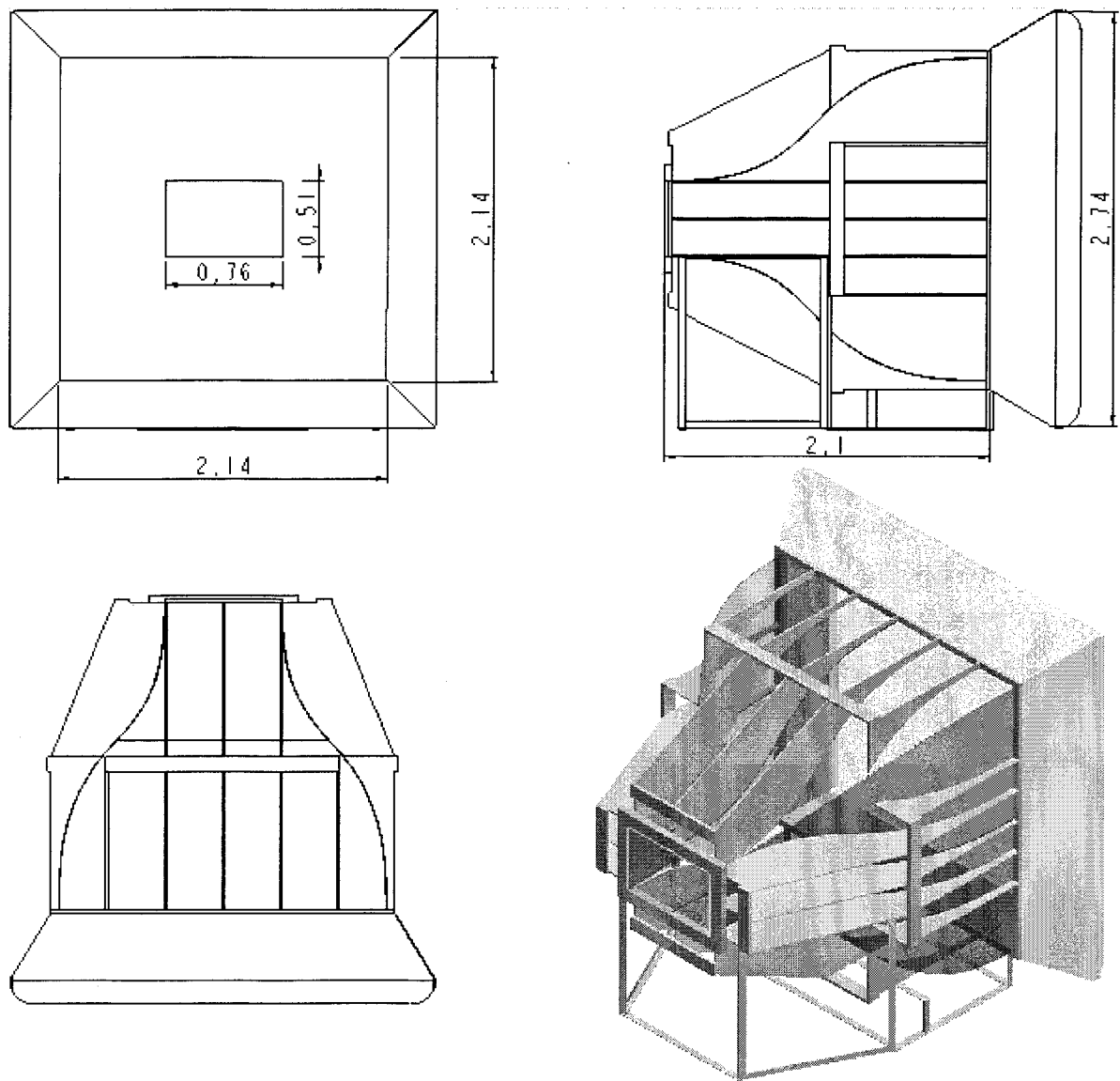


Figure A.3 Three-View Drawing of Wind Tunnel Contraction and Inlet

Appendix B. WIND TUNNEL FAN INFORMATION



Daltec Industries Ltd.

465 Laird Rd., Guelph, Ontario, Canada, N1G 4W1
 Ph: (519) 837-1921 Fax: (519) 837-2380
 Toll Free: 888-3DALTEC e-mail: faninfo@daltecfans.com

Fan Code: 630/255/6/18

Requirements

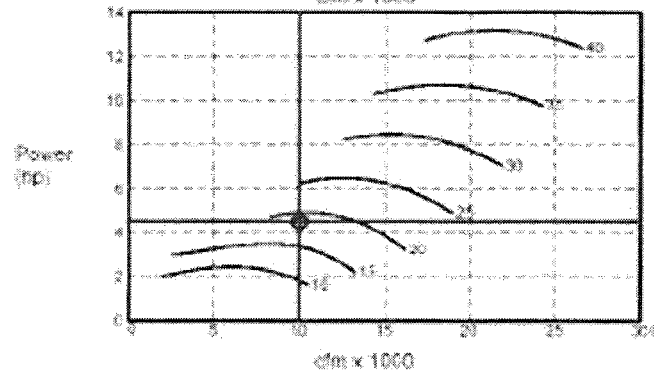
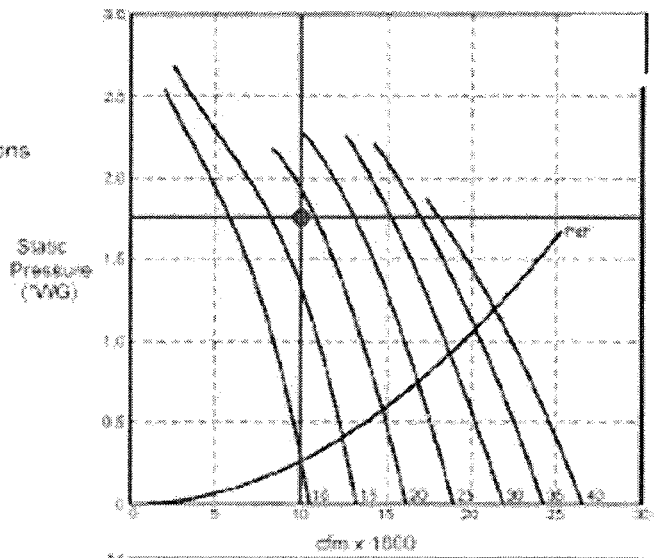
Volume: 10000 cfm
 Static Pressure: 1.75 "WG
 Selection Pressure: 1.75 "WG at std conditions
 Installation Category: TYPE D
 Temperature: 70 deg F
 Altitude: 0 ft

Fan Data (at STP)

Type: Axial Impeller
 Diameter: 29.5 in
 Hub: 266 mm
 Impeller Blades: 6
 Pitch: 18 degrees
 Blade Material: Aluminium
 Speed: 1750 RPM
 Absorbed Power: 4.47 hp
 Peak Power: 4.48 hp
 Total Efficiency: 70 %

Motor Data (at STP)

Motor Type:
 Electrical Supply:
 Motor Frame/Power:
 Current FLC/Start:
 Motor Speed:



Density: 0.075 lb/ft³

Sound Power

Spectrum (Hz)	63	125	250	500	1K	2K	4K	8K	dBW	dBA @ 5ft
Outlet PWL (dB)	92	86	88	87	88	84	80	74	96	77
Inlet PWL (dB)	90	86	87	87	89	84	81	74	96	78

Note: Levels are quoted as in-duct values. dBA values are average spherical free-field for comparative use only.

Appendix C. WIND TUNNEL ASSEMBLY INSTRUCTIONS

The following instructions are a guide for assembling the wind tunnel. The test section, transition duct and fan modules do not require any modifications to fit through the doorway.

Table A.1 Wind Tunnel Assembly Instructions

Step	Procedure
1	Roll the test section, transition duct and fan into the laboratory and place appropriately.
2	Roll in the support structure for the contraction and bolt the uprights into place.
3	Place the bottom contraction wall on the support structure.
4	Place the side contraction walls and line them up with the bottom wall using dowel pins.
5	Check that the height of the contraction outlet matches the height of the test section inlet. If not, adjust the nuts on the support structure.
6	Place the top contraction wall and line it up with the side walls using dowel pins.
7	Place dowel pins in the holes at the contraction inlet and hang the flow-conditioning screen in place.
8	Roll in the steel inlet support structure.
9	Bring in the inlet wooden support structure one wall at a time and join them to the contraction inlet using the dowel pins and black straps.
10	Place each of the rounded inlet segments in place and aligned them to the support structure using dowel pins.
11	Tighten the rounded inlet segments to the contraction using the blue straps.

Appendix D. WIND TUNNEL DISASSEMBLY INSTRUCTIONS

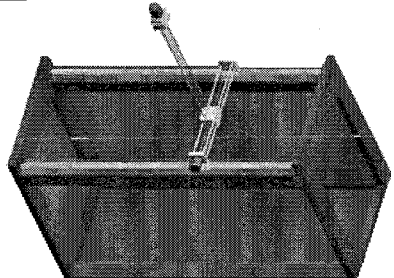
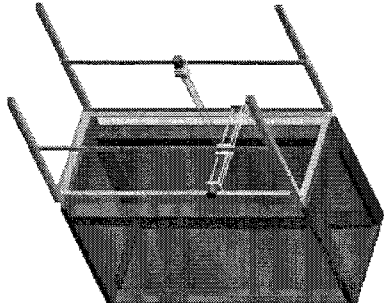
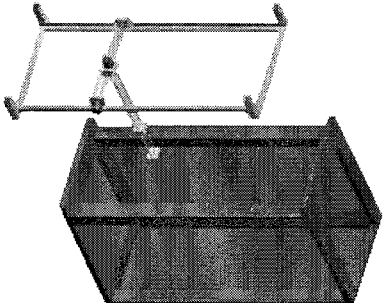
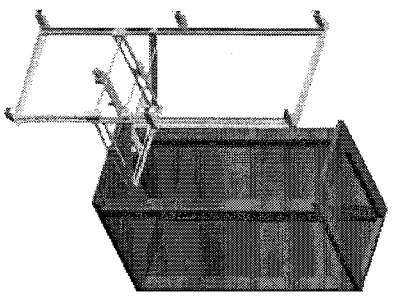
These instructions are a guide for disassembling the wind tunnel. The test section, transition duct and fan modules do not require any modifications to fit through the doorway.

Table A.2 Wind Tunnel Disassembly Instructions

Step	Procedure
1	Remove the transition duct and fan from the laboratory.
2	Turn the test section on its side and remove it from the laboratory.
3	Unhook the blue straps holding the rounded inlet to the contraction.
4	Remove each of the rounded inlet pieces from the dowel pins aligning them with the contraction and remove from laboratory.
5	Undo the black straps holding the inlet wooden support structure to the contraction and slide it out from the dowel pins aligning it with the contraction.
6	Remove the inlet wooden support structure walls one at a time from the laboratory.
9	Remove the steel inlet support structure from the laboratory.
10	Starting with the top wall of the contraction, remove it from the dowel pins connecting it to the side walls and remove it from the laboratory.
11	Remove the two side walls, and then the bottom wall of the contraction and removed them from the laboratory.
12	Unbolt the upright sections of the contraction support structure and remove the support structure from the laboratory.

Appendix E. TRAVERSE SYSTEM DESIGN ITERATIONS

Table A.3 Traverse System Design Iterations

#	ProE Image of Model	Comments
1		<ul style="list-style-type: none"> - minimal structure reduces weight and cost - interferes with access to test section - vertical motor support will likely vibrate and bend significantly - not transferable to different test sections that do not have a flat area to hold the rails
2		<ul style="list-style-type: none"> - high weight due to length of supports - interferes with access to test section - vertical motor support will likely vibrate and bend significantly - allows for transfer to different test facilities by mounting to ceiling
3		<ul style="list-style-type: none"> - less weight due to shorter vertical supports - allows open access to test section - vertical motor held rigidly, but support will still bend in streamwise direction - simple ceiling mount easy to reproduce over different test facilities
4		<ul style="list-style-type: none"> - less weight due to shorter vertical supports - allows open access to test section - includes reinforcements to minimize vibrations and bending - motor for motion in spanwise direction is between the top and bottom supports to reduce the likelihood of jamming - simple ceiling mount easy to reproduce for different test facilities

Design iteration #4 was selected as a base for the detailed design presented in Section 2.10.2.

Appendix F. PHOTOGRAPHS OF INSTALLED TRAVERSE SYSTEM

SYSTEM

The photographs below are of the traverse system installed in 3175 ME.

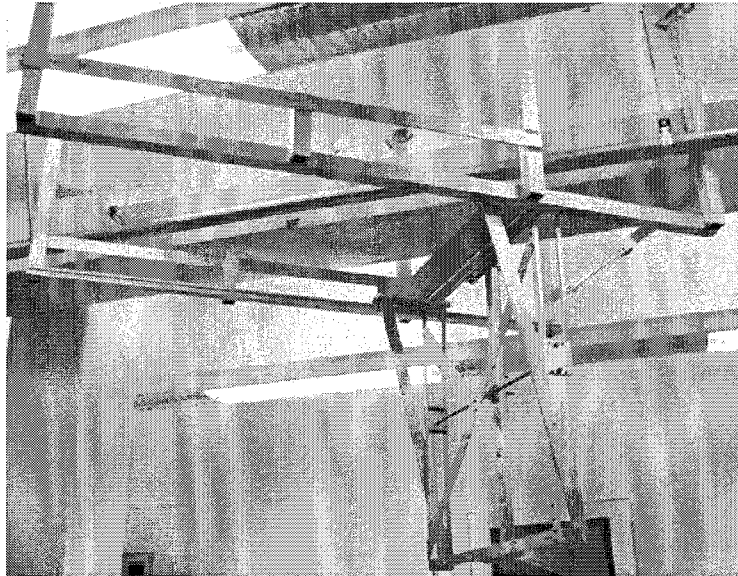


Figure A.4 Traverse System Installed in 3175 ME

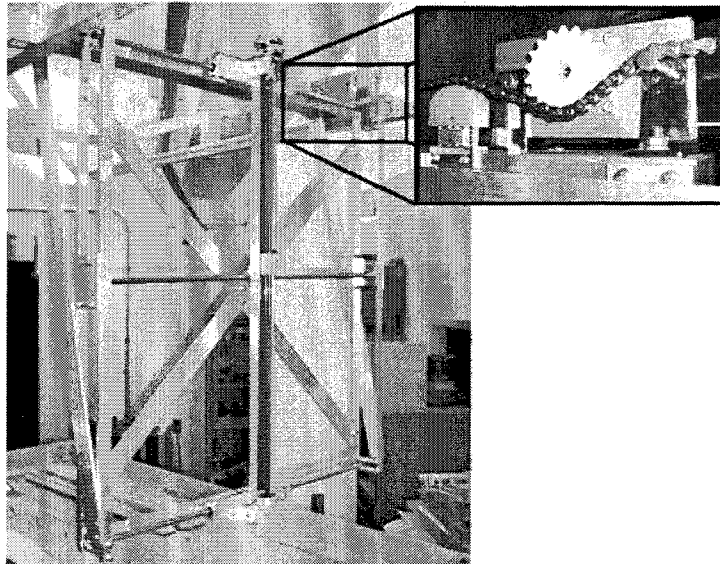


Figure A.5 Traverse System and Streamwise Motion Components Installed in 3175 ME

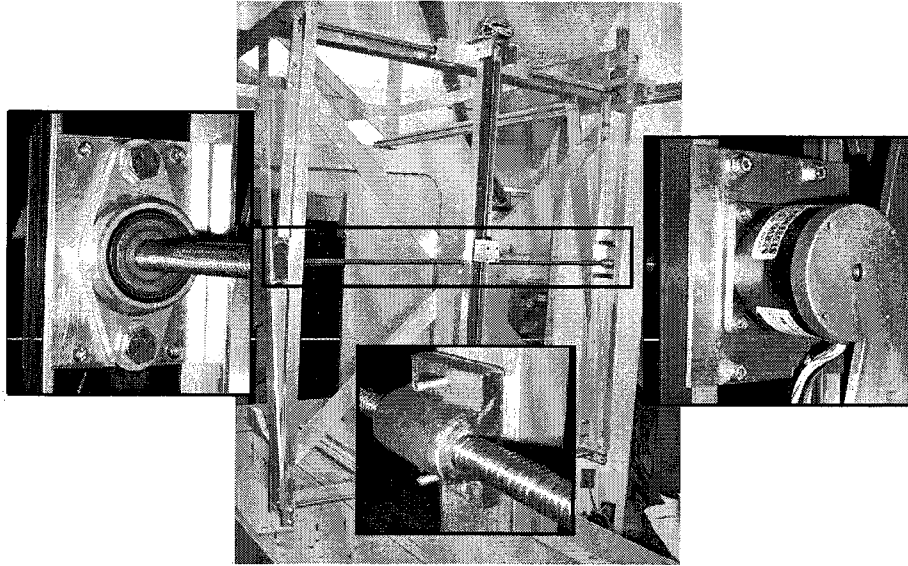


Figure A.6 Traverse System and Spanwise Motion Components Installed in 3175 ME

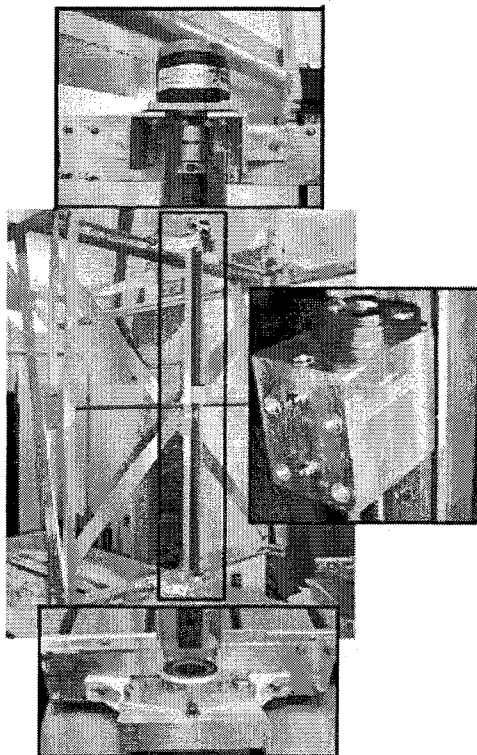


Figure A.7 Traverse System and Vertical Motion Components Installed in 3175 ME

Appendix G. OPERATION OF TRAVERSE SYSTEM

The traverse system step motors are connected to three motor controllers that are driven by a parallel port attached to a computer in 3175 ME. The wiring diagram for the system is shown in Figure A.8. The Matlab program to control the system was designed by Kyle Klumper, an undergraduate engineering student working on an NSERC URSA scholarship during the summer of 2009. The user interface he designed is shown in Figure A.9, along with the Matlab code.

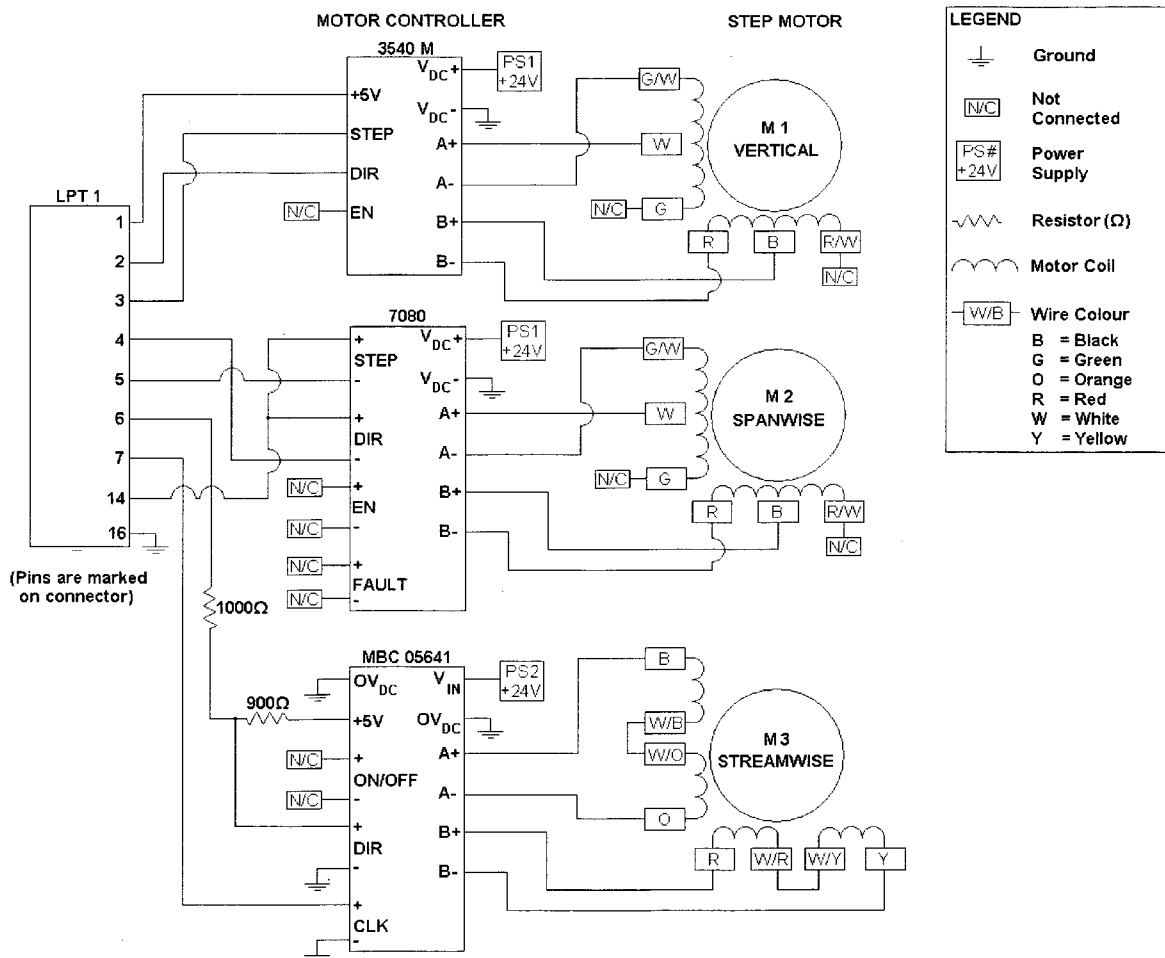


Figure A.8 Wiring Diagram for Traverse System

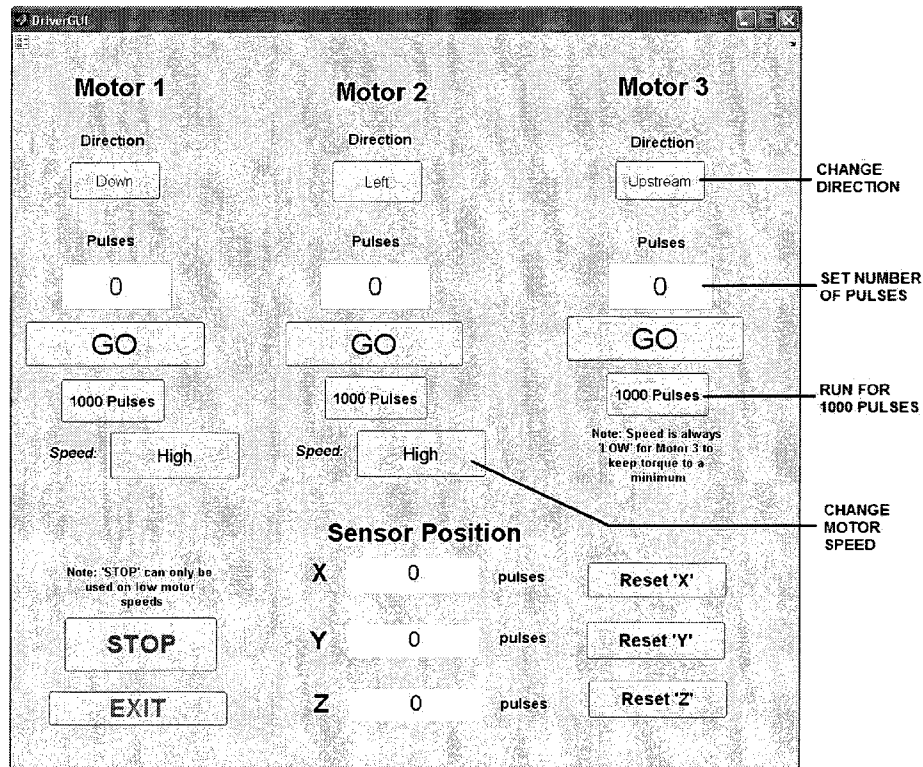


Figure A.9 Traverse System User Interface

MATLAB CODE

```
function varargout = DriverGUI(varargin)
    gui_Singleton = 1;
    gui_State = struct('gui_Name',    mfilename, ...
        'gui_Singleton', gui_Singleton, ...
        'gui_OpeningFcn', @DriverGUI_OpeningFcn, ...
        'gui_OutputFcn', @DriverGUI_OutputFcn, ...
        'gui_LayoutFcn', [] , ...
        'gui_Callback', []);
    if nargin && ischar(varargin{1})
        gui_State.gui_Callback = str2func(varargin{1});
    end
    if nargin
        [varargout{1:nargout}] = gui_mainfcn(gui_State, varargin{:});
    else
        gui_mainfcn(gui_State, varargin{:});
    end
end
```

```
function DriverGUI_OpeningFcn(hObject, eventdata, handles, varargin)
    output=digitalio('parallel','LPT1');
    dato=addline(output,0:7,0,'out');
    putvalue(dato,[0 0 0 0 0 0 0]);

    dato2=addline(output,0:3,2,'out');
    putvalue(dato2,[0 0 0 0]);
    handles.pulse1=0;
```

```

handles.pulse2=0;
handles.pulse3=0;

global abs_x abs_y abs_z stop_bit speed_bit_1 speed_bit_2
abs_x = 0;
abs_y = 0;
abs_z = 0;
stop_bit=0;
speed_bit_1=0;
speed_bit_2=0;
handles.output = hObject;
guidata(hObject, handles);

function varargout = DriverGUI_OutputFcn(hObject, eventdata, handles)
varargout{1} = handles.output;

function Direction1_Callback(hObject, eventdata, handles)
f=get(handles.Direction1,'Value');
if f==1
    set(handles.Direction1,'String','Up');
else
    set(handles.Direction1,'String','Down');
end
guidata(hObject, handles);

function Direction2_Callback(hObject, eventdata, handles)
f=get(handles.Direction2,'Value');
if f==1
    set(handles.Direction2,'String','Right');
else
    set(handles.Direction2,'String','Left');
end
guidata(hObject, handles);

function Direction3_Callback(hObject, eventdata, handles)
f=get(handles.Direction3,'Value');
if f==1
    set(handles.Direction3,'String','Downstream');
else
    set(handles.Direction3,'String','Upstream');
end
guidata(hObject, handles);

function edit1_Callback(hObject, eventdata, handles)
handles.pulse1=str2double(get(hObject,'String'));
guidata(hObject, handles);

function edit1_CreateFcn(hObject, eventdata, handles)
if ispc && isequal(get(hObject,'BackgroundColor'), get(0,'defaultUicontrolBackgroundColor'))
    set(hObject,'BackgroundColor','white');
end

function edit2_Callback(hObject, eventdata, handles)
handles.pulse2=str2double(get(hObject,'String'));
guidata(hObject, handles);

```

```
function edit2_CreateFcn(hObject, eventdata, handles)
    if ispc && isequal(get(hObject,'BackgroundColor'), get(0,'defaultUicontrolBackgroundColor'))
        set(hObject,'BackgroundColor','white');
    end
end
```

```
function edit3_Callback(hObject, eventdata, handles)
    handles.pulse3=str2double(get(hObject,'String'));
    guidata(hObject, handles);
end
```

```
function edit3_CreateFcn(hObject, eventdata, handles)
    if ispc && isequal(get(hObject,'BackgroundColor'), get(0,'defaultUicontrolBackgroundColor'))
        set(hObject,'BackgroundColor','white');
    end
end
```

```
function go1_Callback(hObject, eventdata, handles)
    set(handles.go1,'String','Running..');
    outport=digitalio('parallel','LPT1');
    dato=addline(outport,0:7,'out');
    e=get(handles.Direction1,'Value');
    putvalue(dato,[e 0 0 0 0 0 0]);
    dato2=addline(outport,0:3,2,'out');
    putvalue(dato2,[0 0 0 0]);
    global abs_x stop_bit speed_bit_1
    stop_bit=0;
    for x=handles.pulse1:-1:0
        if stop_bit==1
            break
        else
            putvalue(dato(2),1);
            pause(speed_bit_1)
            putvalue(dato(2),0);
            pause(speed_bit_1)
            if e==0
                xval = abs_x+handles.pulse1-x;
                set(handles.x_coord,'String',xval)
            else
                xval = abs_x-handles.pulse1+x;
                set(handles.x_coord,'String',xval)
            end
        end
    end
    abs_x=xval;
    set(handles.go1,'String','Go');
    guidata(hObject, handles);
end
```

```
function go2_Callback(hObject, eventdata, handles)
    set(handles.go2,'String','Running..');
    outport=digitalio('parallel','LPT1');
    dato=addline(outport,0:7,'out');
    e=get(handles.Direction2,'Value');
    putvalue(dato,[0 0 e 0 0 0 0]);

    dato2=addline(outport,0:3,2,'out');
    putvalue(dato2,[0 0 0 0]);
end
```

```

global abs_y stop_bit speed_bit_2
stop_bit=0;
for x=handles.pulse2:-1:0
    if stop_bit==1
        break
    else
        putvalue(dato(4),1);
        pause(speed_bit_2)
        putvalue(dato(4),0);
        pause(speed_bit_2)
        if e==0
            yval = handles.pulse2+abs_y-x;
            set(handles.y_coord,'String',yval)
        else
            yval = abs_y-handles.pulse2+x;
            set(handles.y_coord,'String',yval)
        end
    end
end
abs_y=yval;
set(handles.go2,'String','Go');
guidata(hObject, handles);

```

```

function go3_Callback(hObject, eventdata, handles)
set(handles.go3,'String','Running..');
outport=digitalio('parallel','LPT1');
dato=addline(outport,0:7,'out');
e=get(handles.Direction3,'Value');
putvalue(dato,[0 0 0 0 e 0 0 1]);
dato2=addline(outport,0:3,2,'out');
putvalue(dato2,[0 0 0 0]);

```

```

global abs_z stop_bit
stop_bit=0;
for x=handles.pulse3:-1:0
    if stop_bit==1
        break
    else
        putvalue(dato(6),1);
        pause(0.01)
        putvalue(dato(6),0);
        pause(0.01)
        if e==0
            zval = handles.pulse3+abs_z-x;
            set(handles.z_coord,'String',zval)
        else
            zval = abs_z-handles.pulse3+x;
            set(handles.z_coord,'String',zval)
        end
    end
end
abs_z=zval;
set(handles.go3,'String','Go');
guidata(hObject, handles);

```

```

function pulses1_Callback(hObject, eventdata, handles)
    set(handles.pulses1,'String','Running..');
    f = get(handles.pulses1,'Value');
    outputport=digitalio('parallel','LPT1');
    dato=addline(outputport,0:7,'out');
    e=get(handles.Direction1,'Value');
    putvalue(dato,[e 0 0 0 0 0 0]);
    dato2=addline(outputport,0:3,2,'out');
    putvalue(dato2,[0 0 0 0]);
    global abs_x stop_bit speed_bit_1
    stop_bit=0;
    for x=1000:-1:0
        if stop_bit==1
            break
        else
            putvalue(dato(2),1);
            pause(speed_bit_1)
            putvalue(dato(2),0);
            pause(speed_bit_1)
            if e==0
                xval = abs_x+1000-x;
                set(handles.x_coord,'String',xval)
            else
                xval = abs_x-1000+x;
                set(handles.x_coord,'String',xval)
            end
        end
    end
    abs_x = xval;
    set(handles.pulses1,'String','1000 Pulses');
    guidata(hObject, handles);

```

```

function pulses2_Callback(hObject, eventdata, handles)
    set(handles.pulses2,'String','Running..');
    outputport=digitalio('parallel','LPT1');
    dato=addline(outputport,0:7,'out');
    e=get(handles.Direction2,'Value');
    putvalue(dato,[0 0 e 0 0 0 0]);
    dato2=addline(outputport,0:3,2,'out');
    putvalue(dato2,[0 0 0 0]);
    global abs_y stop_bit speed_bit_2
    stop_bit=0;
    for x=1000:-1:0
        if stop_bit==1
            break
        else
            putvalue(dato(4),1);
            pause(speed_bit_2)
            putvalue(dato(4),0);
            pause(speed_bit_2)
            if e==0
                yval = 1000+abs_y-x;
                set(handles.y_coord,'String',yval)
            else
                yval = abs_y-1000+x;
                set(handles.y_coord,'String',yval)
            end
        end
    end

```

```

        end
    end
end
abs_y = yval;
set(handles.pulses2,'String','1000 Pulses');
guidata(hObject, handles);

function pulses3_Callback(hObject, eventdata, handles)
set(handles.pulses3,'String','Running..');
outport=digitalio('parallel','LPT1');
dato=addline(outport,0:7,'out');
e=get(handles.Direction3,'Value');
putvalue(dato,[0 0 0 0 e 0 0 0]);
dato2=addline(outport,0:3,2,'out');
putvalue(dato2,[0 0 0 0]);
global abs_z stop_bit
stop_bit=0;
for x=1000:-1:0
    if stop_bit==1
        break
    else
        putvalue(dato(6),1);
        pause(0.01)
        putvalue(dato(6),0);
        pause(0.01)
        if e==0
            zval = 1000+abs_z-x;
            set(handles.z_coord,'String',zval)
        else
            zval = abs_z-1000+x;
            set(handles.z_coord,'String',zval)
        end
    end
end
abs_z = zval;
set(handles.pulses3,'String','1000 Pulses');
guidata(hObject, handles);

function exit_Callback(hObject, eventdata, handles)
delete(gcf)
guidata(hObject, handles);

function reset_x_Callback(hObject, eventdata, handles)
global abs_x
abs_x = 0;
set(handles.x_coord,'String',abs_x)
guidata(hObject, handles);

function reset_y_Callback(hObject, eventdata, handles)
global abs_y
abs_y = 0;
set(handles.y_coord,'String',abs_y)
guidata(hObject, handles);

function reset_z_Callback(hObject, eventdata, handles)

```

```
global abs_z
abs_z = 0;
set(handles.z_coord,'String',abs_z)
guidata(hObject, handles);
```

```
function stop_Callback(hObject, eventdata, handles)
global stop_bit
stop_bit = 1;
guidata(hObject, handles);
```

```
function speed_1_Callback(hObject, eventdata, handles)
global speed_bit_1
f=get(handles.speed_1,'Value');
if f==1
    set(handles.speed_1,'String','Low');
    speed_bit_1=0.01;
else
    set(handles.speed_1,'String','High');
    speed_bit_1=0;
end
guidata(hObject, handles);
```

```
function speed_2_Callback(hObject, eventdata, handles)
global speed_bit_2
f=get(handles.speed_2,'Value');
if f==1
    set(handles.speed_2,'String','Low');
    speed_bit_2=0.01;
else
    set(handles.speed_2,'String','High');
    speed_bit_2=0;
end
guidata(hObject, handles);
```

Appendix H. WIND TUNNEL COST REPORT

The following table shows the cost in Canadian dollars for the materials to build the wind tunnel contraction and inlet.

Table A.4 Wind Tunnel Contraction Costs

Company	Material	Price/unit	Total (with tax)
Home Depot	9 – Plywood sheets 4ftx8ftx¼" 4 – 1"x4"x8ft pine 9 – 2"x4"x8ft pine 8 – 2"x6"x8ft pine 1 – 4ftx8ft hardboard 1 – Small paint brushes/rollers 1 – Locking tie down straps 2 – 50 Brackets ¾"x2 ½" Delivery	\$17.47 \$1.76 \$2.50 \$3.79 \$16.50 \$13.82 \$14.95 \$11.69 \$60.00	\$394.16
Loucon Metal Limited	3 – 20ft steel angles 2"x2"x¼" 1 – 10ft steel angles 2"x2"x¼" 1 – 20ft steel flats 2"x¼" 1 – 10ft steel flats 2"x¼"	\$41.58 \$22.79 \$23.64 \$13.82	\$210.89
CANUS Plastics	8 – Acrylic sheet 4ftx8ftx3mm Delivery	\$79.96 \$35.00	\$769.13
McMaster-Carr	2 – 3” threaded stem castor 2 – 3” threaded stem castor with brake 2 – 4” threaded stem castor 2 – 4” threaded stem castor with brake 8 – Nylon strap hooks 1 – ¼" x 2 ½" dowel pins pack of 25 Plus delivery and conversion to \$CA	\$9.77 \$11.11 \$12.49 \$13.67 \$6.80 \$9.65	\$199.83
Canadian Tire	1- Edge trim 3 - Castors Painting supplies 1 - Mending plates	\$14.99 \$3.09 \$113.71 \$2.79	\$160.47
Carleton Bookstore	Fine tipped non-permanent marker	\$1.99	\$2.27
Givesco Inc.	4 – 12"x10ft builder tubes Delivery	\$24.96 \$15.00	\$130.92
		TOTAL	\$1867.67

The following table shows the costs in Canadian dollars for the materials to build the wind tunnel traverse system.

Table A.5 Wind Tunnel Traverse System Costs

Company	Material	Price/unit	Total (with tax)
Home Depot	Metal cleaner	\$7.79	\$44.08
	Padlock for water channel	\$5.98	
	Stainless steel screws/bolts	\$25.06	
Loucon Metal Limited	2 – 2" x 0.25" x 20 ft. Al. flat	\$43.20	\$470.97
	2 – 2" x 2" 0.25" x 21 ft. Al. angle	\$86.17	
	1 – 2" x 2" x 20 ft. Al. square	\$158.05	
McMaster-Carr	2 – Precision shaft	\$140.81	\$2985.36
	2 – Rail shaft support	\$65.90	
	4 – Linear ball bearings	\$86.42	
	1 – Plain bearing rails	\$109.19	
	1 – Plain bearing guide block	\$32.86	
	2 – Stainless steel threaded rods	\$97.08	
	1 – 40 in. guide rail	\$109.09	
	1 – Sleeve bearing	\$2.54	
	1 – Loctite	\$11.24	
	2 – Shaft coupling	\$14.30	
	2 – Shaft collars	\$2.09	
	4 – Railings	\$29.00	
	2 – Small single flange guide block	\$48.46	
	2 – Large single flange guide block	\$61.61	
	1 – Sprocket	\$12.44	
	2 – Roller chain	\$89.88	
	1 – Chain tensioner	\$41.77	
	1 – Shaft reducer bushing	\$6.90	
	8 – Rail end caps	\$2.67	
	1 – Track (8ft + 6 ft)	\$53.70	
	1 – Track center bracket	\$9.11	
	4 – Track end stops	\$12.05	
	4 – Track hangers	\$13.10	
	1 – Pulley	\$26.90	
	1 – Rope & rope ends	\$16.82	
	4 – Eye bolts	\$6.22	
	5 – Rope guides	\$1.67	
	1 – Rope cleat	\$4.59	
	Screws, nuts and assorted aluminum (includes flats, angles, blocks)	\$885.83	
	TOTAL		\$3500.41

Appendix I. WIND TUNNEL BOUNDARY LAYER PROFILES

The boundary layer profiles were measured both with and without the flow-conditioning screen installed for three different wind tunnel speeds, as shown in Figure A.11 and Figure A.10. When the flow-conditioning screen was removed, the average fluctuations in the boundary layer due to unsteadiness in the flow through the wind tunnel laboratory varied from 11% to 33% of the centerline velocity. With the flow-conditioning screen installed, the average fluctuations in the boundary layer were reduced to 0% to 2% of the centerline velocity. These results clearly show the need for the flow-conditioning screen to dampen unsteady flow motion in the laboratory environment. The profiles for the measured boundary layers are shown in the following figures, with the profiles offset by 0, 1 and 2 for clarity.

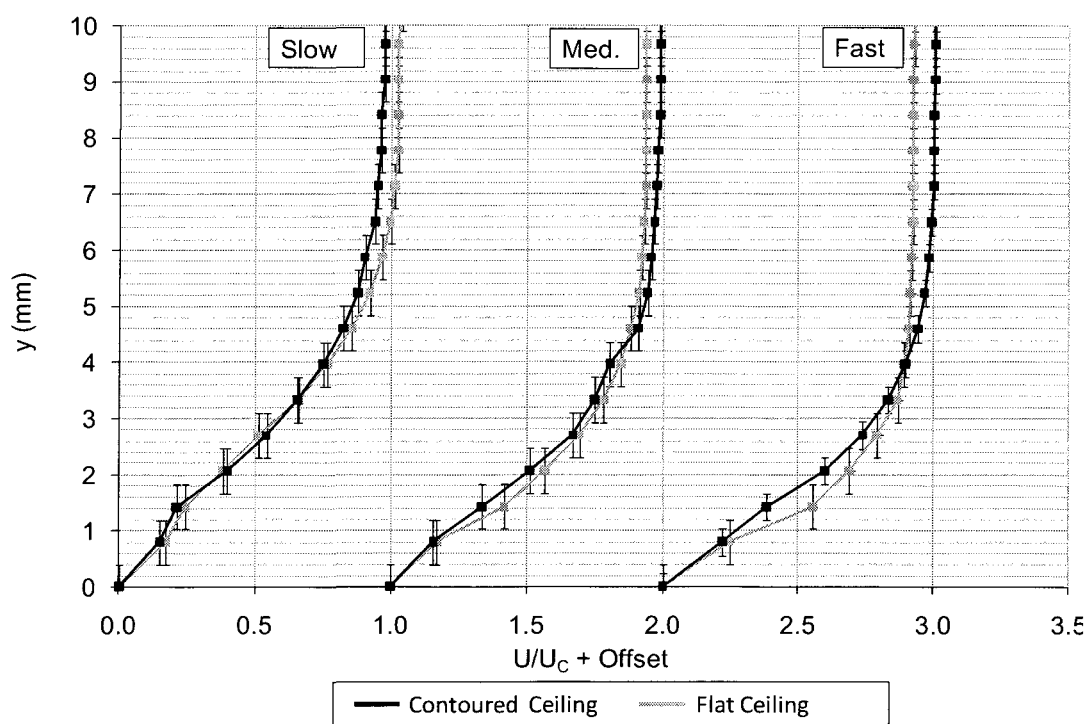


Figure A.10 Boundary Layer Profiles with Flow-Conditioning Screen

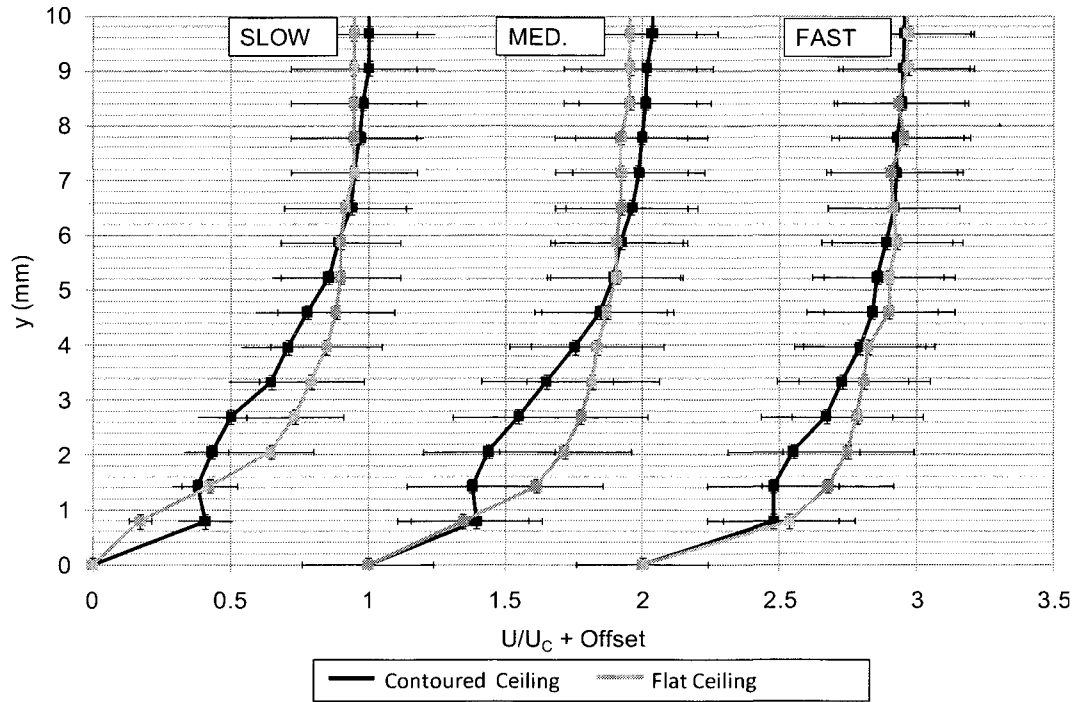
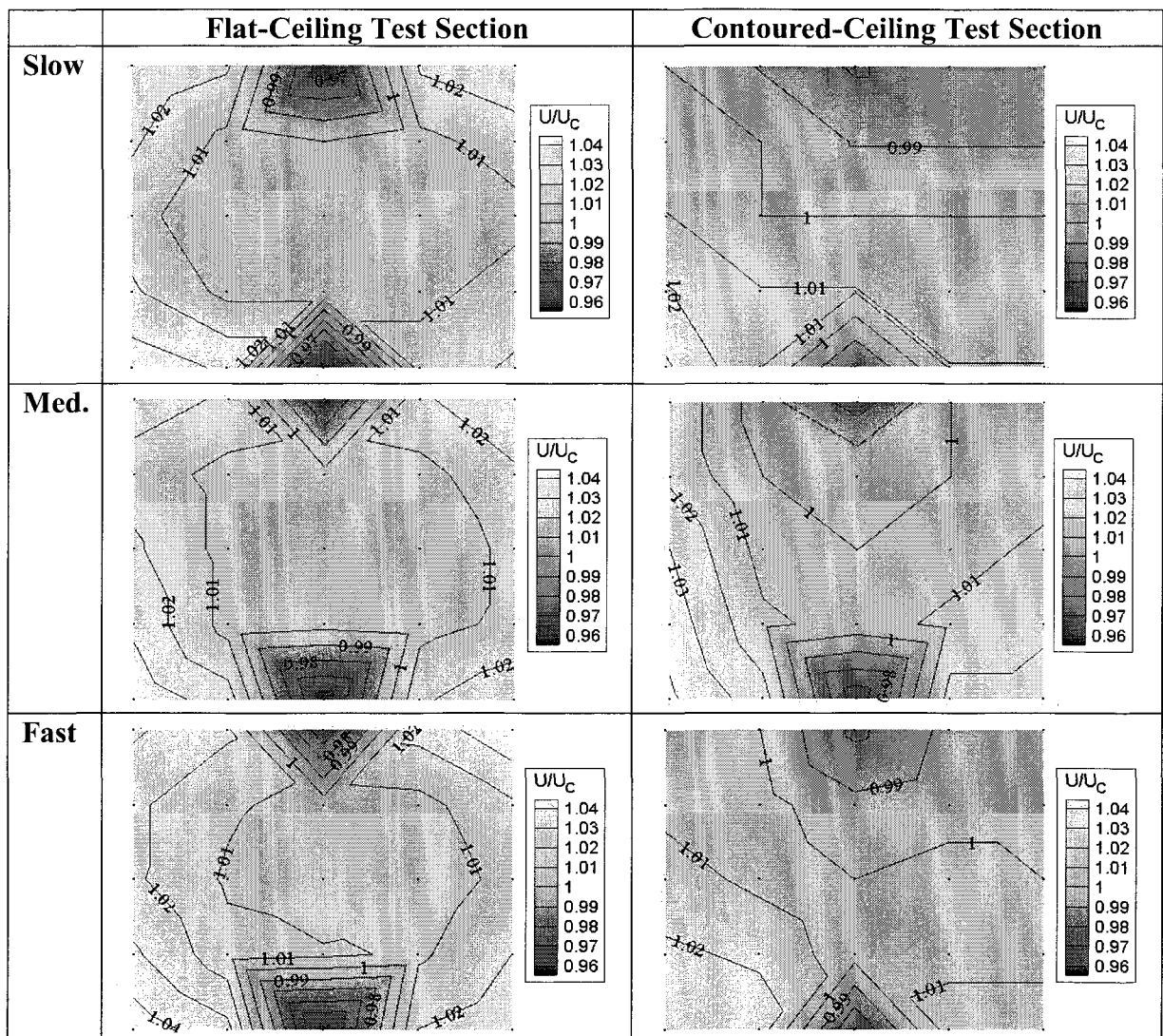


Figure A.11 Boundary Layer Profiles without Flow-Conditioning Screen

Appendix J. WIND TUNNEL MEAN-VELOCITY PLOTS

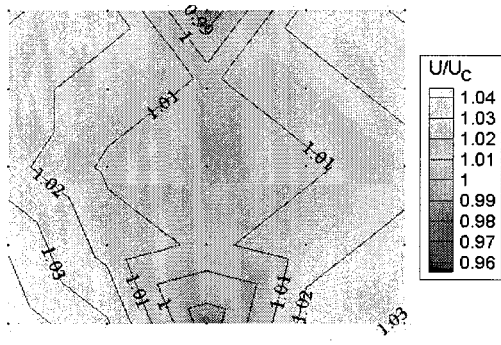
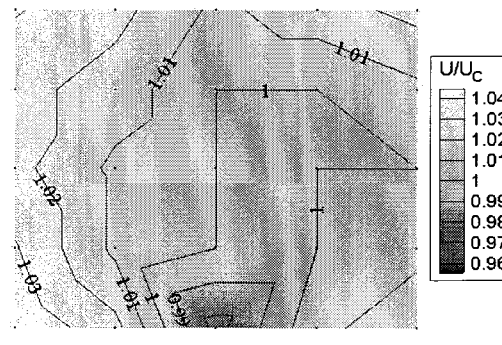
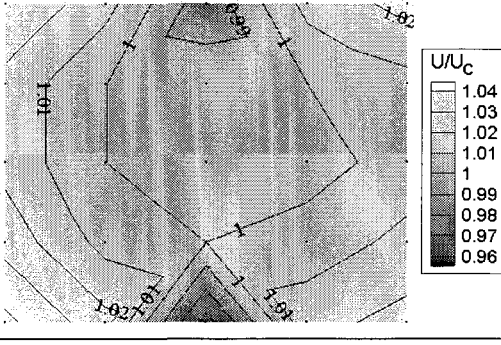
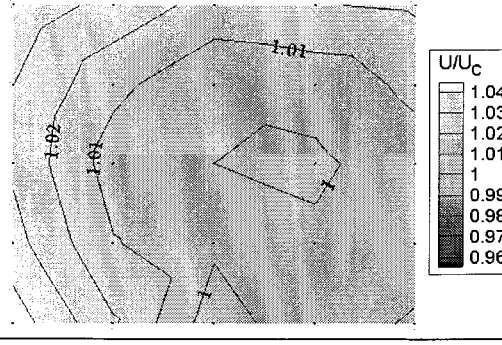
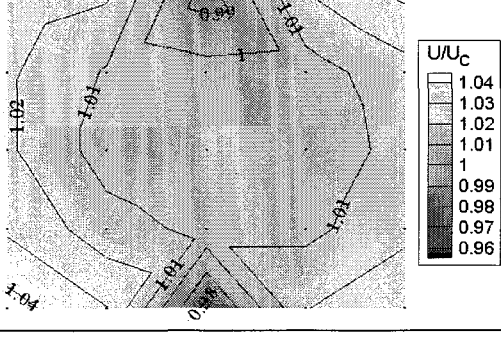
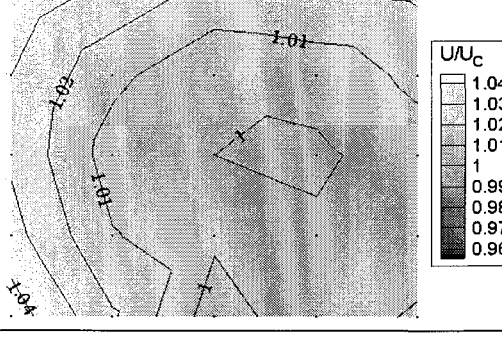
The spatial uniformity of the flow entering the test section was measured with the flow-conditioning screen installed and $\Delta 1 = \Delta 2$. Contour plots of the velocity measured with the flat-ceiling and contoured-ceiling test sections are shown in Table A.6. The dips in velocity along the middle of the top and bottom walls are due to uneven tensioning of the flow-conditioning screen.

Table A.6 Velocity Spatial Distribution for $\Delta 1 = \Delta 2$ with Flow-Conditioning Screen



The spatial uniformity of the flow entering the test section was measured with the flow-conditioning screen and flat-ceiling test section installed. Contour plots of the velocity measured with $\Delta 1 - \Delta 2 = 0.1$ m and $\Delta 1 - \Delta 2 = 0.2$ m are shown in Table A.8, with $(\Delta 1 + \Delta 2)/2 = 0.3$ m for both cases. The dips in velocity along the middle of the top and bottom walls are due to uneven tensioning of the flow-conditioning screen.

Table A.7 Velocity Spatial Distribution for $\Delta 1 \neq \Delta 2$ with Flow-Conditioning Screen

	Flat-Ceiling Test Section $\Delta 1 - \Delta 2 = 0.1$ m $U(\text{side 1}) / U(\text{side 2}) = 1.007$	Flat-Ceiling Test Section $\Delta 1 - \Delta 2 = 0.2$ m $U(\text{side 1}) / U(\text{side 2}) = 1.016$
Slow		
Med		
Fast		

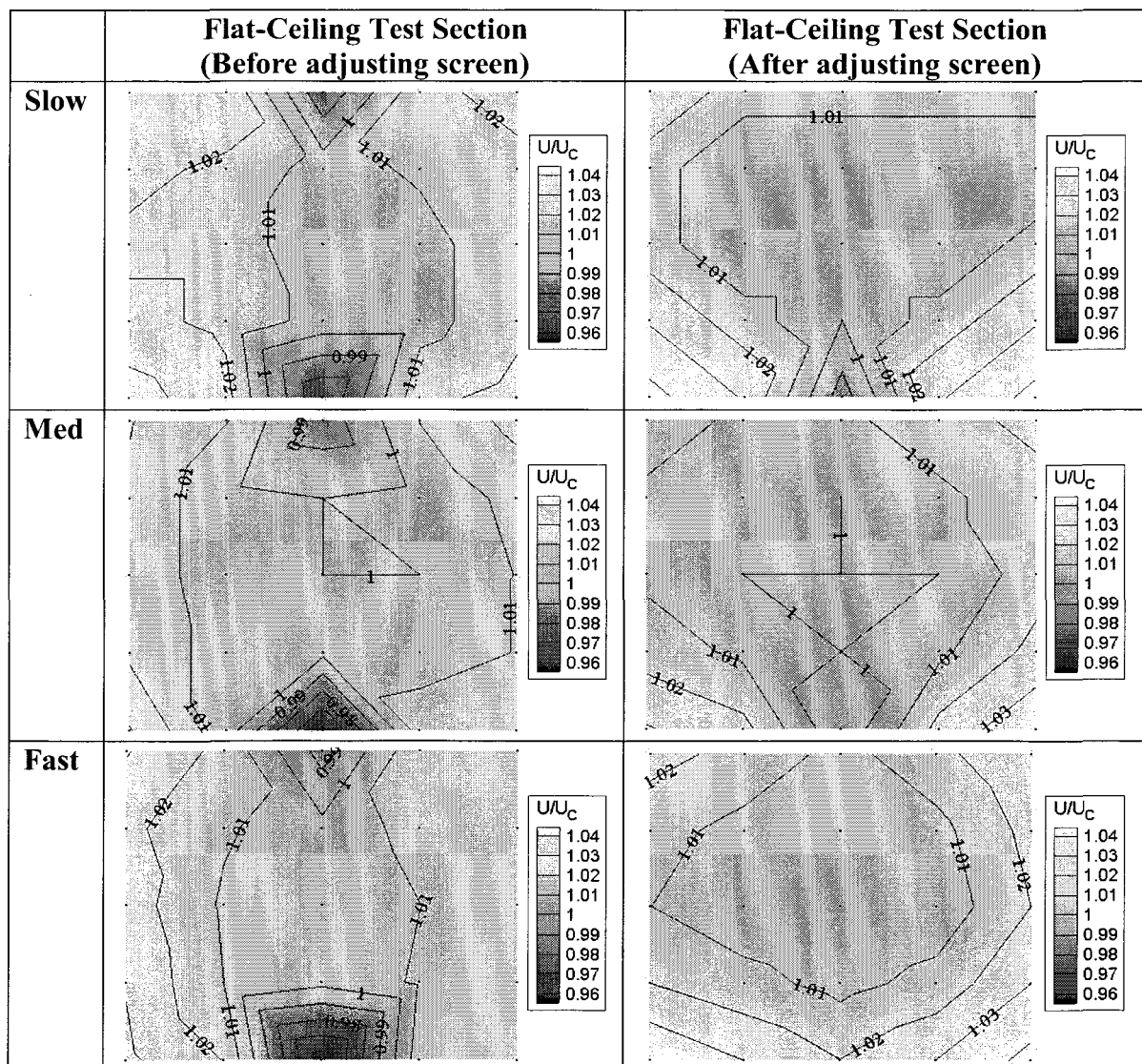
The repeatability of the spatial uniformity of the flow entering the test section was measured with the flow-conditioning screen and flat-ceiling test section installed, with $\Delta 1 = \Delta 2$ and $((\Delta 1 + \Delta 2)/2) = 0.3$ m. Contour plots of the velocity are shown in Table A.9. The results indicate good repeatability over time, with the average velocities changing by less than 0.5%. The dips in velocity along the middle of the top and bottom walls are due to uneven tensioning of the flow-conditioning screen.

Table A. 8 Velocity Spatial Distribution Repeatability

	Flat-Ceiling Test Section (First Day of Tests)	Flat-Ceiling Test Section (Last Day of Tests)
Slow		
Med		
Fast		

After determining that the dips in velocity along the middle of the top and bottom walls were due to uneven tensioning of the flow-conditioning screen, the screen was removed, re-tensioned and re-installed. Contour plots of the velocity measured before and after the screen adjustment are shown in table A.10. The results show improved uniformity, with more uniform overall appearance after the flow-conditioning screen tension was adjusted.

Table A.9 Effect of Flow-Conditioning Screen on Velocity Spatial Distribution



Appendix K. HOTWIRE ANEMOMETER DATA REDUCTION

A substantial amount of post-processing was completed on the hotwire anemometer signal recorded by the oscilloscope to obtain the turbulence intensity of the flow entering the test section. The first step of the post-processing was to convert the hotwire anemometer signal from the time domain into the frequency domain using fast Fourier transforms. In the frequency domain, a low-pass filter was applied to the signal with a cut-off frequency of 5 kHz. The selection of this cut-off frequency was based in part on the experimental data published by Nishi et al. (1997) and Garg et al (1997). The second step of the post-processing was to remove the electronic noise from the hotwire anemometer signal. It was observed that the electronic noise with the feedback loop of the Wheatstone bridge opened is similar in magnitude to the electronic noise with the feedback loop of the Wheatstone bridge closed. Therefore, the hotwire anemometer signal with the feedback loop opened was recorded to provide an estimate of the electronic noise. The signal representing the electronic noise was converted to the frequency domain using fast Fourier transforms and subtracted from the signal with the feedback loop closed, resulting in a signal containing the voltage fluctuations created by the flow turbulence only. This process is believed to provide a conservative estimate of the fluctuations in the hotwire anemometer signal, as it is expected that the amplitude of the electronic noise increases when the feedback loop of the Wheatstone bridge is closed. The signal with the low-pass filter applied and electronic noise removed was then transformed from the frequency domain back into the time domain using inverse fast Fourier transforms.

The next step in the reduction of the hotwire anemometer signal was to convert the measured voltage fluctuations into the corresponding velocity fluctuations. By recording the velocity in the test section simultaneously with the hotwire anemometer signal, it was possible to relate the change in voltage to the change in velocity over the range of wind tunnel speeds tested. This relationship is shown in Equation A.1, where V is the mean voltage from the hotwire anemometer at a given wind tunnel speed and $\partial U/\partial V$ is the rate of change of velocity with respect to voltage.

$$\frac{\partial U \left[\frac{m}{s} \right]}{\partial V [V]} = -3.6416V^3 + 77.934V^2 - 547.22V + 1269.9 \quad (\text{A.1})$$

The turbulence intensity of the flow was calculated using Equation A.2., where V_{RMS} is the RMS of the fluctuating components of voltage about their mean value and $\partial U/\partial V$ is calculated using the mean voltage of the data set.

$$T.I. (\%) = \frac{\left[\frac{\partial U}{\partial V} \right] V_{RMS}}{U} 100\% \quad (\text{A.2})$$

Based on the selected oscilloscope measurement range of ± 8 mV, the error associated with each voltage measurement is $\pm(0.08 \text{ mV} + 1.5\% \text{ of the measurement})$. This corresponds to an error in turbulence intensity of $\pm 0.04\%$ at a wind tunnel velocity of 1 m/s and $\pm 0.01\%$ at a wind tunnel velocity of 10 m/s

Appendix L.

STAGNATION PRESSURE DROP IN AXIAL-TURBINE

The stagnation pressure drop across the axial-turbine rotor was estimated using the data for propeller turbines shown in Figure A.12, assuming a specific speed (Ω) of 3.

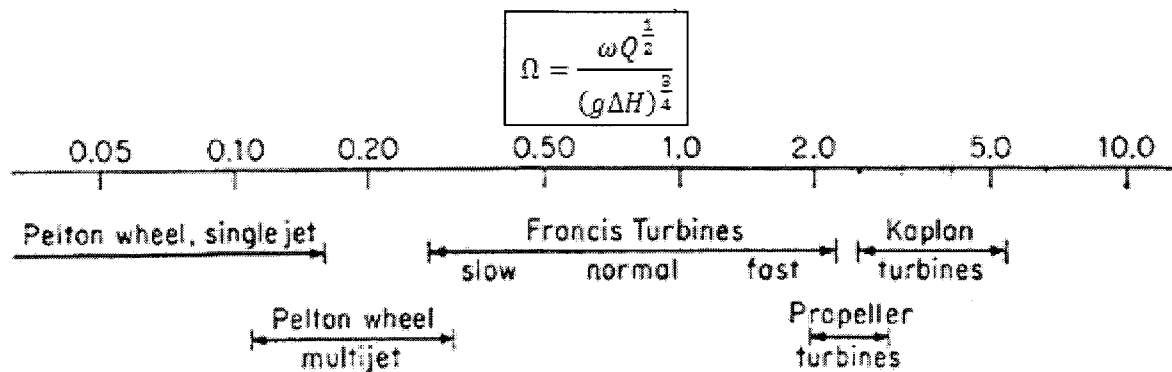


Figure A.12 Specific Speeds for Various Hydraulic Turbines

(Modified from (Sjolander, 2008))

The rotational speed of the turbine was assumed to be 2.6 rad/s based on current turbine designs and the desire for a slow rotational speed to minimize fish-kill. The volume flow rate was calculated assuming a free-stream velocity of 1.75 m/s and a blade diameter of 1 m. These values are based on the design currents for other hydraulic turbines and typical water conditions for locations where hydrokinetic turbines may be installed, such as the St. Lawrence Seaway where the current varies from 1.5 to 2 m/s and the depth is around 12 m on average (Canadian Hydrographic Services, 2009). The pressure drop across the turbine rotor was calculated using Equation A.3.

$$\Delta P_{turbine} = \rho g \Delta H = \rho \left(\frac{\omega Q^{\frac{1}{2}}}{\Omega} \right)^{\frac{4}{3}} = 1021.46 Pa \quad (\text{A.3})$$

The stagnation pressures applied at the axial intake of the exhaust duct computational domain are calculated in Equation A.4 and Equation A.5.

$$P_{total (bypass flow)} = P_{freestream} = P_{static} + 1531.25 Pa \quad (\text{A.4})$$

$$P_{total (turbine flow)} = P_{freestream} - \Delta P_{turbine} = P_{static} + 509.79 Pa \quad (\text{A.5})$$

Appendix M. DESCRIPTION OF WATER CHANNEL FACILITY

The Department of Mechanical and Aerospace Engineering's water channel is a Model 2436 designed by Rolling Hills Research Corporation (RHRC) and was installed in 2268 ME in March 2008. A schematic of the water channel with the major components labelled is shown in Figure A.13. The Model 2436 is a closed-circuit, continuous flow water channel with a horizontal test section that is 0.61 m (24 in.) wide, 0.91 m (36 in.) deep and 1.83 m (72 in.) long. The water channel holds up to 19,000 L and has a 12.2 m by 6.1 m footprint.

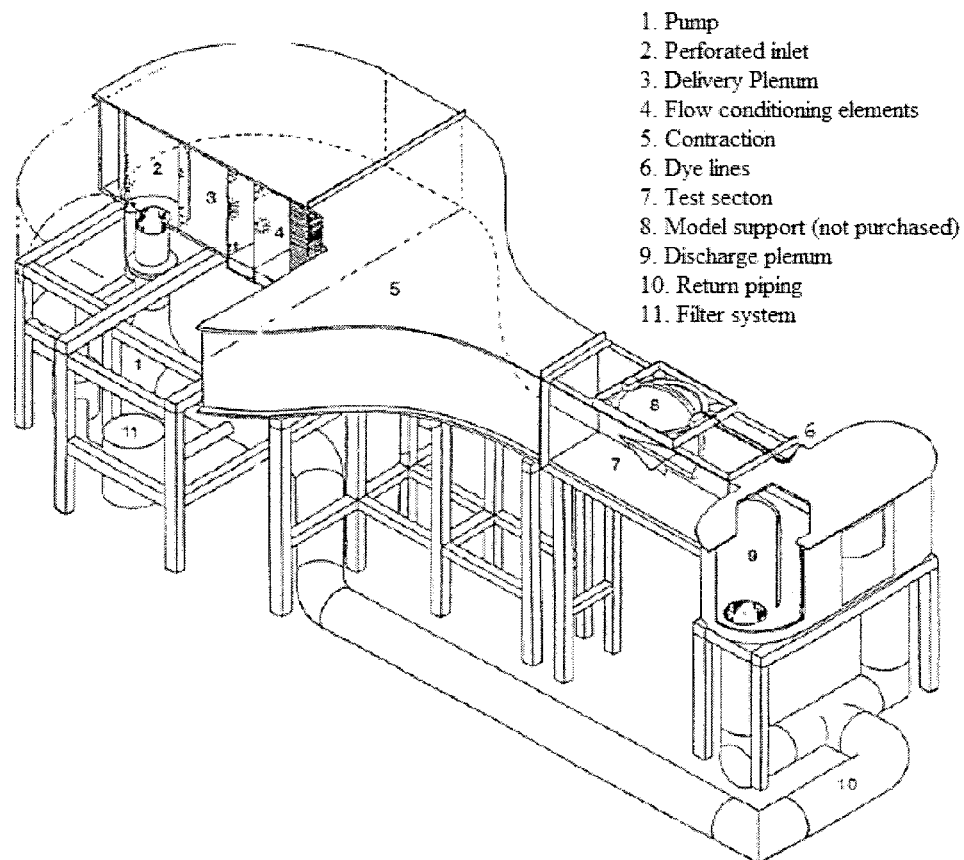


Figure A.13 Schematic of Water Channel Facility

(RHRC, 2003)

A 5.59 kW (7.5 Hp) pump installed with the water channel drives the flow through the water channel circuit. The pump is capable of moving 176.7 L/s (2800 gpm) of water to supply a test section velocity of up to 0.3048 m/s (1 ft/s). (RHRC, 2003)

Water enters the delivery plenum at the upstream end of the water channel through a perforated inlet cylinder. The cylinder is perforated to absorb energy across its length and ensure uniform flow delivery. (RHRC, 2003)

Flow-conditioning elements, located upstream of the contraction, were designed to ensure uniform, low-turbulence flow entering the test section. The flow conditioners consist of a perforated stainless steel plate and two fibreglass screens to reduce the size of the turbulence structures and a honeycomb to straighten the flow. These elements can be rearranged or removed as desired, but it is important to remove trapped air bubbles after submerging the flow conditioning devices before running any experiments or the flow quality could be compromised. The contraction accelerates the flow into the test section and has a contraction area ratio of 6. The contraction was designed to avoid boundary layer separation and ensure uniform, steady and low-turbulence flow into the test section. (RHRC, 2003)

The walls of the test section diverge to compensate for boundary layer growth in order to maintain a uniform velocity profile over the length of the test section. The velocity in the test section can be varied from 0 to 0.3048 m/s (12 in/s), using a controller with a resolution of 2.54 mm/s (0.1 inch/s). The test section was designed to have

turbulence intensity levels less than 1.0%, velocity non-uniformity less than $\pm 2\%$, and mean flow angularity less than ± 1.0 deg. in both pitch and yaw (RHRC, 2003). The sides and bottom of the test section are made of clear, tempered glass to allow for flow visualization and laser measurements. A platform on one side of the water channel shown in Figure A.14 was recycled from a previous facility to facilitate access to the test section.

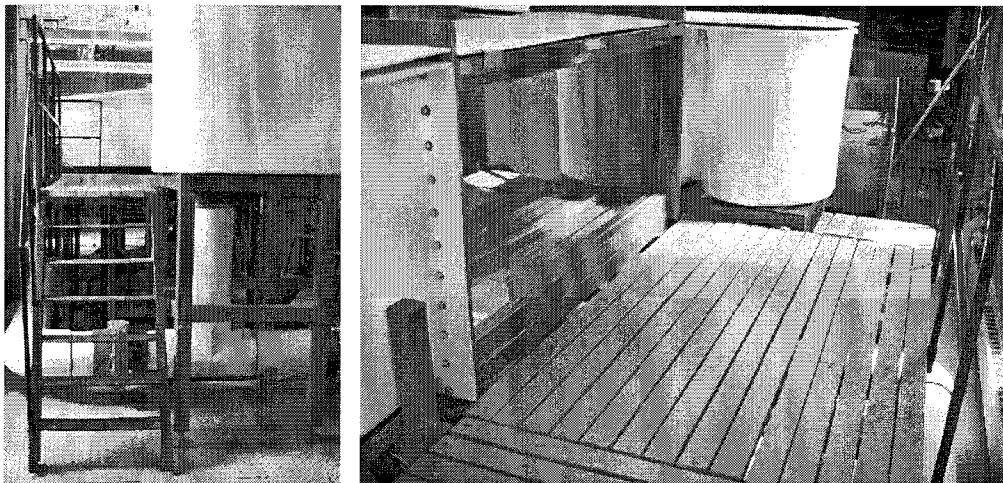


Figure A.14 Photographs of Water Channel Platform

The discharge plenum is located downstream of the contraction and includes a window to view the test section from the downstream direction. It includes two perforated cylinders, similar to those at the inlet of the delivery plenum. The two cylinders and the shape of the downstream end of the water channel were designed to ensure no flow angularity or turbulence develops which could propagate upstream. Without the installation of the perforated cylinders, large vortices form where the water drains into the return piping, similar to water swirling down a sink drain. The cylinders

eliminate this vortex and ensure that air and other foreign objects are not sucked into the return piping. (RHRC, 2003)

A velocity sensor installed in the return piping was calibrated to provide the velocity of the flow in the test section and display it on a digital readout. Also installed with the return piping is a filtration system used to clear the water of contamination from dirt, bacteria and flow visualization dye. The filtration system is similar to those used for residential swimming pools, and consists of a small motor, a strainer and a filter unit. (RHRC, 2003)

Appendix N. FLOW VISUALIZATION IN WATER CHANNEL

The main difficulties associated with photographing flow in the water channel include eliminating reflections from the overhead fluorescent lights on the test section glass and creating a clean, non-reflective background.

The overhead lights in 2268 ME are divided into three different circuits, so the lights directly over the water channel were turned off. This eliminated the majority of the reflections, and the remaining light in the lab was sufficient to provide clear photographs. The light from the windows was reduced by closing the blinds, and the remaining reflections were avoided by careful positioning of the model and the camera. A number of different backdrops, including white fabric and large whiteboards, were tested to determine which backdrop provides the clearest flow visualization photographs. It was determined that white particle board taped to the far side of the test section works best. The particle board has a matte surface which reduces the reflections and provides a clean background for flow visualization photographs.

The 6-colour pressurized dye system attached to the water channel uses water-soluble liquid food coloring for flow visualization. The system is pressurized using the building's high-pressure air lines, and a regulator adjusts the pressure of each dye canister individually. A dye-to-water ratio of 1:4 was found to provide sufficient visual contrast and the addition of chlorine combined with the use of the built-in filter was used to clear the water after using the dye for short periods of time.

Preliminary flow visualization exercises were completed to become familiar with the dye system and experiment with different methods for injecting the dye into the flow. A range of test section velocities and dye pressures were used to visualize flow over a cylinder (see Figure A.15) and the following observations were made.

- i) A large amount of dye was trapped behind the cylinder, indicating where the flow was re-circulating.
- ii) It is important to match the dye injection to the test section velocity; if it's too slow or too fast the dye does not come out in a straight, uniform streamline.
- iii) At faster test section velocities, a fast shutter speed is necessary to prevent the images from blurring.

The clearest photographs were obtained at low velocities, since the dye does not disperse as quickly and the camera shutter speed is capable of taking the images without blurring. It was found that flow velocities less than 0.1 m/s (4 in/s) provided the best photographs.

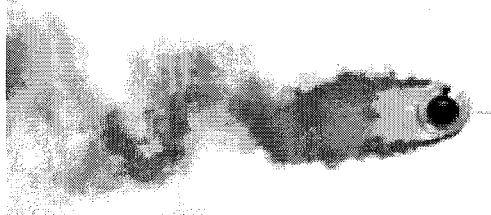
Test Section Velocity	Photograph	Comments
0.1 m/s (4 in/s)		<p>Insufficient dye pressure</p> <p>Vortices are not distinctly outlined</p>
		<p>Good dye pressure</p> <p>Vortices are clearly defined</p>
		<p>Too much dye pressure</p> <p>Vortices are blurring together</p>
0.25 m/s (10 in/s)		<p>Flow velocity is too fast to get a clear photograph</p> <p>Dye diffuses very quickly</p>

Figure A.15 Visualization of Flow over a Cylinder